2008

STREAM-COORDINATE STRUCTURE AND VARIABILITY OF THE KUROSHIO EXTENSION

Penelope Jane Howe
University of Rhode Island

Library Rights Statement

In presenting the thesis, Stream-Coordinate Structure and Variability of the Kuroshio Extension, in partial fulfillment of the requirements for an advanced degree at the University of Rhode Island, I agree that the Library shall make it freely available for inspection. I further agree that permission for copying, as provided for by the Copyright Law of the United States (Title 17, U.S. Code), of this thesis for scholarly purposes may be granted by the Librarian. It is understood that any copying or publication of this thesis for financial gain shall not be allowed without my written permission.

I hereby grant permission to the University of Rhode Island Library to use my thesis for scholarly purposes.

_____

Penelope Jane Howe

_____

Date

STREAM-COORDINATE STRUCTURE AND VARIABILITY OF THE KUROSHIO EXTENSION

BY

PENELOPE JANE HOWE

A THESIS SUBMITTED IN PARTIAL FULFILLMENT OF THE

REQUIREMENTS FOR THE DEGREE OF

MASTER OF SCIENCE

IN

OCEANOGRAPHY

UNIVERSITY OF RHODE ISLAND

2008

MASTER OF SCIENCE THESIS

OF

PENELOPE JANE HOWE

APPROVED:

Masters Committee:

Major Professor _____

_____

_____

_____

DEAN OF THE GRADUATE SCHOOL

UNIVERSITY OF RHODE ISLAND

2008

ABSTRACT

Fine horizontal-scale surveys performed during the Kuroshio Extension System Study deployment cruise in May 2004 provide near-synoptic ADCP and CTD data along cross-jet transects just up-stream of the first meander trough of the Kuroshio Extension. An array of Current and Pressure-recording Inverted Echo Sounders (CPIES) deployed during this cruise over a $\sim$600x600 km region centered on the first meander trough also provide time series of bottom pressure and currents as well as acoustic travel time measurements (τ), which are converted via the Gravest Empirical Mode method to profiles of temperature, salinity, and specific volume anomaly. This combination allows calculation of absolute (barotropic plus baroclinic) geostrophic velocity profiles, and all data are mapped via optimal interpolation to a higher resolution grid covering the entire array area. The datasets from the surveys and the CPIES are used here to analyze the mean and time-varying velocity, hydrographic, and potential vorticity structure of the Kuroshio Extension in its "weakly meandering" state in a stream-coordinate system, which avoids the lateral smearing of the jet structure that would result from an Eulerian approach.

Stream-coordinate analysis reveals a canonical baroclinic jet structure, with isotachs sloping downwards from the cyclonic side of the jet across the core to a subsurface maximum on the anticyclonic side and cross-stream gradients of down-stream velocity that are stronger on the cyclonic side. Maximum surface down-stream velocities range from 1-2 m/s, averaging around 1.4 m/s. Down-stream velocities extend to the bottom just south of the core with average magnitudes of 1-5 cm/s, but vary in magnitude and direction depending upon the presence of deep barotropic eddies. Cross-stream velocities vary in the mean with respect to location along the meander pattern. In the first meander crest, the mean cross-stream flux is towards the cyclonic side, while entering the trough it is towards the anticyclonic side. However, these cross-stream flows appear to be event-driven, with fluctuations in steepness of the meander pattern due to the passage of frontal waves a probable driving mechanism. Relative vorticity (ζ) is found in the mean from

the surveys to make contributions as high as 72% of f on the cyclonic side and -41% of f on the anticyclonic side, while the "twisting" term due to vertical shear and horizontal density gradients reaches a maximum in the mean of 45% of f just north of the core. The lower horizontal resolution of the CPIES dataset produces values of ζ and the twisting term that are about 50 and 75% weaker than in the surveys, respectively. However, comparison of the structure at various phases of the meander pattern reveals differences in the distribution of relative vorticity across the core. Both datasets suggest the presence of four isopycnal potential vorticity gradient layers, where strong cross-stream gradients represent a "barrier" to cross-stream flow. These layers include, in order of decreasing cross-jet gradients, the mode water, the main thermocline, the lower thermocline/North Pacific Intermediate Water core, and a relatively homogeneous deep layer. Comparison of the Kuroshio Extension to the Gulf Stream suggests that although the two possess many qualitative structural similarities, mean velocities and gradients are generally about 30% weaker in the Kuroshio Extension, and the strong jet structure penetrates to about 25% greater depths in the Gulf Stream.

ACKNOWLEDGEMENTS

First and foremost I would like to express my gratitude to my advisor, Kathy Donohue, for her tireless help and guidance throughout the evolution of this work. Karen Tracey also deserves many thanks for her hard work processing and re-processing datasets, producing last-minute figures and MATLAB code, providing a backup computer in times of distress, and of course for editing and updating the LaTeX templates that make this document so beautiful. Thanks are also due to Randy Watts for his helpful input as a member of my committee and to Bud Vincent and Leonard Kahn and the entire committee for granting me safe passage through the defense. I am also in debt to fellow students Christian Buckingham, for his intellectual and moral support throughout the process, and Andy Greene, for his enthusiasm to share his fountain of knowledge. Thanks are also in order to Jules Hummon, the Scripps Institution of Oceanography's Ocean Data Facility, and the KESS deployment cruise participants, as well as to the captain and crew of *R/V Thomas G. Thompson* and the National Science Foundation for making this research possible.

PREFACE

Rather than using the traditional division of the thesis into chapters, this thesis is written in "manuscript" style. The main text is written in a manner appropriate for submission to a scientific journal and is followed by three appendices which provide additional details about instrumentation, data processing, and the analysis techniques employed in the manuscript.

TABLE OF CONTENTS

LIST OF TABLES

LIST OF FIGURES

MANUSCRIPT 1

The Stable Meander Regime

1.1 Introduction

The Kuroshio Current is the major western boundary current of the Pacific basin. It breaks away from the coast of Japan around 35°N, where it becomes the eastward-flowing zonal jet known as the Kuroshio Extension (KE). Observations have shown that the KE fluctuates between two patterns of flow; the weakly meandering state is characterized by a series of quasi-stationary meanders and a strong, zonally-elongated recirculation gyre, while the strongly meandering state comprises an increase in eddy activity and ring formation and a weakened recirculation gyre [*Mizuno and White*, 1983; *Qiu and Chen*, 2005]. This oscillation between dynamic states has been seen both in observations [*Qiu and Chen*, 2005] and numerical studies [*Taguchi et al.*, 2005] to coincide with changes in wind-stress curl in the central North Pacific, which induce baroclinic Rossby waves that impact the Kuroshio Extension either by causing a shift in up-stream position or by altering the jet structure.

The KE acts as a boundary between the warm, salty waters of the North Pacific Subtropical Gyre to its south and the cold, fresh subpolar waters of the Oyashio Front to its north. Water crosses this frontal zone within the surface wind-forced Ekman layer, in meander crests and troughs, and within warm- or cold-core rings [*Talley et al.*, 1995; *Yasuda et al.*, 1996; *Joyce et al.*, 2001], and such cross-frontal exchange and mixing are important in the formation of North Pacific Intermediate Water (NPIW). *Talley and Yun* [2000] have investigated the mixing processes across the KE that lead to the formation of NPIW, and *Joyce et al.* [2001] found that cross-frontal flux varies as a function of location in the meander crest versus the meander trough. A set of two papers by *Kouketsu, Yasuda, and Hiroe* [2005; 2007], used data from a towed conductivity-temperature-depth (CTD) system to describe the structure of frontal waves propagating along the KE and

the intrusion of a salinity minimum southward across the current in the trough of the frontal wave. Studies within the Gulf Stream system indicate that cross-frontal potential vorticity (PV) gradients influence the possibility of cross-frontal exchange: strong surface PV fronts inhibit exchange ('barrier'); weaker PV fronts at intermediate levels allow partial exchange ('stirring'); and the lack of a PV gradient at deeper levels results in well-mixed water properties ('blender') [*Bower et al.*, 1985]. The meander structure itself has also been shown in the Gulf Stream to impact cross-frontal motion of water parcels within the jet, with troughs (crests) inducing equatorward (poleward) flow [*Bower and Rossby*, 1989; *Bower*, 1991].

Despite the above-mentioned advances in understanding exchange and mixing processes in the KE region, in contrast to the Gulf Stream system, little progress has thus far been made in characterizing the mean synoptic structure of the KE. The method which has become widely accepted as the preferred alternative to Eulerian, geographical coordinates in describing the synoptic structure of a baroclinic jet is the "stream-coordinates" method, in which coordinate axes point in the instantaneous down- and cross-stream directions and cross-stream location is defined relative to some characteristic of the current. In 1989, *Hall* used a single current meter mooring to determine an average stream-coordinates velocity cross-section of the KE at 32°N, 152°E, using the temperature at 350 dbar to define cross-stream position within the current and velocity shear to define the down-stream direction. A mean transport of the KE was also calculated, but data were not available to generate hydrographic cross-sections to accompany the current meter data. This study aims to partially fill the gap in the KE knowledge base by determining the mean down- and cross-stream velocity, hydrographic, and potential vorticity (PV) structure of the KE in a stream-coordinate system during the weakly meandering state; determining how this structure varies between meander crest and trough; and identifying and characterizing regions of possible cross-frontal exchange evidenced by PV gradients, enhanced cross-stream velocities, and water property transport. A comparison of these structural aspects of the KE and Gulf Stream systems is also presented.

The data for this investigation come from the Kuroshio Extension System Study (KESS), which is a multi-institutional investigation into the dynamics and variability of the KE and its recirculation gyres. Observational instruments deployed in May 2004 included an array of 46 Current- and Pressure-recording Inverted Echo Sounders (CPIES) centered on the first meander crest and trough, which provide a three-dimensional time series of the circulation. During deployment of the CPIES, fine horizontal-scale 'feature surveys,' consisting of continuous Acoustic Doppler Current Profiler (ADCP) data and 15-km spaced CTD casts, were conducted across the KE to obtain near-synoptic snapshots of the current structure. The KE was in its weakly meandering state for the first 5.5 months (1 June - 16 November) of the two-year CPIES mission before transitioning to the strongly meandering state for the remainder of the study, providing a unique opportunity for future studies to compare the characteristics of the two meander states.

In the next section, details of the synoptic survey and CPIES datasets are provided, and the methods and calculations used to create stream-coordinates sections of velocity, hydrography, and PV from both the surveys and the CPIES are discussed. Sections 1.3 and 1.4 describe the KE structure as obtained from the surveys and the CPIES and its associated time-variability. The velocity structure displays many of the typical characteristics of a baroclinic jet, with maximum surface down-stream velocities ranging between 1-2 m/s and a cross-jet structure at shallow depths in the center of the jet that is relatively invariant with location in the meander pattern. Cross-stream velocities occasionally reach magnitudes of 15-20 cm/s and appear to be event-driven, with fluctuations in steepness of the meander pattern due to the passage of frontal waves a probable driving mechanism. The implications of the PV structure for cross-frontal exchange are also discussed, and four distinct PV-gradient layers are identified at the depths of the mode water, the main thermocline, the lower thermocline/NPIW core, and below. In section 1.5, a comparison is made to previous observations of the Gulf Stream, showing that the KE in general has about 30% weaker maximum magnitudes of velocities and gradients and about 25% less depth penetration. Section 1.6 provides a summary of the findings of this study and suggestions for future work in which these findings may prove invaluable.

1.2 Data and Methods

1.2.1 Synoptic Surveys

ADCP/CTD Data A 75 kHz RD Instruments Ocean Surveyor hull-mounted ADCP collected upper-ocean velocity data down to about 700 meters throughout the KESS deployment cruise aboard *R/V Thomas G. Thompson* from 25 April to 1 June, 2004. Data were collected every second over 16-m depth bins and processed using the CODAS system developed at the University of Hawai'i (see Appendix A for details). Although the shallowest bin was contaminated by acoustic ringing, performance was excellent over the remaining depth range. Data were averaged to five-minute time intervals for storage in the CODAS database and were then further averaged to approximately ten-minute time increments over 20-m depth bins in the datasets used for this study. Feature surveys consisting of CTD casts reaching 1200 to 1500 dbar at horizontal intervals of approximately 15 km were conducted along cross-current tracks of about 200 km length. Their locations are shown superimposed over mean sea-surface height contours from AVISO Rio05 for the time of the deployment cruise in Figure 1.1. Four such crossings were performed in and just up-stream of the first meander trough over a period of about 5 days, moving progressively down-stream from Crossing 1 to Crossing 4. Three additional crossings of the current took place in the trough area without accompanying CTD data, with Crossing 5 occurring one day prior to Crossing 1, Crossing 6 several days after Crossing 4, and Crossing 8 about two weeks later. Crossing 7 was performed at the top of the first meander crest, also without CTD data. Table 1.1 lists the dates, locations relative to the meander pattern, and availability of CTD data for each crossing. These transects provide a near-synoptic representation of the cross-stream structure of the KE during the weakly meandering state, in which the current remained throughout the deployment cruise.

Rotation of ADCP and CTD Data to Stream-Coordinate System

The use of stream-coordinate rotation in this study is consistent with previous similar analyses of baroclinic jets such as the Gulf Stream [*Halkin and Rossby*, 1985; *Rossby and Zhang*, 2001] and

the Subantarctic Front [*Meinen et al.*, 2003], among others. The need for the stream-coordinates approach arises from the meandering of the current system, which causes geographical shifts in the instantaneous location of the high-velocity core of the jet as well as in the instantaneous orientation of down-stream flow. These shifts lead to a temporal average in Eulerian coordinates that does not properly represent the synoptic structure of the current. For example, the meandering current will always appear broader and weaker in an Eulerian average, and cross-stream gradients will be biased low. Figure 1.2 demonstrates the benefits of adopting a stream-coordinate system in the KE. Panel *a* shows the latitudinal average of zonal velocity data from Crossings 1-4, while panel *b* shows the average of these data as a function of distance from an identified core. Improvement in the resolution of the velocity core can be seen to some extent between panels *a* and *b*, but in panel *c*, where the data are rotated into the stream-coordinate system, the jet structure is clearly more robust, displaying 39% greater velocity magnitudes at and surrounding the core as well as increased cross-stream velocity gradients. By comparison, simply rotating the zonal velocity core into the mean down-stream direction of -39° produces only a 29% increase in magnitude at the velocity core $(1/cos(39^\circ) = 1.29)$.

Rotation into stream coordinates is achieved by first identifying the location of the origin, or *core*, and then determining the direction of down-stream flow. Since the feature survey data are already in the form of cross-current transects, they are then simply projected onto the cross-stream line and velocities are rotated into down- and cross-stream components. The methods used for each of these steps are discussed below. The stream-coordinate system in this study is defined with the positive Y-axis as the instantaneous down-stream direction and the X-axis as cross-stream, with positive to the right of Y. For the purposes of the following discussion, "southward" and "equatorward" shall be used interchangeably to mean "in the positive cross-stream direction." Positive values of cross-stream velocity therefore indicate "southward" cross-stream flow.

Determining Core Position Traditionally, hydrographic data have been used to define the core of a jet current. For the Gulf Stream, *Halkin and Rossby* [1985] cite several possible means of determining core position according to the locations at which certain isotherms cross a particu-

lar depth, ultimately choosing to define the core as the halfway point between where the 12°C isotherm crosses 400 and 600 m. *Mizuno and White* [1983] choose to define the mean path of the Kuroshio as the location at which the 12°C isotherm crosses 300 m, which they note typically falls at or close to the center of the temperature front in all seasons throughout the KE. *Hall* [1989] uses temperature at 350 dbar to determine cross-stream position of her current meter mooring within the meandering current, assuming a time-invariant cross-stream temperature structure. However, in an ADCP study of the Gulf Stream by *Rossby and Gottlieb* [1998], the core of the current is defined simply as the location of the maximum velocity vector. Similarly, in an ADCP and Expendable Bathythermograph (XBT) study by *Rossby and Zhang* [2001], the stream-coordinate system is defined with the origin at the location of the velocity maximum of the Gulf Stream at 52 m depth.

After examination and comparison of various hydrographic and velocity-based methods (see Appendix B for details), the final choice for core location definition with the KESS dataset was to use the location of the maximum velocity from the ADCP data after averaging over the 100-300 m depth range and gridding the data to a 5-km horizontal grid. A deeper average was chosen over a shallower average or a single depth in order to reduce the influence of noise in the data or of near-surface wind-induced submesoscale currents or inertial oscillations. The hydrographic data, a sample of which can be seen in Figure 1.3, show some high vertical wavenumber variability in the temperatures on lateral scales reaching up to 15 km, most likely due to the $\sim$15 km spacing between CTD casts, which suggest that the ADCP data may be a more reliable means of locating the core than the hydrography. The vertically-averaged cross-stream velocities (sample shown in Figure 1.4) appear to introduce $<$5 km lateral ambiguity in core position. Furthermore, several crossings of the current were made that did not include fine-scale CTD surveys, so a definition that does not rely on CTD data was preferable in order to incorporate those crossings into the complete data set using consistent methods.

Determining Core Direction Once the core has been identified, the down-stream direction of the current must be defined. With data from a current meter mooring, *Hall* [1989] uses the

direction of the velocity shear between 500 and 1200 dbar to determine down-stream direction in the KE. In the Gulf Stream, *Johns et al.* [1995] use a similar method with data from the SYNOP mooring array, but in some situations near the edge of the current (not applicable here, as the shear method is not used and a single down-stream direction defined near the center of the jet is applied here to the entire transect) they substitute a different method, defining down-stream as tangent to the contour of the 12°C isotherm crossing 400 m. *Rossby and Zhang* [2001] use the direction of the maximum velocity at 52 m depth to define a down-stream direction of the Gulf Stream at their site of study for each crossing, while *Halkin and Rossby* [1985] use an average of the direction of the three central maximum transport vectors for each of their Gulf Stream transects. In the present study, a unique down-stream direction is defined for each crossing of the KE using the horizontal vector-average of the three vectors centered on the core, vertically averaged over 100-300 m. Various other methods were examined (Appendix B), but differences in both rotation angles to obtain the new cross-stream line and rotation of currents with depth from the defined down-stream direction were minimal among the definition methods, with a maximum difference between the best methods of about 1.25° in transect line rotation for any one crossing.

Projecting and Rotating Data onto Stream-Coordinate Axes The ADCP data, originally obtained in the standard east-north coordinate system, are linearly interpolated to an even 10-minute temporal grid and then regridded with nearest neighbor interpolation to 5-km horizontal spacing (approximately 16-minute intervals when traveling at 10 knots) along a straight line between the first and last CTD stations of the survey. If no CTD data are available, the locations of the first and last ADCP vectors for the crossing are used. The actual ship track is close enough to a straight line that the projection of the velocity vectors onto that line is not considered a significant source of error; maximum on-station drift during a CTD cast is about 10 km and is primarily in the down-stream direction. In the vertical, the data are averaged into 20-m bins, with a weighted average value given at the center of each bin. The cross-stream (U) and down-stream (V) velocity component values are then calculated along the new rotated cross-stream

line according to

$$U = u\ sin(\phi) - v\ cos(\phi) \tag{1.1a}$$

$$V = u\ cos(\phi) + v\ sin(\phi), \tag{1.1b}$$

where (u, v) are the east-north velocity components from the ADCP and ϕ is the defined down-stream direction (with 0 pointing due east). This amounts to a clockwise rotation of the east-north coordinate system by $\frac{\pi}{2} - \phi$, where ϕ is negative heading into a trough and positive approaching a crest. Figures 1.4 and 1.5 provide a graphical demonstration of this process. After projection along the down-stream axis onto the cross-stream line and rotation into stream-coordinate components, the velocity data are once again interpolated to 5-km horizontal grid-spacing using linear interpolation.

Errors in the orientation of the down-stream axis induce maximum errors in cross-stream velocity magnitudes where the overall current speed is a maximum. Taking the maximum absolute velocity of the current to be about 2 m/s, the resulting maximum error due to a 1.25° down-stream offset is about 4.5 cm/s in the cross-stream direction, dominating the possible error due to the instrument (<1 cm/s, see Appendix A). On the other hand, the errors in down-stream velocity magnitude due to a 1.25° down-stream direction error are negligibly small (O(2 mm/s)) compared to the possible instrument error. Propagating instrument error and down-stream angle error through Equations 1.1a and b suggests maximum errors of 1-2 cm/s in down-stream velocities and 4-5 cm/s in cross-stream velocities for individual measurements at the high-speed velocity core. The magnitude of these errors, particularly in the cross-stream component, decreases with the magnitude of the total velocity. For example, for absolute velocity magnitudes around 0.6 m/s, down-stream velocity magnitude errors remain about 1 cm/s due to instrument error, but cross-stream velocity error magnitudes are reduced to about 1.5-2 cm/s.

In order to put the CTD data into the same stream-coordinate system as the ADCP data, they are first projected along a line perpendicular to the ship track onto a straight line between the first and last stations of the crossing and then along the down-stream direction for that transect (Y-

axis) onto the rotated cross-stream line. Projection onto the new cross-stream line is equivalent to compression of the inter-station distances by a factor of $cos(\theta_r)$, where θ_r is the rotation angle between the original ship-track line and the cross-stream line, with positive (negative) values representing counterclockwise (clockwise) rotation. After this projection, the data are linearly interpolated from their spacing along the cross-stream line (reduced from the original $\sim$15-km spacing by $cos(\theta_r)$) to the same 5-km spacing of the ADCP data.

1.2.2 KESS CPIES Array

Inverted Echo Sounders were deployed at forty-six locations in an array centered on the first quasi-stationary meander trough of the KE east of Japan, as shown in Figure 1.6, with horizontal spacing of about 84 km and diagonal spacing of about 94 km, from June 2004 to June 2006. CPIES were equipped with both Paroscientific bottom pressure sensors and Aanderaa acoustic Doppler current meters (RCM-11s) moored 50 m above the bottom, although some instruments had only the pressure sensor (PIES). Eight tall moorings (blue stars) included upward-looking ADCPs at 250 m, McLane moored profilers between 250-1500 m, and deep current meters at 1500, 2000, 3500, and 5000 m. Solid black lines in the figure are the Generalized Digital Environmental Model mean surface dynamic height contours in dyn-cm referenced to 1000 dbar from *Teague et al.* [1990]. The 2000 and 4000-m isobaths are shaded dark and light gray, respectively. Eddy kinetic energy determined from satellite sea surface height anomaly $>$ 0.18 and 0.24 m^2s^{-2} is color shaded yellow and orange, respectively. Data from the PIES included round-trip bottom-to-surface acoustic travel time (τ), bottom pressure, and bottom temperature, with the CPIES also recording current velocity 50 m above the bottom. After suitable low-pass filtering and tide removal, resulting data time series were subsampled at half-day intervals for use in this study. Early battery failure and shorts in the current meter cables caused some instruments to stop recording prematurely, but nearly full coverage of the array is available for the first sixteen months of deployment. The KE remained in the weakly meandering state for approximately the first 5.5 months of CPIES data collection.

Through a compilation of historical hydrographic data from the region and calibration CTD casts performed during KESS, a look-up table called the Gravest Empirical Mode (GEM) is created to define the empirical relationship between the vertical round-trip acoustic travel time (τ) of a pulse emitted from the CPIES and temperature (T) and salinity (S). A GEM relating τ and specific volume anomaly (δ) can also be defined since δ depends only on T, S, and pressure. These empirical relationships allow τ to serve as a proxy for the hydrographic measurements, and therefore allow the creation of time series of profiles of T, S, and δ at each CPIES site. The GEM technique has been shown to work well in strong baroclinic current regions, where T and S variability across the front may be significant but orderly and may include persistent features that correspond to unique τ values [*Sun and Watts*, 2001]. Values of δ obtained from the GEM can be integrated over the water column, effectively making τ a proxy for geopotential height. Baroclinic shears can therefore be determined via geostrophy, and addition of the CPIES deep pressure and current measurements provides a reference from which to obtain absolute (barotropic + baroclinic) geostrophic velocity profiles. *Donohue et al.* [2008] details the optimal interpolation (OI) methods used to map the velocities over the area of the full array. Appendix C summarizes standard post-processing procedures and the errors associated with the CPIES data.

Since the absolute CPIES velocities are derived via geostrophy and measured bottom currents and pressure, the high wavenumber near-surface effects that produced uncertainty in defining the core of the current with the ADCP data are not a problem here. Therefore, transects across the current in stream coordinates are obtained from the OI-mapped CPIES data by first defining the core as the location of the maximum absolute *surface* velocity along a line of longitude; the down-stream direction is then defined by the direction of this maximum velocity vector. The velocity and T and S maps from the OI products are then linearly interpolated at 12-hour intervals to the new cross-stream line (perpendicular to the down-stream direction), and average down- and cross-stream velocity profiles are calculated over the relevant portion of the time series. Although horizontal resolution is coarser when using the CPIES data instead of the ADCP data from the feature surveys, the longer time series and greater geographical range of the CPIES

puts the synoptic surveys into a broader context that spans the full water-column and defines how the structure changes along-stream and with time.

1.2.3 Stream-Coordinate Vorticity

Since potential vorticity (PV) is theoretically conserved in a fluid parcel in the absence of external torques and neglecting dissipative effects, PV structure can serve as a dynamic tracer. Because PV gradients resist cross-gradient displacement and produce wave motions, regions of a baroclinic jet such as the KE with strong cross-current PV gradients may act as barriers to cross-frontal exchange, while weak PV gradients suggest an increased possibility of exchange, and absence of PV gradient allows free exchange, called the 'blender' effect as per *Bower et al.* [1985]. To calculate total PV across the current for the feature surveys, the gridded CTD data are used in conjunction with the ADCP data, which are extrapolated to the surface by repeating the shallowest measurement. Beginning with Ertel's PV formula,

$$\frac{D}{Dt}\left(\vec{\zeta_a}\cdot\frac{\nabla\rho}{\rho}\right)=0, \tag{1.2}$$

scale analysis and translation into the stream-coordinate system (Y down-stream and X cross-stream, positive to the right) produces the following equation for use with the feature survey transects [*Bower*, 1989; *Rajamony et al.*, 2001; *Logoutov et al.*, 2001]:

$$Q=-\frac{1}{\rho}\frac{\partial\rho}{\partial X}\frac{\partial V}{\partial z}+\frac{1}{\rho}\frac{\partial\rho}{\partial z}\left(f+\frac{\partial V}{\partial X}+\kappa V\right). \tag{1.3}$$

From left to right, these four terms represent the "twisting" vorticity due to cross-frontal density shear and vertical velocity shear, the planetary or "thickness" vorticity, and the relative vorticity expressed in natural coordinates ($\zeta=-\frac{\partial V}{\partial n}+\kappa V$) with $\frac{\partial V}{\partial X}=-\frac{\partial V}{\partial n}$ the cross-stream shear component and κV the component from the curvature of the meander itself. Because the vertical resolution of the CTD data is much higher than that of the ADCP data (2-m bins as compared to 20-m bins), a fourth-order Butterworth filter with a cutoff frequency of 40 m is applied to the CTD data in the vertical before calculating the total PV. The CTD data are then subsampled every 20 m and cropped at the maximum depth of the available ADCP data for the purposes of this calculation. Curvature of the meander is determined by finding the curvature of the sea-surface

height (SSH) contours from AVISO Rio05 during the time of the surveys (which preceded the CPIES array) according to

$$\kappa = \frac{Z_x^2 Z_{yy} + Z_y^2 Z_{xx} - Z_x Z_y (Z_{xy} + Z_{yx})}{(Z_x^2 + Z_y^2)^{3/2}}, \tag{1.4}$$

where Z represents a slightly smoothed SSH surface and subscripts x and y indicate spatial differentiation in the east-west and north-south dimensions respectively [*Watts et al.*, 1995]. Positive values of κ indicate cyclonic curvature.

In contrast to the feature surveys, the CPIES provide a synoptic three-dimensional array of data, so PV calculations from the CPIES dataset can include the contribution to the relative vorticity from the $\frac{\partial U}{\partial Y}$ term in place of the curvature term (κV). Relative vorticity values are obtained in two different ways, the first of which involves finding the cross-stream velocities at sections exactly 10 km up- and down-stream of the location in question and dividing the difference in cross-stream velocities on these two sections at equal cross-stream distances from the core by the down-stream distance between each pair of points (20 km). This results in a value of $\frac{\partial U}{\partial Y}$ that represents the along-stream gradient of the cross-stream velocity and can be compared in magnitude with $\frac{\partial V}{\partial X}$ to determine its relative significance. The second method of calculating relative vorticity obtains values of $\frac{\partial v}{\partial x} - \frac{\partial u}{\partial y}$ over the entire array (where x/u and y/v refer to the standard east-north coordinate system) and then interpolates to the cross-stream line. The two methods serve as a consistency check and produce satisfyingly similar results. The stream-coordinates PV equation used for the CPIES is therefore

$$Q = -\frac{1}{\rho}\frac{\partial \rho}{\partial X}\frac{\partial V}{\partial z} + \frac{1}{\rho}\frac{\partial \rho}{\partial z}\left(f + \left(\frac{\partial V}{\partial X} - \frac{\partial U}{\partial Y}\right)\right), \tag{1.5}$$

where the ζ is expressed in Cartesian rather than natural coordinates. Temperature and salinity profiles are vertically smoothed with a 100-m low-pass 4th-order Butterworth filter, which is large enough to remove noise without compromising the real signal. Values of N^2 ($= \frac{g}{\rho}\frac{d\rho}{dz}$) are calculated every 12 hours from these smoothed fields over the whole array and then interpolated to the cross-stream line.

1.3 Feature Survey Results and Discussion

1.3.1 Velocity and Hydrographic Structure

The down-stream velocity sections for all crossings show similar characteristics to those observed extensively in the Gulf Stream [*Halkin and Rossby*, 1985; *Rossby and Zhang*, 2001; *Johns et al.*, 1995, among others]. As expected in a baroclinic jet, the high-velocity core tilts downwards across the front towards the subtropical gyre center. On average, as can be seen in Figure 1.7, the maximum velocity at 70 m is between 1.8 and 1.9 m/s and occurs about 10 km north of the core, while by 400 m depth the maximum velocity is located about 20 km south of the core. On the anticyclonic side of the jet, little or no vertical shear is present in the top 400 m, with some points even exhibiting a subsurface maximum and slight negative shear towards the surface. This velocity shear structure is a direct result of the thermal wind equations, which state that vertical gradients in velocity are proportional to horizontal gradients in density. A glance at the available hydrographic data reveals that the strongest horizontal density gradients shift in the positive cross-stream direction with depth (Figure 1.8), and the slight negative thermal wind shear south of the core is attributable to a core of warm surface waters advected northwards from lower latitudes (Figure 1.3). Mean velocities at various depths are presented in Figure 1.9, which provides an alternative visualization of the above-mentioned features and errorbars indicating estimates of the standard error of the mean of the four transects. Standard error is calculated as $\sigma/\sqrt{N-1}$, where N has a different value at each location along the transect representing the number of crossings with a measurement at each location. Because there is likely to be some degree of correlation between the individual surveys, this estimate of the standard error is probably biased low. The standard error is undefined in places where data from only one crossing were available. Barotropic tides have not been removed from the survey velocity measurements. However, residuals between hourly and 72-hour low-pass filtered bottom pressure records from the CPIES indicate that tidal currents in the survey region are typically less than 3 cm/s.

Although the same general pattern of the core velocity structure appears in each crossing, ad-

ditional varying velocity features are visible to either side of the jet in the individual transects. Since these features change from crossing to crossing, they are most likely indicative of eddies peeling off or passing by rather than part of the mean jet structure. These features are visible in the CTD data largely as temperature anomalies other than the deepening thermocline. For example, the lateral advection of warmer near-surface waters from lower latitudes is often apparent in the high-speed core of the jet on the anticyclonic side and produces a weak subsurface velocity maximum south of the core (Figures 1.10 and 1.11).

Also visible in the CTD data is the apparent advection of a low-salinity ($<$34 psu) intrusion in the NPIW layer across the current from north to south over the course of the four feature surveys, indicating that southward cross-frontal flux is taking place. In Crossing 1, this low-salinity feature reaches only 40 km south of the core, whereas by Crossing 4 it extends to about 90 km south of the core (Figure 1.12). Examination of the cross-stream velocity profiles from the corresponding crossings (Figure 1.13) reveals southward cross-frontal flow increasing in the deeper anticyclonic portions of Crossings 1-3 which would help advect this low-salinity anomaly across the jet. Although the magnitude of the error associated with the cross-stream velocities at these locations is relatively large (O(0.02 m/s)) compared to the observed cross-stream velocity magnitudes at most locations near the core, by Crossing 3 cross-stream velocities of magnitude 0.04 - $>$0.08 m/s exist between 350 and 550 m depth south of the core, suggesting the existence of a significant southward cross-stream advection.

Although *in situ* SSH or geopotential anomaly data are not available for the time of the surveys, as the CPIES had not yet begun recording, NASA's Tropical Rainfall Measuring Mission (TRMM) satellite's Microwave Imager (TMI) provides accurate 3-day averaged through-cloud SST maps. The passage of frontal waves through the KESS region can be tracked by examining the daily deviation of an SST contour representing the KE front from its mean location over a 6-month time series. Figure 1.24 shows the daily locations of the 17.8°C SST contour and the survey crossings superimposed over the mean SST map and the mean 17.8°C contour. This re-

veals the apparent passage of a frontal wave through the region, causing an enhanced steepness of the meander trough at the time of the feature surveys which may have served as a mechanism for the observed southward cross-frontal transport mentioned above [*Kouketsu et al.*, 2005].

The high-resolution ADCP surveys produce a robust picture of the down-stream component of the velocity structure. However, due to the fact that cross-stream structure appears to evolve with time and along-stream progression (Figure 1.13, the four surveys do not provide a reliable picture of cross-stream fluxes in the trough in the mean. As Figure 1.14 shows, the magnitude of the mean cross-stream velocity is of the same order as the magnitude of the standard error of the mean (calculated in the same manner as for the down-stream velocities) throughout the majority of the mean transect, since the standard error is reflecting along-stream variation. Figure 1.15 presents the mean cross-stream velocities at various depths, with errorbars indicating the standard error of the mean, and shows again that other than near the surface, where slight confluence around the core is apparent, the errorbars do not show the means of the cross-stream flow to be statistically different from zero across the core.

1.3.2 Potential Vorticity Structure

Although the velocity profiles only marginally indicate cross-frontal flow structure, examination of the potential vorticity structure can be helpful in identifying regions where such exchange may be more or less likely to occur. Using Equation 1.3, potential vorticity cross-sections are calculated for each of the four feature survey transects and a mean section is produced by averaging the four as a function of cross-stream distance. Figure 1.16 shows the mean total PV structure, in which a band of relatively high PV can be seen to extend from north to south of the core along deepening isopycnals. Also of note is the large region of low-PV mode water south of the core between isopycnals $\sigma_\theta = 25.1$ and 25.5 kg/m^3. At shallow depths north of the core, the total PV reaches values of the order 10^{-9} m^{-1}s^{-1}, but it remains $O(10^{-10}$ m^{-1}s$^{-1})$ throughout the rest of the region.

Breaking the PV into its four component terms reveals the importance of relative vorticity in generating the observed total PV structure (Figures 1.17, 1.18 and 1.19). Thickness vorticity (Figure 1.20) plays a major role throughout, with a signature that defines the overall structural shape of the total PV. However, in the region just north of the core at shallow depths and extending downwards across the core to about 500 m, both twisting vorticity and the cross-stream shear portion of ζ contribute significant increases to the total PV. The cross-stream shear also adds some negative vorticity at shallow depths south of the core, decreasing the total PV in this location. The maximum of the mean contribution from cross-stream shear is about 72% of f, or about 46% of the total PV, on the cyclonic side of the core, and -41% of f on the anticyclonic side (Figure 1.21). Twisting vorticity reaches a maximum of 45% of f, or about 25% of the total PV, around 100 m depth just north of the core. Curvature adds only a small positive vorticity over most of the profile due to the slight positive curvature of the meander at this location. Negative values of curvature vorticity on the north edge of the profile are due to up-stream-directed velocities and on the south edge to the negative curvature of the recirculation gyre.

Looking at cross-stream PV as a function of σ_θ rather than depth (Figure 1.22) is helpful in assessing PV gradients along isopycnals, which can serve as an indicator of potential cross-stream flow behavior as described in Section 1.2.3. The KESS survey data suggest the presence of four distinct PV-gradient regions correlating with the mode water, the main thermocline, the lower-thermocline/NPIW core, and a deep layer. At the mode water level, between $\sigma_\theta \sim$ 25.1 and 25.5 kg/m^3, a strong gradient exists across the core in the thickness vorticity and is enhanced on both sides of the core by the cross-stream shear and twisting vorticities, which add positive vorticity to the north of the core and negative to the south. Total PV has a negative gradient of $O(10^{-14}$ m^{-2}s^{-1}) from the cyclonic to the anticyclonic side of the core. As suggested by *Bower et al.* [1985], this can be thought of as a "barrier" to cross-frontal exchange, since water parcels tend to conserve PV. In the main thermocline, between $\sigma_\theta \sim$ 25.5 and 26.4 kg/m^3, a weaker gradient in the thickness vorticity is again enhanced on both sides of the core by the combination of cross-stream shear and twisting vorticity, resulting in less intense PV gradients ($O(10^{-15}$ m^{-2}s^{-1}))

across the front which suggest increased possibility of exchange. Between $\sigma_\theta \sim$ 26.4 and 26.8 kg/m^3, at the base of the thermocline, the PV gradient is very weak ($O(10^{-16}$ m^{-2}s^{-1})) and has reversed sign across the core compared to the layers above, with slightly weaker PV values to the north of the core and slightly stronger values to the south. Despite this very slight gradient, this layer likely marks the beginning of the "blender" region, where free exchange is possible as cross-stream PV gradients become negligibly small compared to the planetary effect. Although the survey data do not extend deep enough to fully resolve the lowest layer, it appears that below $\sigma_\theta \sim$ 27.1 kg/m^3, virtually no PV gradient persists and the blender region continues. This will be discussed further with reference to the CPIES data.

While they by no means provide conclusive evidence of the existence of cross-stream flow within different density layers, the following two examples are interesting when considered in conjunction with the structure of the PV gradients. Returning to Figure 1.12, note that the low-salinity anomaly is located below the $\sigma_\theta = 26.4$ contour, placing it within the "blender" region and supporting the theory that cross-stream exchange occurs below rather than above this density level. Figure 1.23 shows the cross-stream velocity transect from feature survey Crossing 5, which occurred at the same location as Crossing 1 and one day prior. Although CTD data are not available for this transect, its proximity in time and space to Crossings 1-4 suggests that their mean density field may represent a reasonable rough estimate of the density field during Crossing 5. Superimposing the $\sigma_\theta = 26.4$ contour from the survey mean potential density onto the Crossing 5 cross-stream velocities reveals that the strong southward flow is occurring only below this density level, again within the "blender" region suggested by the PV gradient structure. Above this density layer, cross-stream velocities are confluent around the core.

1.4 CPIES Results and Discussion

The presence of the frontal wave during the feature surveys described in Section 1.3.1 prompts further investigation of frontal waves in the KESS region via 12-hour maps of geopotential

anomaly at the surface, referenced to 0 at 5300 dbar, generated from the CPIES array. These maps indicate the time-varying shape of the first meander crest and trough. Figure 1.25 shows several snapshots of surface geopotential anomaly over the course of a week in July and reveals the passage of another frontal wave through the region, demonstrating that even during the weakly meandering period a considerable amount of variability exists in the shape and extremity of the meander pattern. This combined with the inconclusive nature of the small sample of cross-stream velocity profiles provided by the feature surveys motivates examination of the longer time series available in the CPIES data. Although the horizontal resolution is considerably less than that of the surveys, with CPIES instruments at approximately 88 km spacings, the broader picture provided by this dataset is invaluable in characterizing the weakly meandering state as a whole. The CPIES provide time series of data over the full water column and across greater lateral distances from the core, as well as allowing for comparison of the structure at different along-stream positions with respect to the meander pattern.

1.4.1 Full Water-Column Velocity Structure

The CPIES array provides the necessary data to calculate stream-coordinates velocity profiles along an extended section of the first meander crest and trough. In the following section, several full water-column transects at various locations along the meander pattern will be discussed in depth, followed by an overview of the surface and bottom features of the full array region. Errors in mean values are presented as standard errors, calculated using a time interval of 19 days between measurements to contribute each additional degree of freedom. This value was determined from autocorrelations of surface and bottom down- and cross-stream velocities across the central part of the jet at a range of phases of the meander pattern using a procedure outlined in *Bendat and Piersol* [2000, p. 173]. Figure 1.26 shows the range of required time intervals across the jet along the mean transect entering the trough. Although the mean required time interval for one additional degree of freedom was considerably shorter than 19 days, this conservative value was chosen to ensure that the significance of bottom cross-stream velocities was not overestimated.

Meander Trough

Although longitude 146°E was representative of the up-stream edge of the meander trough during the time of the feature surveys, the trough location varied significantly over the course of the 5.5-month CPIES time series from the weakly meandering period. Therefore, rather than choose a fixed longitude to represent the trough, which has the undesirable effect of contaminating the perceived trough structure with that from other phases of the meander pattern, the up-stream edge of the trough (about halfway between the inflection point between crest and trough and the trough minimum) was visually tracked through the entire time series via geopotential anomaly maps produced from the CPIES array, and its longitude was recorded at each point in the time series. The mean stream-coordinate structure entering the trough was then determined from the time series of stream-coordinates transects at the specified longitudes. The mean longitude of the up-stream edge of the trough was found to be about 146.4°E using this method.

Figure 1.27 shows mean down- and cross-stream velocity magnitudes entering the trough, approximately co-located with the feature surveys relative to the meander pattern. Figure 1.28 shows a close-up of the core down-stream velocities. The familiar baroclinic jet structure is evident in the down-stream velocities in the top 1500m, with the width of the jet at the surface between the 0.1 m/s contours matching almost exactly that seen in the surveys ($\sim$190-200 km). Cross-stream gradients of down-stream velocity $\left(\frac{\partial V}{\partial X}\right)$, however, are weaker due to the more evenly dispersed isotachs across the core resulting from the reduced horizontal sampling resolution in the CPIES data. The magnitude of the core velocity is about 20% lower in the CPIES mean than in the surveys, at a maximum of 1.4-1.5 m/s as compared with 1.8-1.9 m/s. Figure 1.29 shows the standard error of the mean for the down-stream velocities entering the trough, indicating that the mean core and surrounding jet structure are relatively steady and robust, while the mean approaching the northern end of the 'transect' is not known within significant bounds. The time series of surface down-stream velocities at the core ($X = 0$) (Figure 1.30) shows variation between about 1-2 m/s, suggesting that the KE was in a stronger-than-average flow state during the time of the surveys. The region shaded in gray in the figure reflects the errors asso-

ciated with east-north u, v estimations from the CPIES array as well as the resultant uncertainty in the down-stream direction, all of which are propagated through the down-stream velocity rotation calculation.

Cross-stream velocities are zero by definition at the core at the surface. The mean field shown in Figure 1.27 (lower panel), in which the white zero contour extends down to about 550 m just north of the core, suggests that in the mean, no cross-frontal flux takes place in the upper 550 m, as expected given the existence of the strong PV gradients observed in the surveys. A slight northward flow is seen near the surface north of the core, although error estimates (Figure 1.29) suggest that this may not be significant. Beneath the PV barrier region, however, southward cross-stream flow dominates all the way down to the bottom. Although the magnitude of this cross-stream component lies between 0.5 and 3.5 cm/s given the magnitude of the possible error, it does appear to be a significantly southward rather than northward flow. This agrees with previous studies which found a tendency for southward cross-frontal flow entering meander troughs in the Gulf Stream [*Bower and Rossby*, 1989] and in the KE [*Kouketsu et al.*, 2005].

Also apparent in the CPIES data entering the meander trough is a mean barotropic down-stream component of magnitude 5 cm/s extending all the way to the bottom, where it persists across a 50-km wide region just south of the core. Down-stream directed flow at the bottom spans a total width of $\sim$ 200 km, but the weaker down-stream flows to either side of the 5 cm/s contours likely represent regions where down-stream flow is augmented by the recirculation gyres, whose signatures can be seen in the down-stream velocity profiles as relatively weak (O(10 cm/s)) up-stream directed flows to either side of the jet. The southern recirculation gyre shows stronger near-surface velocities than the northern, reaching a maximum of 0.2-0.3 $\pm$ 0.04 m/s up-stream velocity between the surface and $\sim$500 m depth.

The blue lines in Figure 1.30 show the time series of down- and cross-stream bottom velocities at the core ($X = 0$), again with the gray areas indicating errors associated with east-north u, v esti-

mation from CPIES as well as resultant down- and cross-stream directional errors. Down-stream velocities vary between about -2 cm/s and 15 cm/s, with occasional periods of up-stream rather than down-stream directed flow. These reversals may be attributed to both deep eddy activity and the fact that the maximum down-stream velocity shifts southward with depth and is located slightly south of the surface core in the mean at the bottom.

Cross-stream velocities also exhibit considerable variability, with southward flow dominating in the mean but northward flow present at times, particularly in the first half of the time series. This fluctuation between southward and northward flow appears to correlate with changes in the shape of the meander trough, which at some times is very steep and at others almost flat, due to the passage of frontal waves through the region. In general, since the KE is primarily a zonal jet, the steeper the trough, the greater the deviation of the flow from due east. Thus, the ratio of eastward to total flow at the surface can serve as a scalar proxy measurement for the steepness or angle of the meander. Using this proxy to investigate the relationship between bottom cross-stream velocities at the core and the angle of down-stream flow reveals a linear correlation coefficient of $r = -0.68$. Although this is not an extremely high correlation, a hypothesis test as outlined in Chapter 4 of *Bendat and Piersol* [2000] shows it to be significant, with 95% confidence bounds of $-0.85 < r < -0.37$. The negative sign arises from the fact that a decreasing ratio of eastward to total surface flow implies a steepening of the trough, while southward cross-stream velocities have positive values in our coordinate system. An anticorrelation between the two therefore suggests that southward velocities increase with steepening of the trough, again in agreement with the aforementioned studies of the Gulf Stream and KE [*Bower and Rossby*, 1989; *Kouketsu et al.*, 2005].

Figure 1.31 shows the mean down- and cross-stream bottom velocities entering the trough, as derived from the mapped bottom current meter data, and the associated uncertainty of the mean expressed as a standard error. These error estimates demonstrate the significance of the off-centered mean down-stream flow at the bottom as well as the southward cross-stream flow

spanning most of the central jet region.

While noting the correlation of the direction of cross-stream flow with the extremity of the meander pattern entering the trough, it is also interesting to note the apparent trend shift around day 238 in the time series of cross-stream bottom velocities. During the first part of the record, cross-stream flow seems to be predominantly northward, but after this date, southward flow dominates. Day 238 also marks the time when a warm-core eddy approaching from the northeast begins to be absorbed into the jet at the down-stream edge of the first meander crest. This eddy interacts with the jet for about a month before being released back towards the northeast. Though it by no means indicates causation, the coincidence of these events is intriguing.

Meander Crest

The three-dimensional nature of the velocity and density fields from the CPIES array allows us to compare the structure described above, which is representative of the region of the jet at the up-stream edge of the first meander trough, with that at the western edge of the array in the middle of the first meander crest. Since the crest feature remains relatively fixed in longitude space for the duration of the time series, longitude 143.75°E is chosen to represent the approximate mean peak of the meander crest. Averaging stream-coordinate transects over the 5.5-month weakly meandering period produces the profiles shown in Figure 1.32, with standard errors shown in Figure 1.33. A similar down-stream baroclinic jet structure is seen at the surface near the core, but the width between 0.1 m/s contours is greater here, spanning more than 250 km. *Liu and Rossby* [1993] saw some evidence of narrowing of the jet in a trough region of the Gulf Stream as compared to a crest, which they suggest may be due to an increase in the pressure gradient required to balance both the Coriolis term and the centrifugal term introduced by the meander. The mean velocity magnitude at the core in the crest is also lower than that seen in the trough, but this discrepancy is primarily due to the fact that our calculations of geostrophic velocities do not account for the curvature of the meander. It is common knowledge that simple geostrophic velocity calculations tend to overestimate velocities in regions of cyclonic curvature (trough)

and underestimate them in regions of anticyclonic curvature (crest) [*Holton*, 1992]. Using the surface geopotential anomaly contours to calculate curvature over the entire array area according to Equation 1.4, and using the calculated down-stream velocity transects for v_g, adjusted down-stream velocity transects including curvature effects (essentially the gradient wind balance) can be estimated by solving the quadratic equation:

$$\kappa v^2 + fv - fv_g = 0. \tag{1.6}$$

This adjustment reduces mean core velocities entering the trough from 1.4-1.5 m/s to 1.3-1.4 m/s and increases those in the crest from 1.2-1.3 m/s to 1.3-1.4 m/s, eliminating the apparent difference in maximum surface flow between the two regions. This continuity in velocity structure along the stream suggests that the KE possesses a "stiffness" similar to that documented by *Rossby and Zhang* [2001] in the Gulf Stream, which they correctly predicted would also be a prominent feature of the KE.

Mean cross-stream velocities near the surface in the crest (Figure 1.32, lower panel) seem to display a slight confluence from both sides of the core, although the errors associated with this mean suggest that only the southward surface flow less than 100 km north of the core is significantly different from zero. Although diffluence would be expected entering a crest, the apparent confluence here is not surprising as the 143.75°E line tends to represent the peak of the crest or just down-stream of the peak. The most significant feature to note here, however, is the deep-penetrating northward velocities across the jet of order 0.5-2 cm/s, which reveal a tendency for northward flux and upwelling in the crest in contrast to the southward flux and downwelling which were observed entering the trough. This represents the major difference between the crest and trough and again verifies previous results in both the Gulf Stream and the KE [*Bower*, 1991; *Kouketsu et al.*, 2005].

The down-stream deep velocities cover an even wider swath than was seen in the trough, spanning $>$300 km between zero contours, but they are weaker throughout the region, with magnitudes $<$5 cm/s below 2000 m. The contour pattern suggests less connection between the jet

and the bottom at this location, where the maximum deep down-stream velocities south of the core are likely due to summation of the KE jet flow with the deep flow of the southern recirculation gyre. The increase in the lateral span of the zero contours at the surface in comparison to the trough transect can also be explained by the presence of the southern recirculation gyre, whose down-stream flow at the surface augments down-stream flow within the jet in this region. The southern recirculation gyre at this location shows slightly stronger up-stream directed flows, reaching 0.3-0.4 m/s, which cover a slightly greater distance range from the core (250-450 km) than at the up-stream edge of the trough (250-400 km). The northern recirculation gyre does not extend this far west [*Qiu et al.*, 2008].

The time series (not shown) of down-stream velocities at the core ($X = 0$) again reveal variability between 1 and 2 m/s at the surface and between about -2 cm/s and 10 cm/s at the bottom. As in the trough, down-stream flow dominates at the core at the bottom but is occasionally replaced by weak up-stream flows. Cross-stream bottom velocities again show variability between northward and southward flow, with northward dominating in the crest. Figure 1.34 shows the mean down- and cross-stream bottom velocities in the crest, calculated from the mapped bottom current meter and pressure data, with errorbars indicating the standard error of the mean, calculated in the same manner as in the trough. This reveals the significance of the mean northward cross-stream bottom flow around the core and the mean down-stream bottom flow at and south of the core, as well as the off-centered nature of the down-stream bottom flow. The presence of the southern recirculation gyre is again clear, centered around 300 km south of the core, with bottom along-stream flows directed up-stream and cross-stream flows not statistically different from zero.

Trough to Crest

Looking at a transect at 148.5°E, which represents on average about halfway between the first meander trough and second meander crest, reveals even more about the along-stream evolution of the velocity structure. Maximum core velocities are again between 1.3-1.4 m/s, as found

in the adjusted velocity profiles in the crest and trough. Because curvature is virtually zero at the inflection point between trough and crest, no adjustment is necessary here. Although stream width between the 0.1 m/s contours at the surface remains fairly constant between the trough and the trough-to-crest locations ($\sim$190-200 km), down-stream flow at the bottom is significantly reduced beyond the trough (Figure 1.35), where the width between zero contours at the bottom is only $\sim$50 km, and mean bottom velocities near the core reach only to 2 cm/s as opposed to the $>$5 cm/s seen entering the trough. This maximum velocity region is again off-centered towards the south. It is possible that the summation of flows in the jet and the southern recirculation gyre in the more up-stream transects is responsible for this apparent reduction in down-stream flow at the easternmost transect. In contrast to the more up-stream sections, this easternmost transect shows stronger near-surface velocities in the northern recirculation gyre than the southern (Figure 1.35, $X \sim -150$), as expected given our knowledge of the locations of these gyres [*Qiu et al.*, 2008].

The profile of cross-stream velocity shows very small magnitude velocities of O(1 cm/s) surrounding the core region at all depths. The standard error of the mean cross-stream velocity (Figure 1.36) is in some places larger than the mean velocity itself, suggesting that in fact there is very little cross-stream flux here in the mean. This is also verified by examining the mean bottom cross-stream velocities as calculated from the mapped bottom current meters, shown in Figure 1.37, whose errorbars reveal them to be not statistically different from zero at and surrounding the core.

The time series (not shown) of surface down- and cross-stream velocities at the core again show variation at the surface from 1 m/s up to 2 m/s in the down-stream direction and down-stream bottom velocities varying between about -2 to 12 cm/s (occasional periods of weak up-stream flow). Bottom cross-stream velocities vary between northward and southward flows, with neither direction dominating, as discussed above.

Full Array

A plan view schematic of surface and bottom velocities plotted over mean SSH for the weakly meandering period provides context for the three sections discussed above (Figure 1.38). In order to create this schematic, mean absolute velocities as a function of distance from the core along the cross-stream line are calculated from the time series of stream-coordinate transects at any given phase in the meander pattern. These mean sections are then superimposed on the mean meander pattern by effectively co-locating each transect in a mean stream-coordinate system, in which the mean core location is defined as the mean latitude (and longitude, for the trough) of all cores in the time series, and the mean down-stream direction is the direction of the mean absolute velocity at the core. (see Figure 1.39 for an illustration of this procedure). In order to be included in the schematic in Figure 1.38, a time series at any one point is required to have sufficient data for five or more degrees of freedom and $<$200 bad points out of a possible 337 data points. These restrictions result in significant cropping of the transects beyond the central jet.

This schematic representation of the data (Figure 1.38) serves as a summary of some of the points discussed above, showing the tendency for rotation of the velocity vectors with depth as a function of location in the meander pattern. Locations where the rotation with depth is significant beyond the bounds of maximum possible directional error in the measurements are marked by orange circles. In the up-stream section at the crest the velocity vectors "veer" (rotate counterclockwise) with depth, so that deeper velocities are directed northwards across the jet in comparison to the surface flow. *Bower and Rossby* [1989] have shown in the Gulf Stream that this implies northward cross-stream transport and upwelling. In the middle section entering the trough, currents "back" (rotate clockwise) with depth, implying southward cross-stream transport and downwelling, and in the easternmost section, currents are very nearly vertically aligned, suggesting little cross-stream flow. These observations agree with others made by *Kouketsu et al.* [2005], who linked the intensity of southward transport of cool, fresh Oyashio water across the KE to backing with depth in meander troughs. In further support of these conclusions, the low-

salinity intrusion seen during the KESS feature surveys (Section 1.3.1) was observed to move southward across the front entering the meander trough. This schematic diagram also provides a visualization in the trough transect of the peeling-off of some of the down-stream flow into the southern recirculation gyre.

As was mentioned previously, the position of the meander trough was tracked over the time series in order to produce the mean cross-section entering the trough. If instead a fixed longitude of 146.4°E is used to represent the mean location of the up-stream edge of the trough, the clockwise rotation with depth in the trough seen in Figure 1.38 is all but eliminated. This is due to the fact that although the mean longitude entering the trough is 146.4°E, it is rarely actually found in that position during the 5.5-month time series and moves significantly over a wide longitudinal range. This observation provides further support for the idea that it is the meander trough itself (or troughs of frontal waves) that is inducing the southward cross-stream flow.

Examining surface and bottom velocities along the full length of the meander pattern in plan view provides a more continuous overview of the along-stream variation in velocity structure. Figures 1.40 and 1.41 show the mean surface and bottom velocities along cross-stream transects at $\frac{1}{8}^{th}$-degree longitudinal separation. The same basic averaging procedure and data quality criteria described above are used, except each transect here represents a fixed longitude rather than a phase in the meander pattern. Although these illustrations are quite cluttered, several important features can be discerned. The surface velocities clearly show the jet following the meander pattern of the SSH contours and the southern recirculation gyre beneath the first meander crest and trough. The bottom velocities also display a meander pattern in the first crest to trough area, but the pattern is suggestive of a steeper meander, with increased cross-stream displacement to the north in the crest and to the south in the trough. This behavior is in keeping with the kinematic exchange mechanism proposed by *Bower* [1991], whereby water parcels with lower zonal (u) velocities (that is, parcels near the edges of the jet or at greater depths) exhibit a greater amplitude of cross-stream motion in a meandering jet whose meander pattern propagates at some

eastward phase speed $c < u$. Also evident in the bottom velocities is the mean presence of a deep cyclonic eddy at the up-stream northern edge of the first meander trough, centered at (450, 450) km in Figure 1.41. This feature is likely responsible for some of the up-stream flows seen in the time series of bottom velocities at the core entering the trough (Figure 1.30) and accounts for the mean up-stream velocity north of the core at this location (Figure 1.31). It is unclear whether this eddy forms part of the northern recirculation gyre, but it appears to be on a smaller spatial scale than the mean gyre as a whole as proposed by other studies. *Qiu et al.* [2008] have found the northern recirculation to extend as far as 40°N, 156°E at 1500 m from a multiyear mean of profiling float data. However, inspection of the 1500 dbar streamfunction from the KESS CPIES data does not reveal a larger recirculation (*D. R. Watts,* personal communication), so it is possible that the shorter averaging period in KESS is contributing to this different picture of the gyre.

Contour plots of down- and cross-stream velocities at the surface and bottom generated from the individual transects described above provide another means of examining the along-stream evolution of the velocity structure. Figure 1.42 shows mean down-stream velocities at the surface and their standard error. Here again is evidence of a slight narrowing of the zero contours spanning the jet between crest and trough, with the excess width in the crest largely attributable to the 0-0.2 m/s range south of the core and most likely representing summation with the southern recirculation gyre. Also of note here is the apparent mean presence of "jet streaks," regions of increased down-stream velocity observed to develop in the Gulf Stream near inflection points between meander crests and troughs [*Howden and Watts*, 1999]. Figure 1.43 shows that bottom down-stream velocities extend further north in the crest and further south in the trough than the surface zero contour, as expected given the meander pattern seen in the velocity vectors in Figure 1.41. Also apparent is the extreme narrowing of the down-stream bottom flow in the jet between the first crest and trough (around zonal distance = 350 km in the figure). This may be in part due to the southern recirculation gyre but is also suggestive of a decrease in the vertical penetration of the jet structure with down-stream progression. The local maximum of down-stream bottom velocity near the inflection region between crest and trough may correspond to the nearby

surface "jet streak," though it is slightly offset to the south. However, as these plots represent the time-mean structure rather than a time-varying evolution, it is difficult to determine whether these features are in fact linked and analogous to the jet streaks seen in the Gulf Stream. Further investigation of the time series at these locations could provide a better indication of the nature of these local maxima. Cross-stream bottom velocities, shown in Figure 1.44, again confirm our expectation over the whole array region of northward cross-stream flow heading into meander crests and southward flow heading into troughs. Northward flow resumes again on the down-stream edge of the trough. In the center panel of this figure, areas where the magnitude of the cross-stream flow is less than the magnitude of the associated standard error have been masked out to indicate the regions where cross-stream flow is most significant. The apparent up-stream offset of the strongest southward flows from the meander trough may be due to the longitudinal variation in trough location over the course of the time series. Standard errors for the bottom mean down- and cross-stream velocities are also shown in Figures 1.43 and 1.44. The error maps show that, as previously noted, mean bottom velocities in both down- and cross-stream directions are small but significant.

1.4.2 Potential Vorticity Structure

The basic features of the mean PV structure obtained from the CPIES dataset entering the trough closely resemble those seen in the ADCP surveys, with differences arising from the coarser horizontal resolution and smoothing due to the assumption of strict GEM behavior. Figure 1.45 is very similar to Figure 1.16, displaying the same high-PV band following isopycnals down across the core, low-PV mode water, and high-PV surface waters as were seen in the surveys, with PV values of $O(10^{-10}$-10^{-9} m^{-1}s$^{-1})$. We can again distinguish the four isopycnal layers of varying PV gradients at the mode water depth, the main thermocline, the lower thermocline/NPIW core, and the deep layer, where we find that the gradient across the core is of $O(10^{-17}$ m^{-2}s$^{-1})$, or $<$ 1% of $\frac{\beta}{H}$ in most locations (Figure 1.46). Slightly lower values of total PV are seen in the CPIES data than in the surveys in the thermocline region crossing the core, from about 150 m depth 20 km north of the core down to $\sim$500 m depth 45 km south of the core. The reduced magnitude

of the portion north of the core can be attributed to the reduction in magnitude of both the shear (Figure 1.47) and twisting (Figure 1.48) vorticity terms calculated from the CPIES dataset, while the portion south of the core is attributable to changes in the twisting and thickness (Figure 1.49) terms. These differences are due to the low resolution of the CPIES data, which results in a reduction of maximum values of $\frac{\partial \rho}{\partial X}$, $\frac{\partial V}{\partial z}$, and $\frac{\partial V}{\partial X}$ over those in the survey data by factors of about two, four, and three, respectively, as well as to the GEM method, which causes smoothing of all these quantities and of N^2 and does not attempt to resolve the surface mixed layer. Artificially high values of N^2 at the surface in the CPIES dataset cause the increased horizontal range of the shear vorticity term (ζ) and increased total PV at the surface.

Although the reduced resolution of the CPIES data does impact calculations of PV by weakening gradients, other aspects of the dataset make it invaluable in further examining the PV structure of the KE. The first of these benefits is that the total ζ term can be calculated, including the $\frac{\partial U}{\partial Y}$ term rather than the curvature (κV) term, which could not be obtained from the survey data. As described in Section 1.2.3, $\frac{\partial U}{\partial Y}$ is calculated from the CPIES both in stream coordinates as the along-stream gradient of the cross-stream velocity, and as part of $\frac{\partial v}{\partial x} - \frac{\partial u}{\partial y}$ from the full array, where x-y and u-v refer to the standard east-north coordinate system. Comparing the two methods shows that both produce similar results for the total relative vorticity. Using the stream-coordinates method, the relative magnitudes of the $\frac{\partial V}{\partial X}$ and $\frac{\partial U}{\partial Y}$ terms can be compared. They are shown for the transect entering the trough in Figure 1.50 as percentages of f. As expected, the cross-stream shear of down-stream velocity $\left(\frac{\partial V}{\partial X}\right)$ makes a significantly larger contribution, averaging 24-28% of f at its maximum near the surface in the region of cyclonic shear, about 25 to 50 km north of the core. South of the core, in the weaker anticyclonic shear, $\frac{\partial V}{\partial X}$ reaches a maximum of -16 to -20% of f. The along-stream gradient of cross-stream velocity $\left(\frac{\partial U}{\partial Y}\right)$ makes a smaller but non-negligible contribution, averaging -12 to -16% of f near the surface at and north of the core, with mean small negative contributions across the central jet region. The addition of the $-\frac{\partial U}{\partial Y}$ term strengthens the relative vorticity on the cyclonic side of the jet, bringing it up to a maximum of 40% of f near the surface while weakening it very slightly on the anticyclonic side.

As with the velocity structure, the CPIES dataset also allows us to examine along-stream differences in PV structure. Using the 143.75°E section again to represent the down-stream edge of the meander crest, several differences between the crest and the trough can be observed. Total PV (Figure 1.51) shows a very similar pattern in both locations on the northern side of the jet, although high PV appears to reach to slightly deeper isopycnals in the mean entering the trough. South of the core, the low-PV mode water shows up again around $\sigma_\theta \sim 25.1$ kg/m^3 but obtains even lower PV in the crest than was seen in the trough, reaching down below zero around 200 km south of the core. Upon breaking the total PV into its components, we see that this is attributable to a lower thickness vorticity in the mode water region (Figure 1.52) than was seen entering the trough. Total PV is also slightly lower at the crest along the isopycnals of the main thermocline south of the core. This difference is not due to thickness vorticity but to the increased strength of the ζ term on the anticyclonic side of the crest. The ratio of the cross-stream gradient of down-stream velocity to f $\left(\frac{\partial V}{\partial X}/f\right)$ is almost symmetrical about the core in the crest and weaker on both sides than entering the trough, and the $\frac{\partial U}{\partial Y}$ term in this location serves to strengthen the shear vorticity on the anticyclonic side (Figure 1.53), since the crest is a region of anticyclonic curvature. As a result, the contribution of the ζ term to the total PV south of the core is significantly more negative in the crest than entering the trough, reaching -20 to -24% of f as compared to -16% entering the trough, while the contribution north of the core is much weaker, reaching a maximum of only 20% of f as opposed to 40% entering the trough.

Down-stream of the trough, at 148.5°E, the total PV profile (Figure 1.54) is again very similar to that entering the trough, north of and at the core. South of the core, the mode water has the same PV value as at the trough, but the PV along the isopycnals of the main thermocline is even further reduced than it was in the crest, reaching only half the values seen entering the trough at some locations. Figure 1.55 shows that the asymmetry of the $\frac{\partial V}{\partial X}$ term is retained and slightly increased over that entering the trough, with slightly greater values of $\frac{\partial V}{\partial X}/f$ on the cyclonic side and slightly lower values on the ancticyclonic side. However, the $\frac{\partial U}{\partial Y}$ term here tends to decrease

the asymmetry, leading to a total shear term that is only slightly larger on the cyclonic side, at a maximum of 24-28% of f compared to -20 to -24% of f on the anticyclonic side.

The time series from the CPIES provides an opportunity to examine the variability of the PV structure within the weakly meandering period. Returning to the trough transects, the time series of total PV shows that while the overall shape of the PV structure remains nearly constant, its location along the cross-stream axis shifts with respect to the core (see Figure 1.56). *Rajamony et al.* [2001] observed similar behavior of PV structure across the front in the Gulf Stream, which they linked during an isopycnal RAFOS float study to cross-stream motion of the floats, suggesting that despite the barrier imposed by the PV gradient itself, cross-stream motion is possible in the center of the jet near the surface to the extent that the PV structure shifts across the front. Although float data are not available for this study of the KE to verify the cross-stream motion of water parcels, the shifting PV structure observed from the CPIES suggests that the same mechanism may be at work here.

1.5 Comparison with the Gulf Stream

Mention of the Gulf Stream and its shared characteristics with the KE has been made at various times throughout the above discussion. Many similarities are expected between the two, as both are western boundary currents of large ocean basins. In this section, a brief statistical summary and comparison of the two currents is provided.

The average strength of the down-stream component of velocity in the Gulf Stream has been found in multiple studies to exceed that observed in the KE. As Table 1.2 shows, *Halkin and Rossby* [1985] found an average maximum down-stream velocity of 1.69 m/s in the Gulf Stream, at a location relatively further up-stream than the KESS region. *Liu and Rossby* [1993], *Rossby and Gottlieb* [1998], and *Rossby and Zhang* [2001] all found average maxima of 2 m/s or greater. *Johns et al.* [1995] also found an average maximum down-stream velocity of almost 2 m/s from the SYNOP central array data, which was a comparable experiment to KESS in location and

instrumentation, although a recent revisit of this dataset produced a slightly reduced estimate of 1.6-1.8 m/s [*Meinen et al.*, 2008]. The combination of these studies suggests a range in the maximum strength of the down-stream component of the Gulf Stream jet of 1.5-2.5 m/s. In contrast, the present study has found an average maximum down-stream velocity in the KE of about 1.4 m/s, with a range of 1.0-2.0 m/s. A mooring study by *Hall* [1989] also suggested that maximum down-stream velocities in the Gulf Stream exceed those of the KE, although surface values were not available in her study. In addition, the strong jet structure of the Gulf Stream appears to penetrate to greater depths than that of the KE, with maximum down-stream velocities of 60-80 cm/s seen at 700 m [*Johns et al.*, 1995; *Meinen et al.*, 2008] compared to 45 cm/s in the KE (Figure 1.28).

Although the mean total PV cross-section in the Gulf Stream has a similar structure to that observed here in the KE, with PV values of $O(10^{-10})$, several differences can quickly be identified. The mean stream-coordinates PV section found by *Meinen et al.* [2008] in the Gulf Stream shows the low-PV mode water region south of the core reaching down to 600 dbar ($\sim$ 594 m), whereas in the KE the mode water extends only to 4-500 m depth. The PV following the isopycnals of the main thermocline in the Gulf Stream is also about 50% less at and south of the core than that in the KE. These differences simply reflect the thicker and deeper mode water signature in the Gulf Stream and suggest a stronger density front, which thermal wind indicates is consistent with the stronger maximum velocities noted above. Also consistent with a sharper front in the Gulf Stream is the observation of stronger lateral shear vorticity components on both sides of the jet. *Liu and Rossby* [1993] found cross-stream shear of down-stream velocity $\left(\frac{\partial V}{\partial X}\right)$ on the cyclonic side of the Gulf Stream ranging from 80 to $>$120% of f, with anticyclonic shear sometimes exceeding -40% of f. The survey data from the KE, however, show a maximum of $\sim$ 72% of f north of the core and -41% of f to the south. Neither of these sets of values represents a long-term mean, but a comparison of the KESS CPIES measurements with the PIES measurements from the SYNOP data discussed in *Meinen et al.* [2008] may also be considered. The Gulf Stream data show $\frac{\partial V}{\partial X}$ reaching a maximum of 40% of f on the cyclonic side of the jet

and -28% of f on the anticyclonic side, as compared with 20-24% and -16 to -20% of f in the KE. Values of $\frac{\partial U}{\partial Y}$ in the section of the Gulf Stream discussed by *Meinen et al.* [2008] reach up to 12% of f, while the KE shows mean values of up to -16% of f entering the trough and only 4% of f in the crest. Combining these terms, the ratio of ζ to f in the Gulf Stream shows a cyclonic maximum of 32% and a deeper negative maximum on the anticyclonic side of -28%. In the KE entering the trough, the cyclonic maximum is 40% of f with a deeper negative maximum on the anticyclonic side of -16 to -20% of f. In the crest, however, the cyclonic maximum is only 20% of f, with the deeper maximum on the anticyclonic side reaching -20 to -24% of f. The SYNOP data were not specific to a crest or trough in the Gulf Stream, and the resulting value for ζ/f on the cyclonic side lies in between the values found in the crest and trough of the KE.

Although the general similarity of the structures of the two currents has been mentioned and only minor differences of magnitude of certain of their characteristics have been discussed, it should be remembered that this refers only to the KE while it remains in its weakly meandering state. The oscillation of the KE between weakly and strongly meandering states represents a significant difference between the two currents, and it is possible that it is when the KE enters the strongly meandering state that more striking differences between its structure and that of the Gulf Stream may emerge.

1.6 Conclusion

In May of 2004, during the deployment of an array of 46 CPIES that formed part of KESS, four fine horizontal-scale ADCP/CTD surveys of the KE were performed just up-stream of the first meander trough to determine the synoptic structure of the current at this location. These sections were analyzed in a stream-coordinate system, whose origin (the *core*) was defined by the location of the maximum velocity vector after averaging over 100-300 m to reduce the effects of noise and surface wind-induced flow and then gridding to 5-km horizontal spacing. The down-stream axis was oriented in the direction of the vector average of the three vertically-averaged ADCP vectors centered on the core. This method was chosen over more traditional, hydrography-based

methods because of small-scale variability observed in the hydrography and the existence in the dataset of several additional ADCP cross-sections that were not accompanied by CTD data.

This analysis produced a picture of the KE velocity structure that includes many of the canonical features of a baroclinic jet. The velocity maximum, located about 10 km north of the core at the surface, shifts southward with depth, reaching 20 km south of the core at 400 m. In addition, a slight subsurface velocity maximum exists on the anticyclonic side of the jet. The cross-stream velocity shear exhibits an asymmetry similar to that seen in studies of the Gulf Stream, with larger shear on the northern, cyclonic side of the jet.

Despite the coarser horizontal resolution, producing stream-coordinates sections from the CPIES data provides further indication of the long-term mean and full water-column structure, as well as evidence of along-stream variability. The 5.5-month time series during the weakly meandering state reveals surface down-stream core velocities averaging 1.4 m/s and varying between 1 and 2 m/s and down-stream velocities around 5 cm/s extending to the bottom at times, depending upon the location of deep barotropic eddies. A slight narrowing of the down-stream flow with eastward progression along the meander is apparent, but most of the excess flow in up-stream regions likely constitutes the summation of the jet with the southern recirculation gyre. Down-stream flow at the bottom also grows significantly narrower and weaker with along-stream progression. Mean cross-stream flow patterns indicate northward transport and upwelling in the first meander crest and southward transport and downwelling approaching the first meander trough, with cross-stream velocities across the core of the order 1-2 cm/s that are relatively depth-independent below $\sim$550 m. Despite these mean tendencies, cross-stream velocities in both crest and trough alternate between northward and southward flows with respect to the jet axis and reach magnitudes $>$10 cm/s, suggesting an event-driven process which is significantly correlated with the slope of the meander pattern ($r = 0.68$) in the trough but may also be attributable to other mechanisms.

Calculations of PV from the surveys and the CPIES produce a similar picture of its structure across the front. Low-PV mode water is evident in all sections between about 200 and 500 m depth beginning about 50 km south of the core. At these densities, about $\sigma_\theta \sim 25.1$ to 25.5 kg/m^3, a strong PV gradient exists across the front, acting as a 'barrier' to cross-frontal exchange. A pattern of slightly higher PV can be seen to follow isopycnals down through the thermocline, between $\sigma_\theta \sim 25.5$ and 26.4 kg/m^3, where a slightly weaker PV gradient exists across the jet. At the base of the thermocline, between $\sigma_\theta \sim 26.4$ and 27.1 kg/m^3, a reversal occurs in the sign of the PV gradient. PV values are slightly lower to the north of the core here than to the south, but the gradient is very weak, suggesting the beginning of the 'blender' region where free exchange is possible. Below the thermocline, or below $\sigma_\theta \sim 27.1$ kg/m^3, the blender region continues, and the PV gradient across the front is less than 1% of $\frac{\beta}{H}$ in most locations. The time series of the PV structure entering the trough reveals that while it generally maintains its basic shape, the structure as a whole shifts in time laterally across the front with respect to the core. *Rajamony et al.* [2001] observed in a Lagrangian float study that similar shifting of PV gradients in the Gulf Stream serves to transport water parcels across the front despite the apparent PV barrier. Rough calculations reveal that this shifting can reach "speeds" ($\frac{\Delta x}{\Delta t}$) of O(10-20 cm/s), which is significantly greater than mean cross-stream velocity magnitudes but agrees on the lower end with the maximum cross-stream flows of O(10-12 cm/s) seen in the time series.

Finally, comparing the KE to the Gulf Stream reveals that the two share the same basic structure of a baroclinic jet, but the Gulf Stream attains greater maximum surface currents, ranging between 1.5 and 2.5 m/s, and shows a deeper expression of the high velocity jet structure. Although both systems display the asymmetric lateral shear structure, both cyclonic and anticyclonic shears are in general stronger in the Gulf Stream. These differences are suggestive of a stronger, deeper density front in the Gulf Stream. As would be expected given these observations, PV gradients across the jet appear to be somewhat stronger in the Gulf Stream, but a similar division into four isopycnal 'barrier/blender' layers can still be made.

Beyond the simple benefit of providing a picture of the general structure of the KE current, which has heretofore been missing from the literature, the results of this study will be of value as a basis for future work in various areas. Knowledge of the mean structure of the KE will aid in the identification and quantification of regions of cross-frontal exchange, which is critical in the formation of NPIW and mode water and plays a significant role in heat and nutrient flux in the larger North Pacific. In addition, the physical model of the KE resulting from this work can be used in future theoretical studies to assess the stability of the current. The values of the structural properties of the current observed and calculated here may also be of use as quantitative metrics with which to assess the performance of complex numerical models.

Table 1.1

Dates and Locations in Meander Pattern of Feature Survey Crossings

Crossing No.	**Date in 2004 [mon/day]**	**Location**	**CTD Data**
1	5/1 - 5/2	trough	Y
2	5/2 - 5/3	trough	Y
3	5/3 - 5/5	trough	Y
4	5/5 - 5/6	trough	Y
5	5/1	trough	N
6	5/7	crest to trough	N
7	5/18	crest	N
8	5/28	trough	N

Table 1.2

Comparison of Various Characteristics of Gulf Stream and KE

Attribute	**Gulf Stream**	**Kuroshio Extension**
Down-stream Max. Velocity Average	$\sim$ 2 - $>$ 2 m/s [2,3,4,5]; 1.6 - 1.8 m/s [1,6]	1.4 m/s
Down-stream Max. Velocity Range	1.5 - 2.5 m/s [1,2,3,4,5,6]	1.0 - 2.0 m/s
Max. Down-stream Velocity at 700 m	0.6 - 0.8 m/s [5,6]	0.4 - 0.5 m/s
Ratio of $\frac{\partial V}{\partial X}$ to f as percentage	80-120%(-40%) [2], 40%(-28%) [6]	72%(-41%), 20-24%(-16 to -20%)
Ratio of $\frac{\partial U}{\partial Y}$ to f as percentage	12% [6]	trough: -16%, crest: 4%
Ratio of ζ to f as percentage	32%(-28%) [6]	trough: 40%(-16 to -20%), crest: 20%(-20 to -24%)

Note. Percentages in parentheses refer to anticyclonic side.
[1]*Halkin and Rossby* [1985], [2]*Liu and Rossby* [1993], [3]*Rossby and Gottlieb* [1998], [4]*Rossby and Zhang* [2001], [5]*Johns et al.* [1995], [6]*Meinen et al.* [2008]

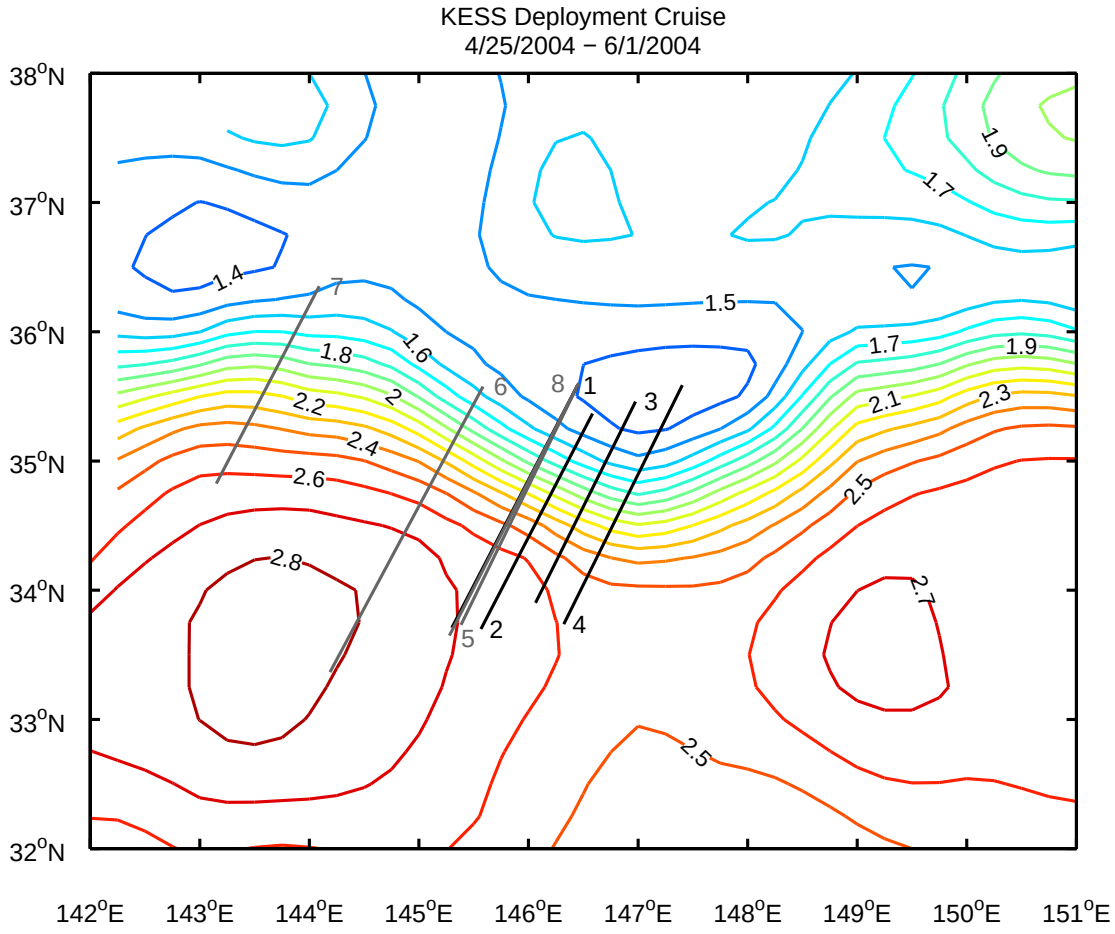

Figure 1.1: Mean SSH over the period of the deployment cruise in meters referenced to 1500 dbar from AVISO Rio05. Black and gray lines are feature survey crossings. Crossings 5-8 were not accompanied by CTD casts.

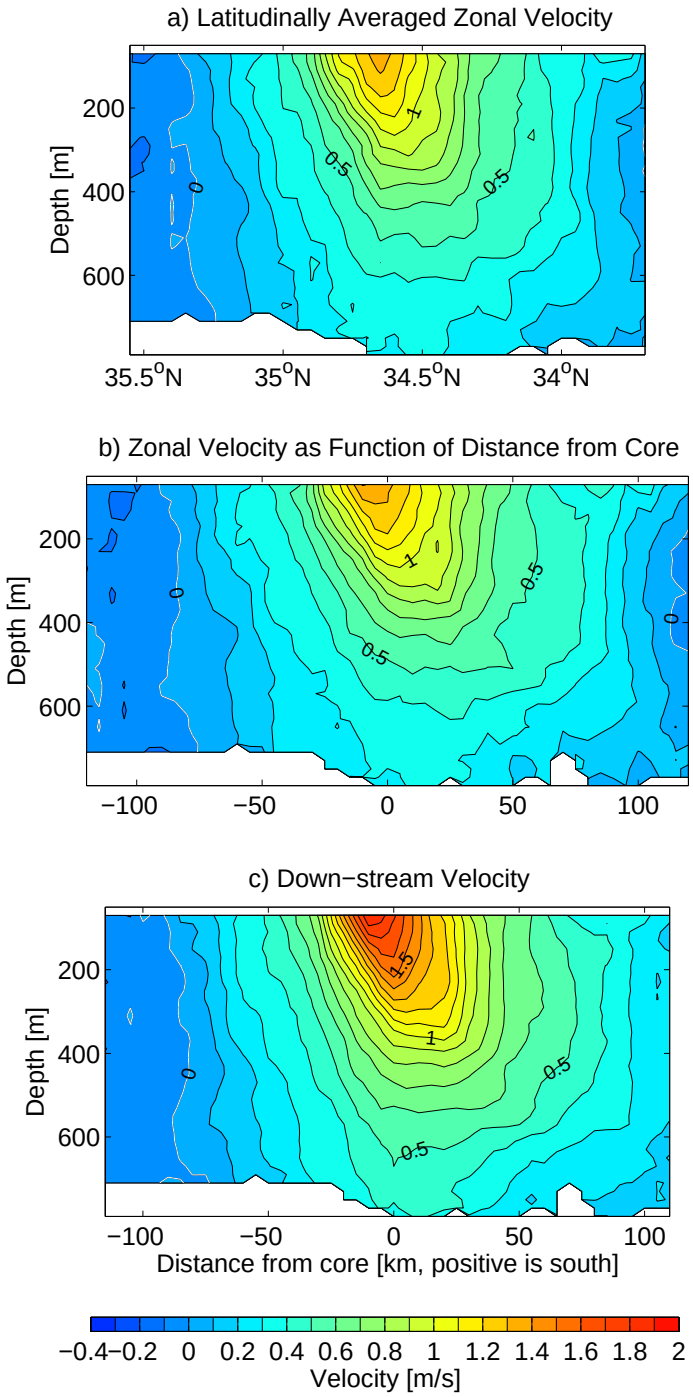

Figure 1.2: Data from crossings 1-4 (see Figure 1.1a) contoured in three different ways with the same color-scale. (a) Zonal velocities from original ADCP data gridded to .05° latitude increments and averaged. (b) Zonal velocities from original ADCP data gridded to 5 km along actual ship track lines and averaged according to distance from the core. (c) Data rotated into the stream-coordinate system, gridded to 5 km along the new rotated transect line, and averaged according to distance from the core. Note the increased magnitude of velocities and gradients in the stream-coordinate system.

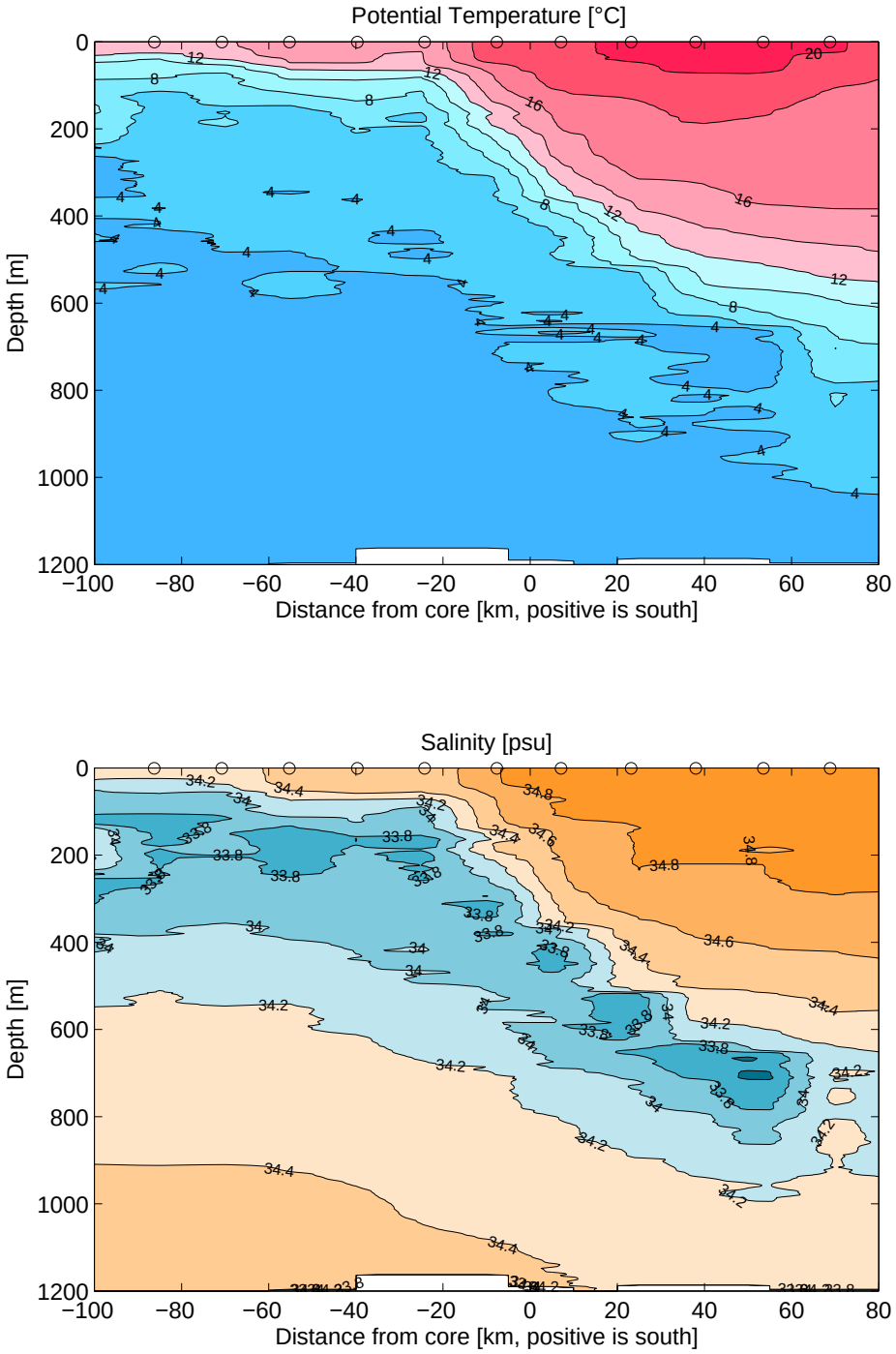

Figure 1.3: Potential temperature and salinity from Crossing 3 (see Figure 1.1). High vertical wavenumber variability apparent in the temperature data discourages the use of hydrography in defining the stream-coordinates core, as it may introduce up to 15 km lateral ambiguity in core location. Also visible are warm surface waters that have been advected within the core on the southern side from lower latitudes, resulting in surface waters on the southern edge of the jet that are actually warmer than the surface waters further south. This creates negative thermal wind shear on the anticyclonic side of the core.

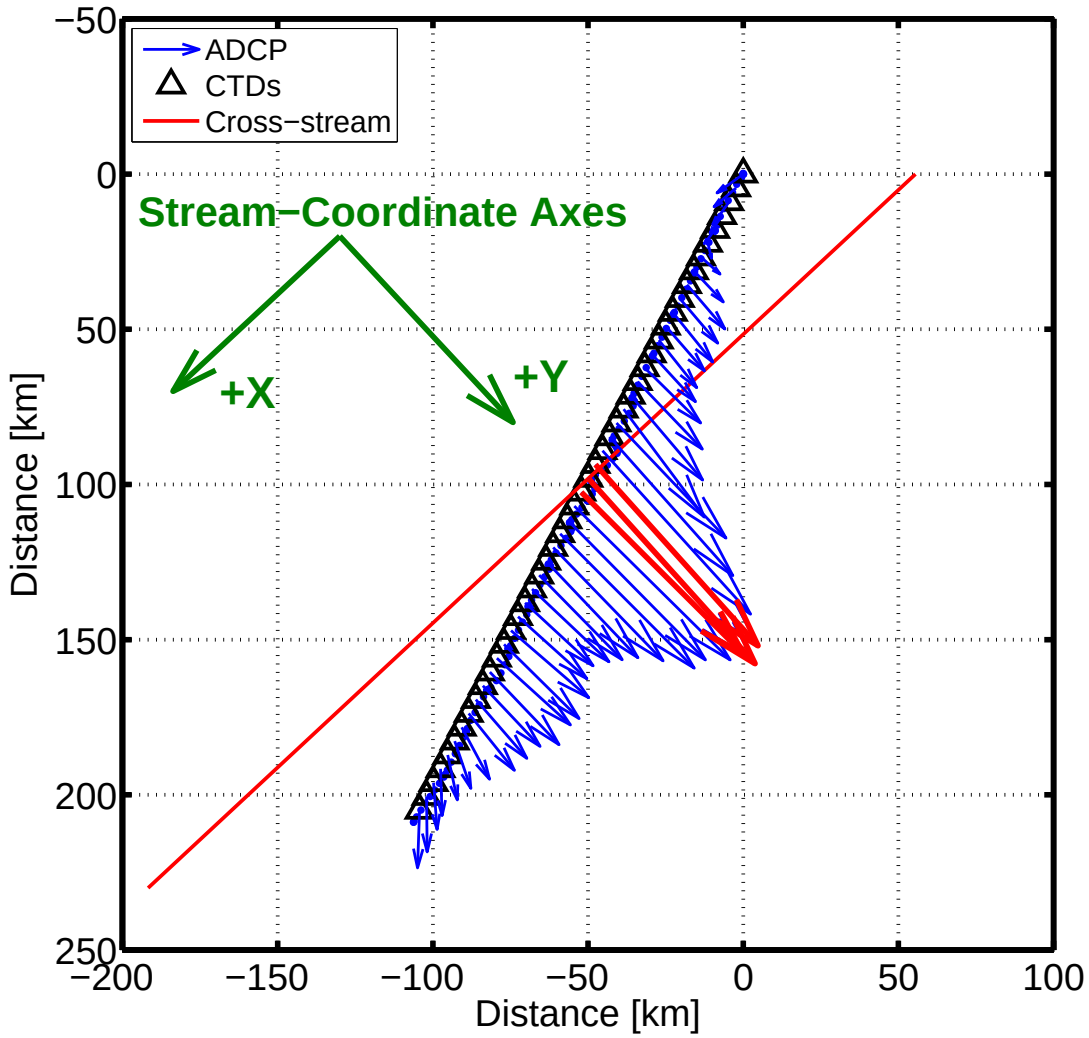

Figure 1.4: Sample transect showing 100-300 m averaged and 5-km gridded velocities and 5-km gridded CTD data points. Core and surrounding two vectors highlighted in red are averaged to define down-stream direction. Red line indicates resultant cross-stream line. CTD and ADCP data are then projected along the down-stream direction onto the cross-stream line. See Figure 1.5 for diagram of rotation procedure.

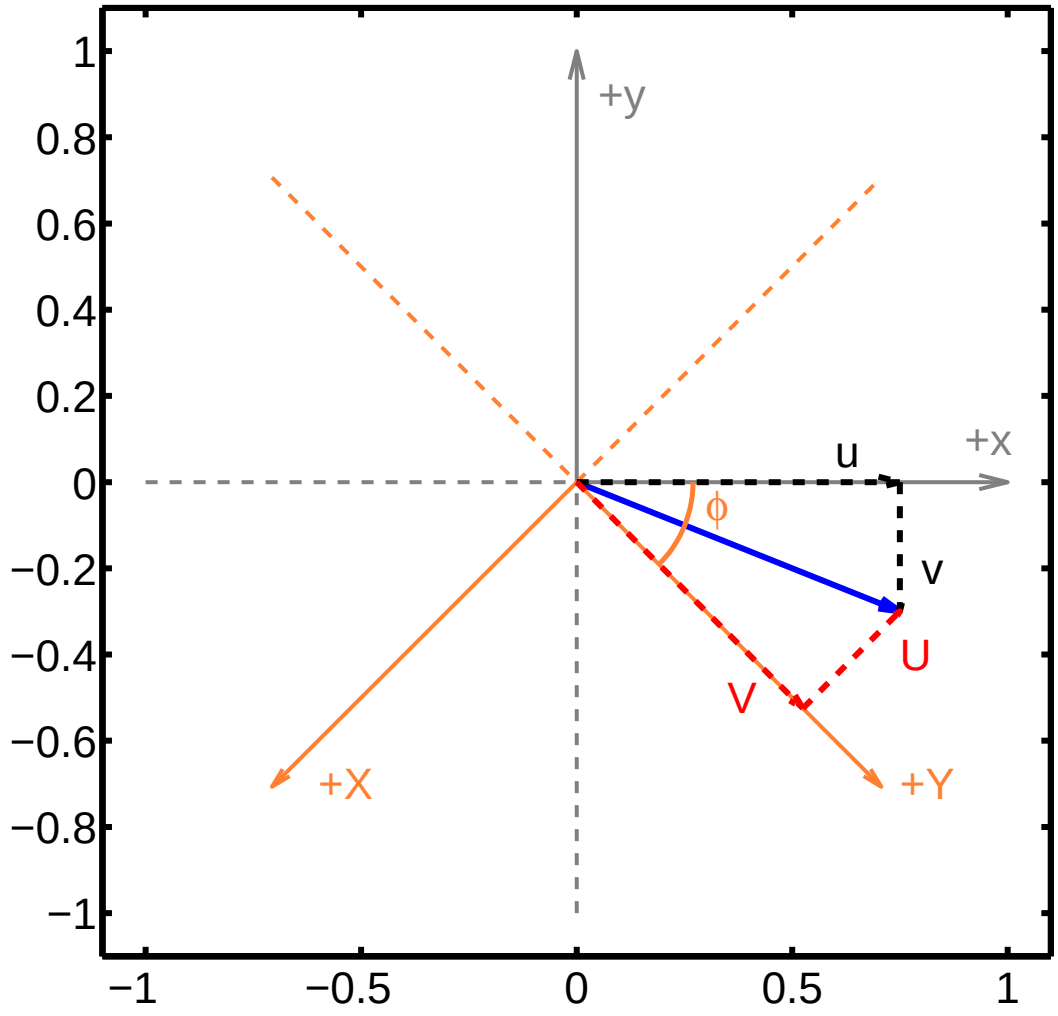

Figure 1.5: Diagram of rotation procedure to translate ADCP velocities into stream-coordinate down- and cross-stream components. ϕ is the sample down-stream direction, measured from 0 pointing due east. Gray axes indicate original east-north coordinate system. Orange axes indicate the orientation of the stream coordinate system, rotated clockwise from east-north by $\frac{\pi}{2} - \phi$, where in this case $\phi < 0$. The origin is centered at each 5-km gridded output velocity from the ADCP. The solid blue vector represents one such ADCP absolute velocity, which has dashed black east-north components (u, v) and dashed red cross-stream and down-stream components (U, V) in the stream-coordinate system. The transformation between coordinate system components is performed according to Equations 1.1a and b.

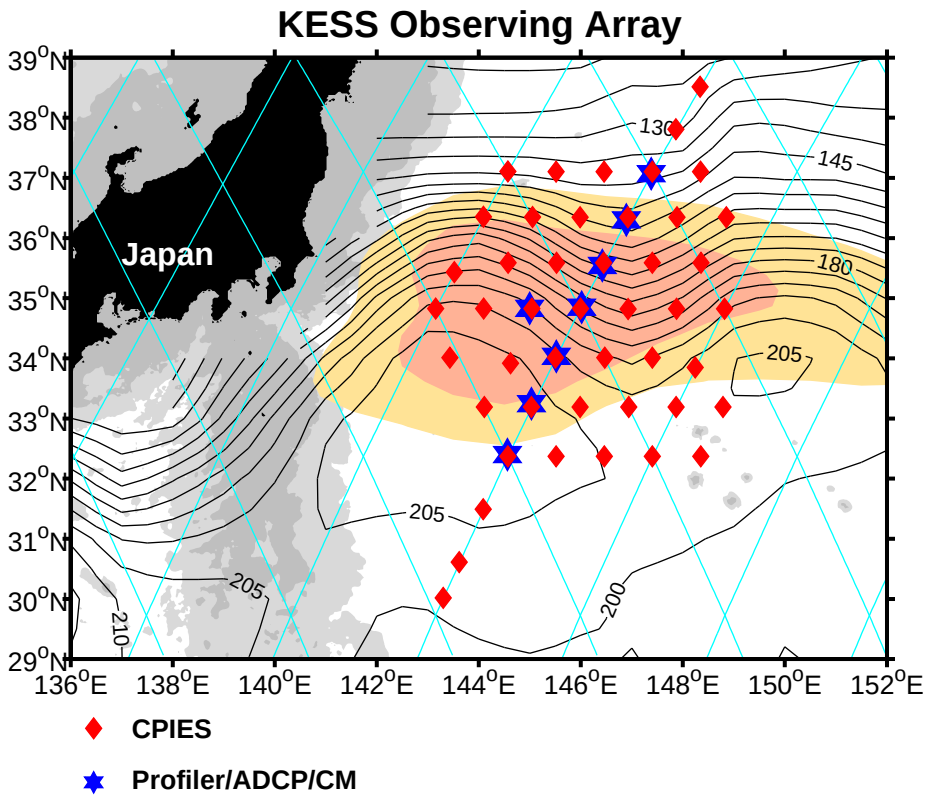

Figure 1.6: KESS instrument array. 46 PIES and CPIES (red diamonds) at horizontal spacings of 84 km and diagonal spacings of 94 km. Eight tall moorings (blue stars) included upward-looking ADCPs at 250 m, McLane moored profilers between 250-1500 m, and deep current meters at 1500, 2000, 3500, and 5000 m. Solid black lines in the figure are the Generalized Digital Environmental Model mean surface dynamic height contours in dyn-cm referenced to 1000 dbar from *Teague et al.* [1990]. The 2000 and 4000-m isobaths are shaded dark and light gray, respectively. Eddy kinetic energy determined from satellite sea surface height anomaly $>$ 0.18 and 0.24 $m^2 s^{-2}$ is color shaded yellow and orange, respectively.

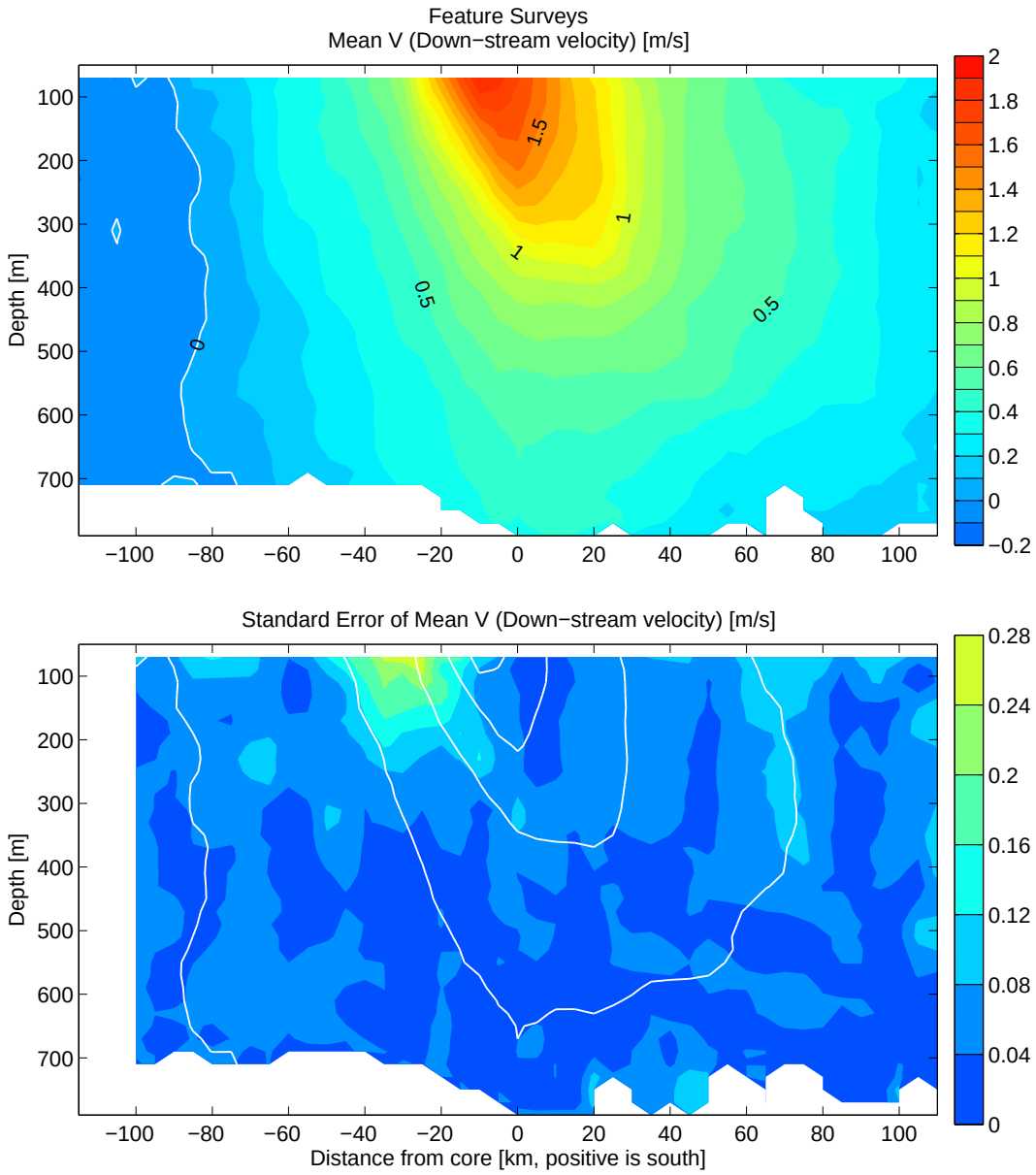

Figure 1.7: (top) Mean down-stream velocities from feature survey Crossings 1-4. White contour indicates zero down-stream velocity. The location of the maximum velocity shifts downward to the right, and a subsurface maximum is seen south of the core induced by the negative thermal wind shear to the right of the warm near-surface core. (bottom) Standard error of mean down-stream velocities. White contours indicate 0, 0.5, 1, 1.5, and 1.8 m/s mean down-stream velocities from top panel for context.

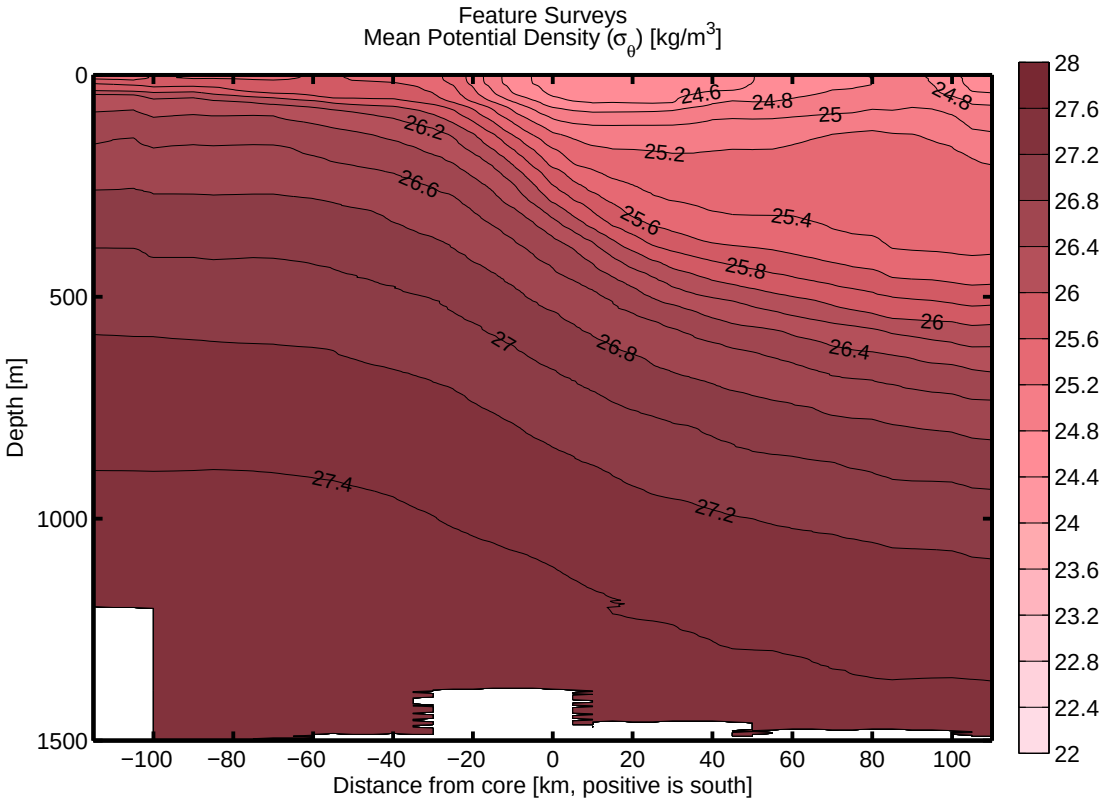

Figure 1.8: Mean potential density for feature survey Crossings 1-4. A region of negative thermal wind shear is apparent south of the core due to advection within the core of warm surface waters from lower latitudes.

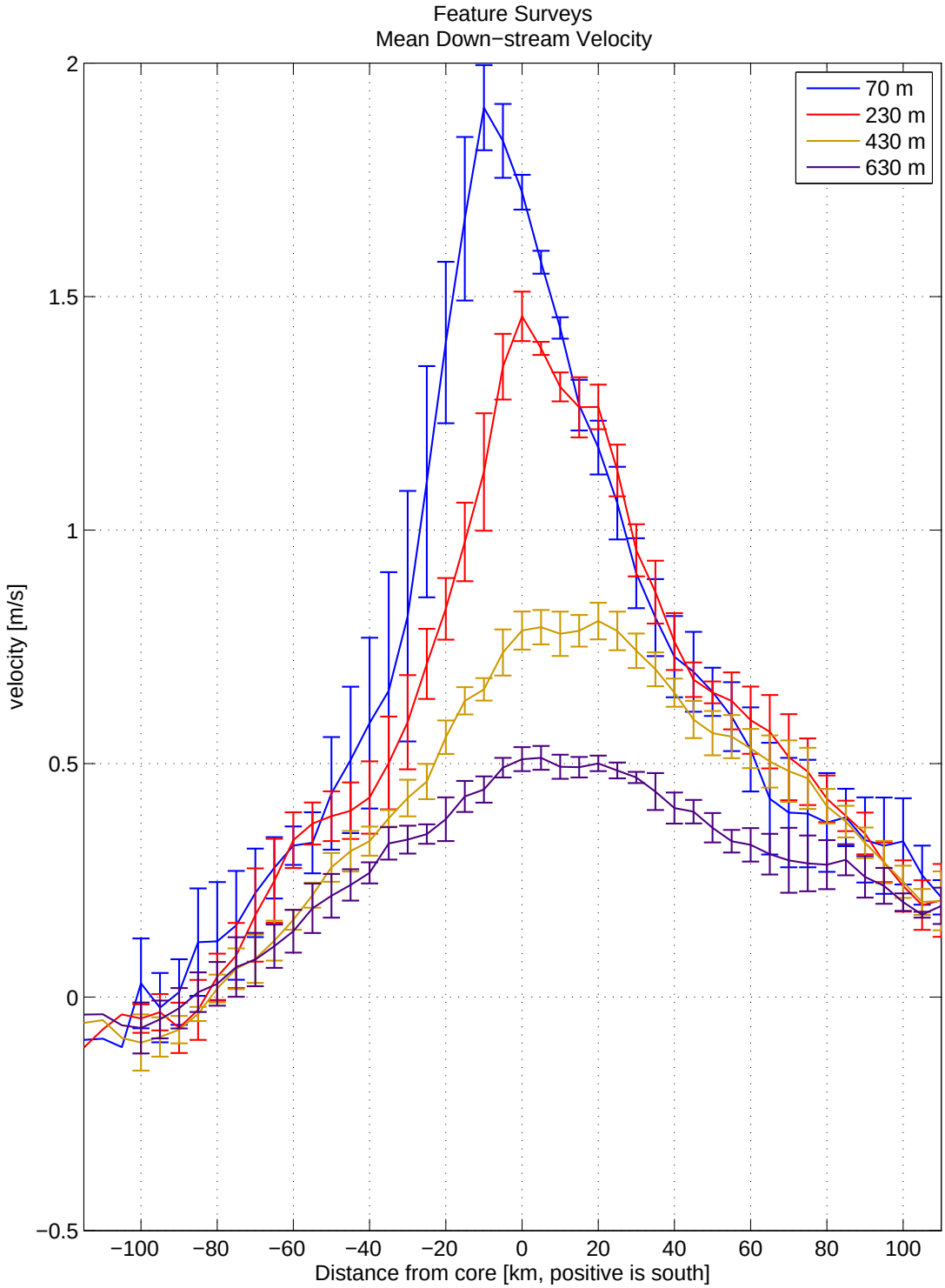

Figure 1.9: Mean down-stream velocities at depths indicated by the key. Errorbars indicate standard error.

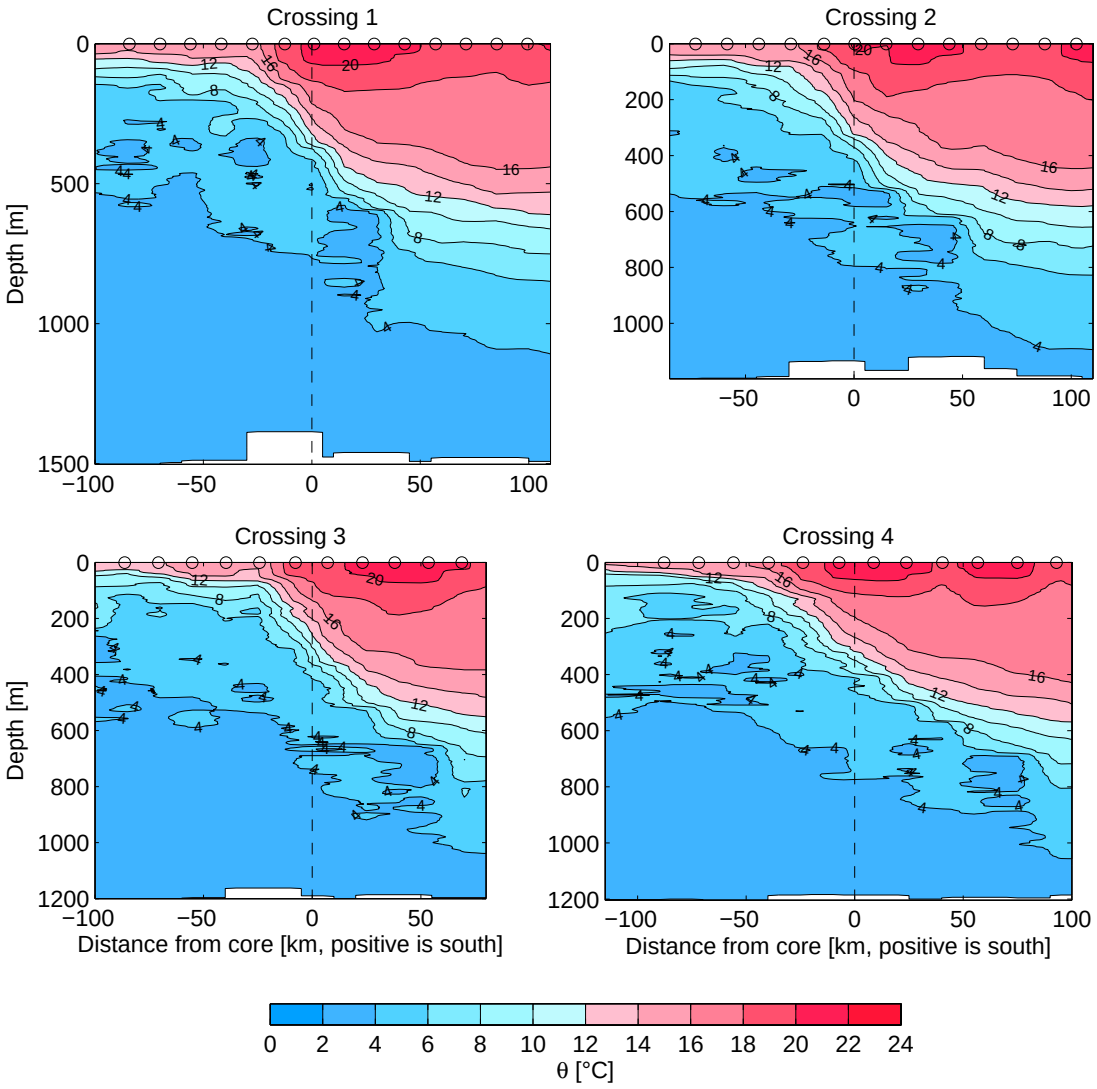

Figure 1.10: Potential temperature for individual feature survey Crossings 1-4. All plots have the same aspect ratio. Black circles indicate locations of CTD casts. Dashed black lines indicate location of core. Note the presence of warm surface waters at and south of the core and the reversal of the horizontal temperature gradient in some locations both north and south of the core.

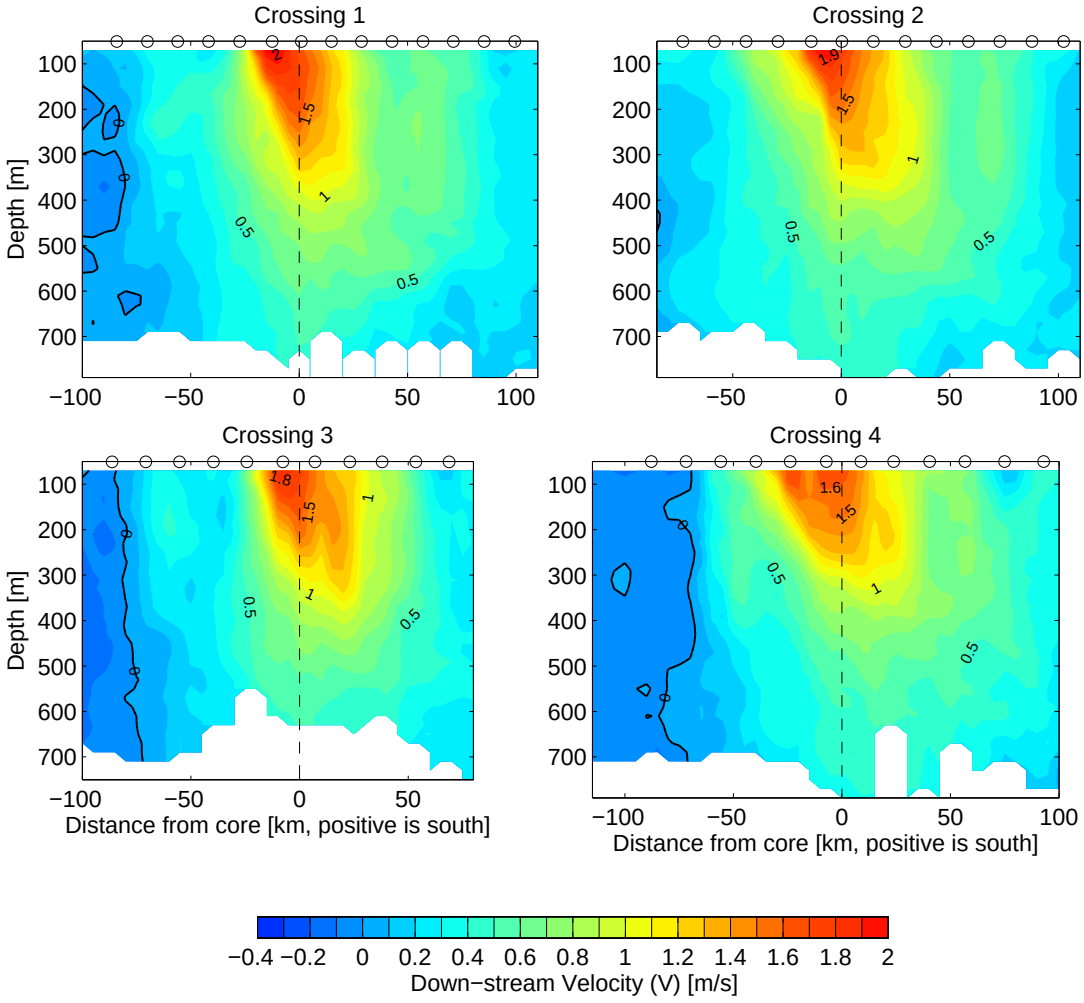

Figure 1.11: Down-stream velocities for individual feature survey Crossings 1-4. All plots have the same aspect ratio. Black circles indicate locations of CTD casts. Dashed black lines indicate location of core. Solid black lines are zero contours. Note the local velocity maxima south of the core in Crossings 1, 2, and 4 corresponding with the reversal of the horizontal temperature gradient in these locations (Figure 1.10).

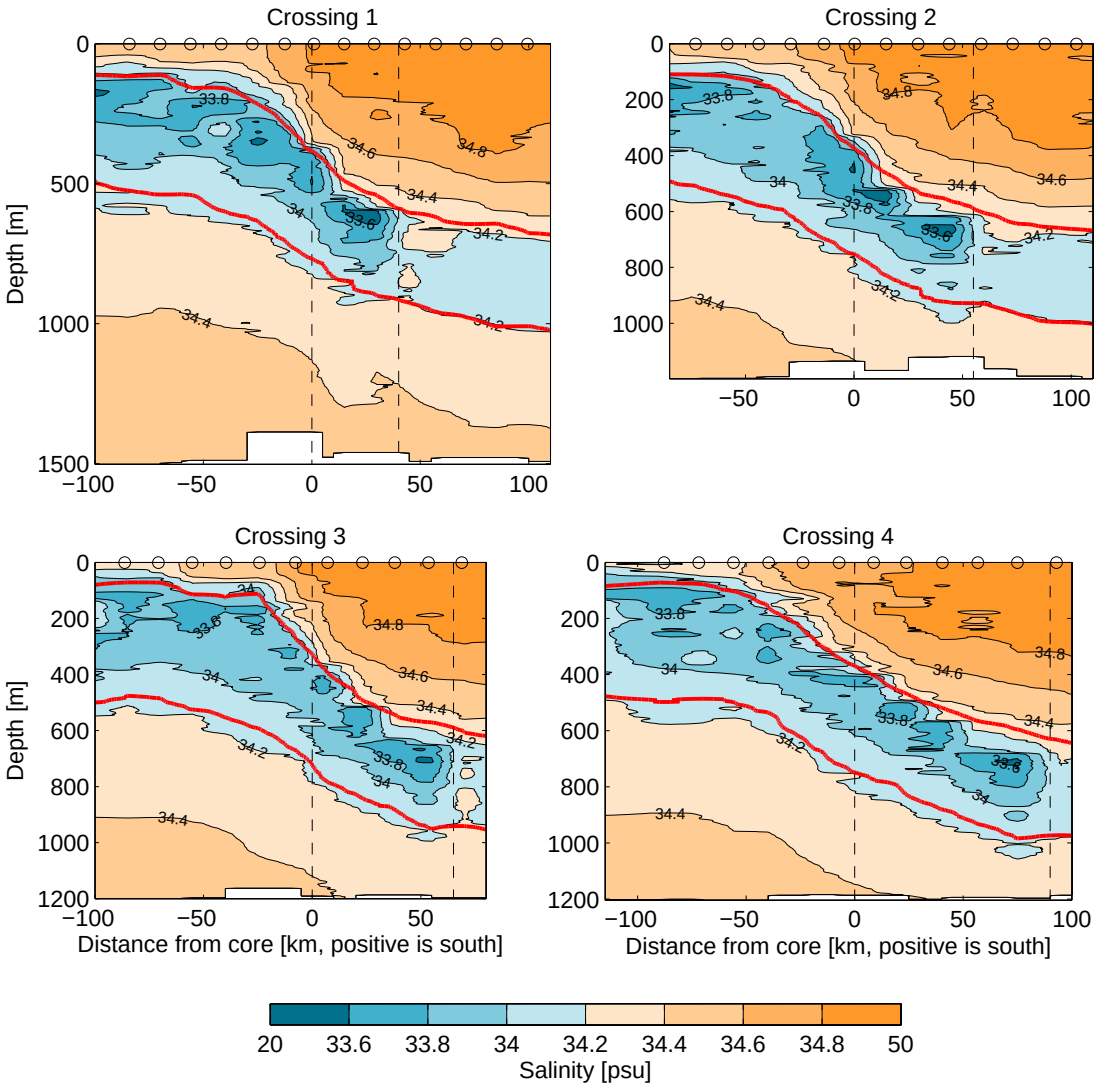

Figure 1.12: Salinity for individual feature survey Crossings 1-4. All plots have the same aspect ratio. Black circles indicate locations of CTD casts. Dashed black lines indicate location of core and extent of low-salinity intrusive layer. Note the progression of the low-salinity intrusion along the pycnocline towards the south side of the core. Red contours indicate the σ_θ =26.4 and 27.1 contours.

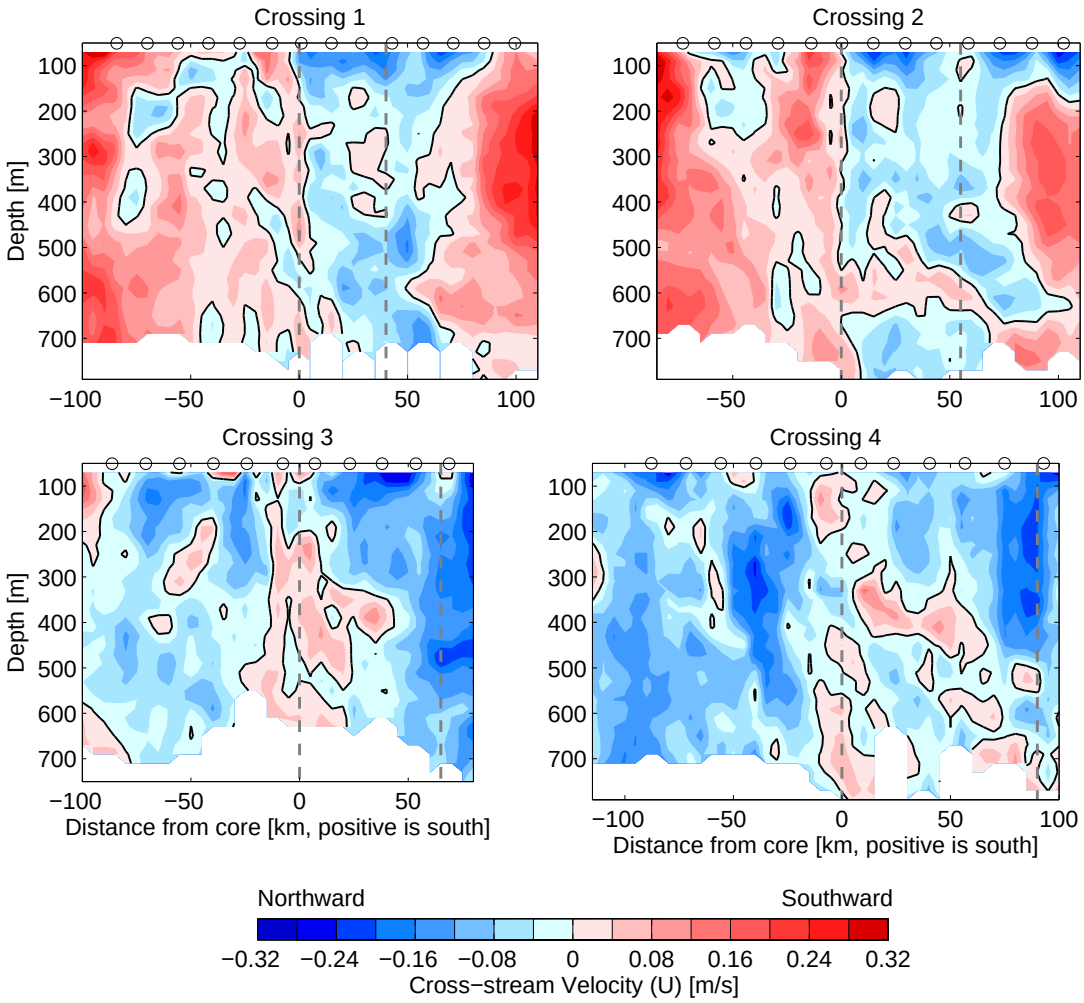

Figure 1.13: Cross-stream velocities for individual feature survey Crossings 1-4. All plots have the same aspect ratio. Black circles indicate locations of CTD casts. Shades of blue (red) indicate northward (southward) cross-stream flow. Heavy black lines are zero cross-stream velocity magnitude. Dashed gray lines indicate location of core and southward extent of low-salinity intrusion. Note the apparent confluence around the core in Crossing 1 and the progression of southward cross-stream velocities towards the anticyclonic side of the core in Crossings 2-4 (pink patches between 300 and 700 m).

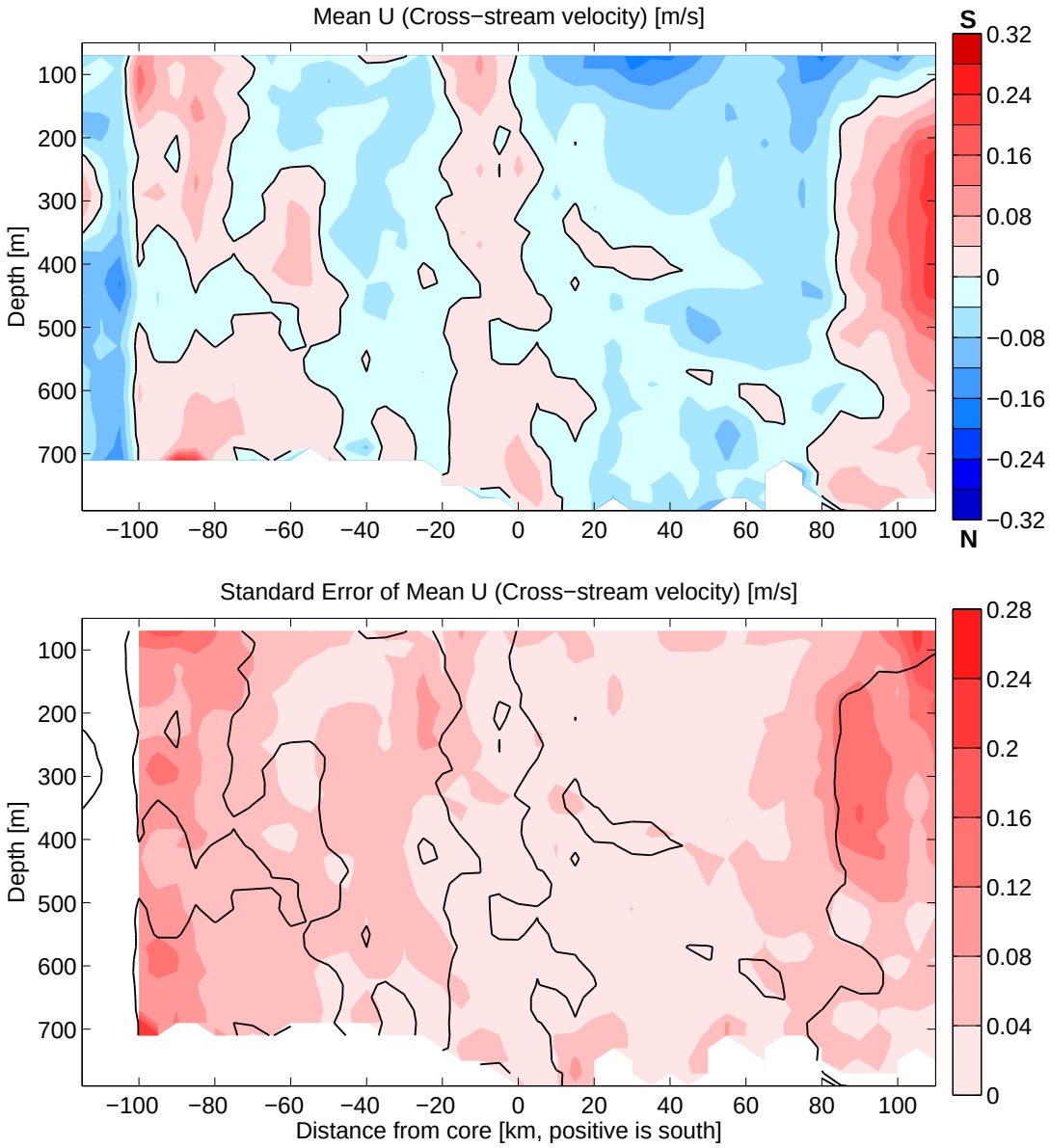

Figure 1.14: (top) Mean cross-stream velocities from feature survey Crossings 1-4. Black contour indicates zero cross-stream velocity. (bottom) Standard error of mean down-stream velocities. Black contours indicate zero mean cross-stream velocity from top panel for context.

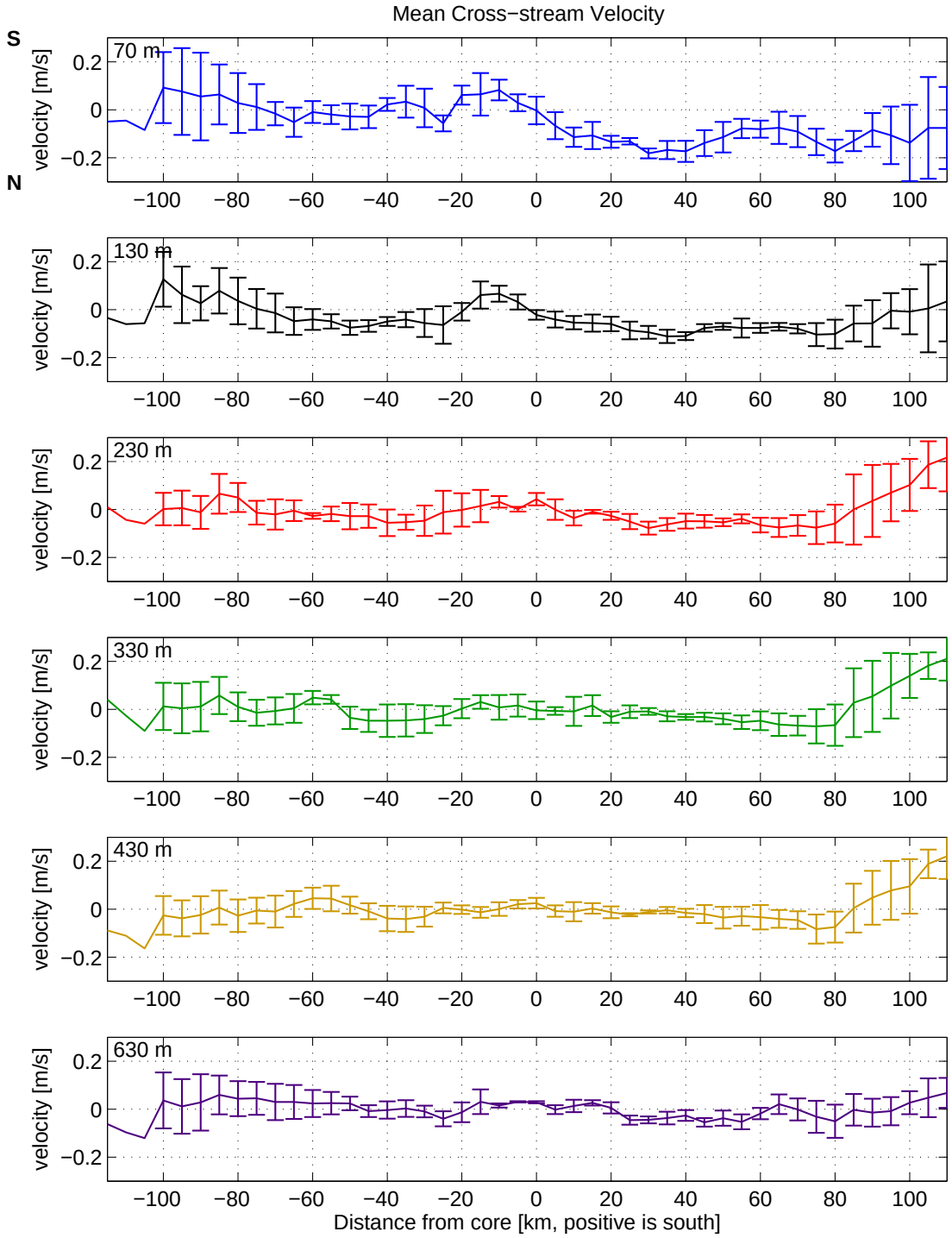

Figure 1.15: Mean cross-stream velocities at depths indicated for feature survey Crossings 1-4. Errorbars indicate generous estimates of standard error (see text). Slight confluence on both sides of the core is apparent near the surface, with deeper mean velocities not statistically different from zero. Note that positive velocity values indicate southward flow.

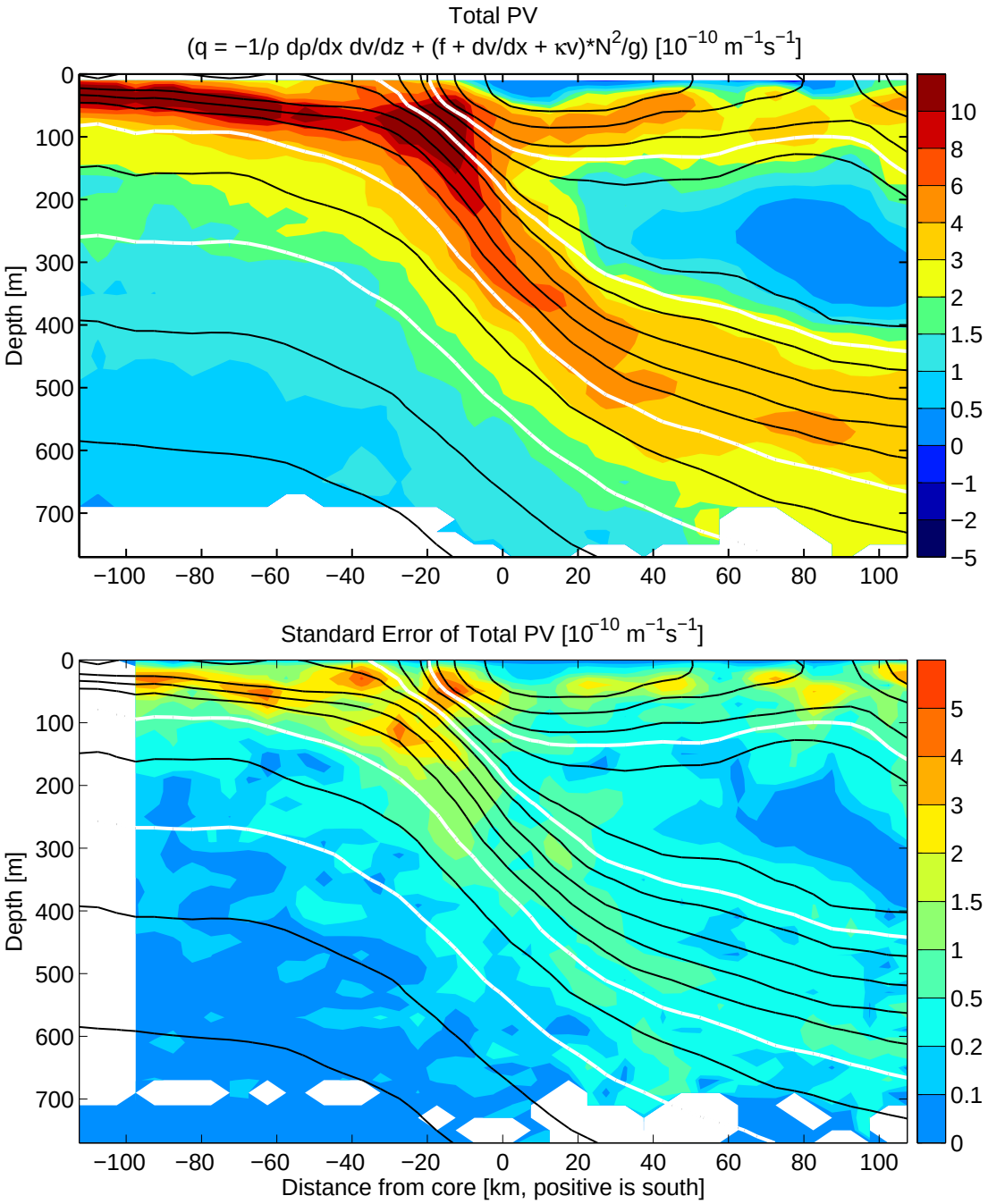

Figure 1.16: Mean total potential vorticity (top) and standard error (bottom) for feature survey Crossings 1-4. Colors indicate $PV * 10^{10}$ and black contour lines are potential density (σ_θ) with contour intervals of 0.2 kg/m^3. White contours are σ_θ = 25.1, 25.5, 26.4, and 26.8, outlining the four major regions mentioned in the text. Note high-PV band running along isopycnals from north to south of core and low-PV mode water between 150 and 400 m south of core.

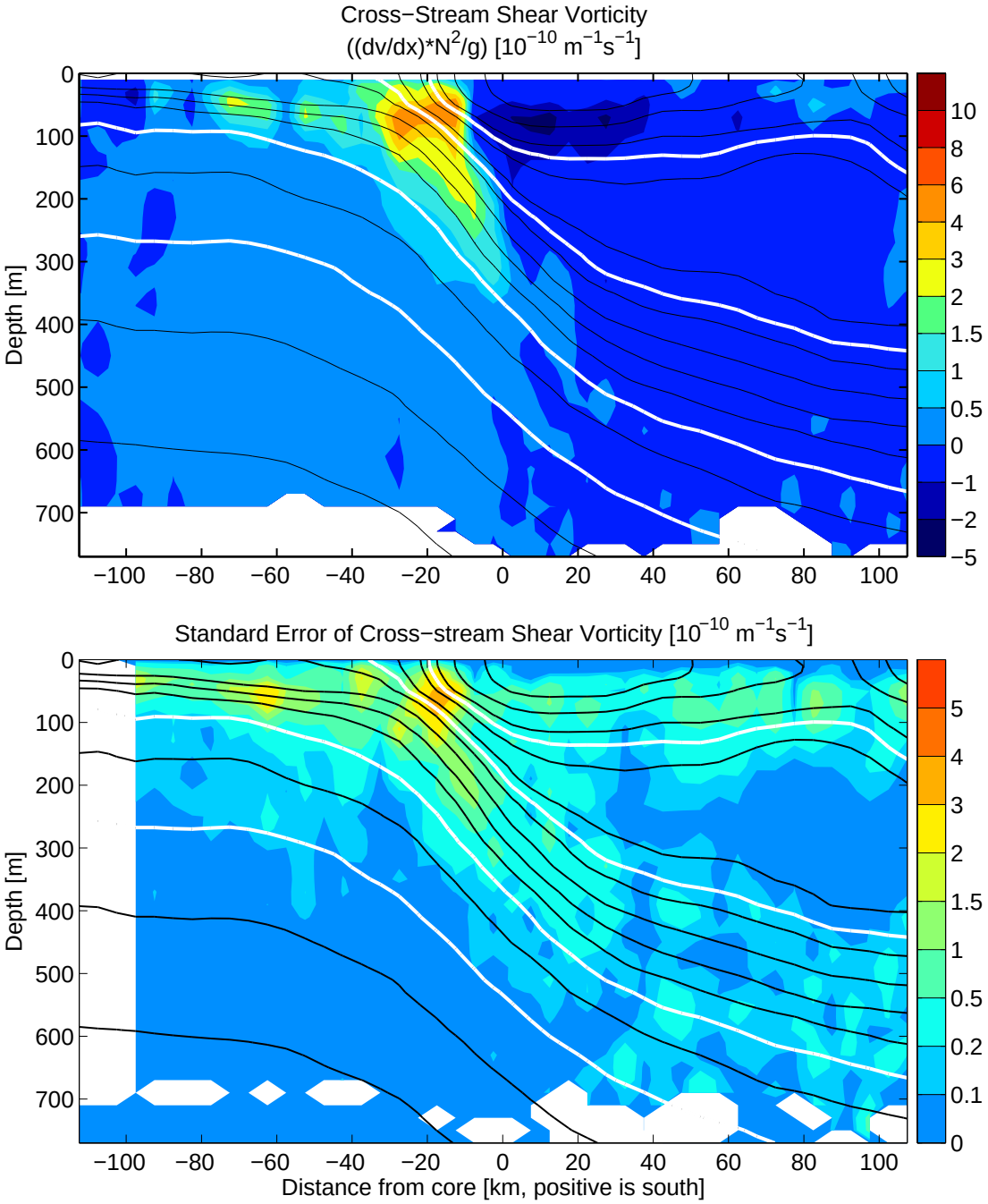

Figure 1.17: Mean cross-stream shear vorticity (top) and standard error (bottom) for feature survey Crossings 1-4. Colors indicate $PV * 10^{10}$ and black contour lines are potential density (σ_θ) with contour intervals of 0.2 kg/m^3. White contours are $\sigma_\theta = 25.1$, 25.5, 26.4, and 26.8, outlining the four major regions mentioned in the text. Note strong contributions from shear component at shallow depths north of the core, descending across the core with isopycnals, as well as fairly strong negative vorticity at shallow depths south of the core.

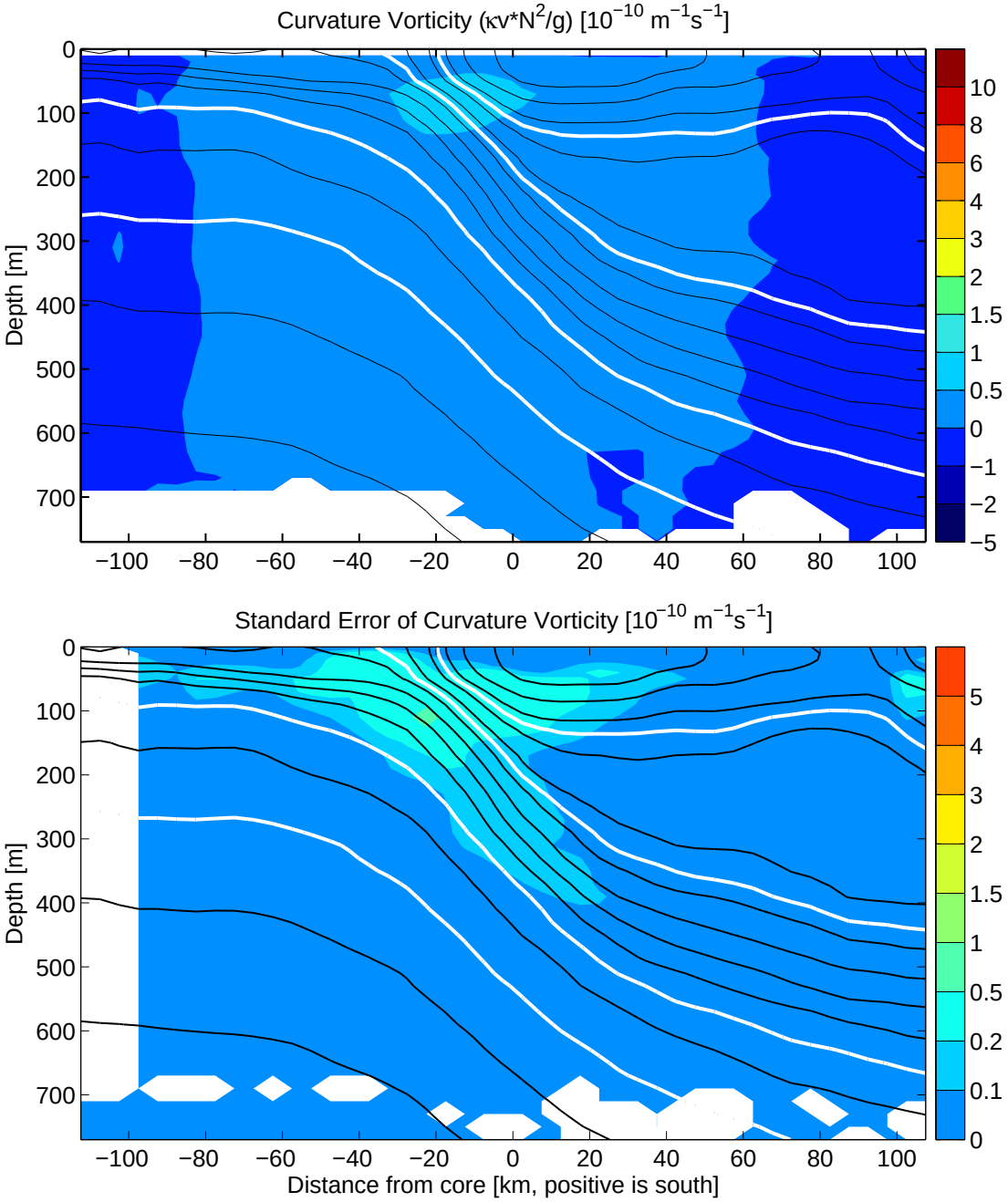

Figure 1.18: Mean curvature vorticity (top) and standard error (bottom) for feature survey Crossings 1-4. Colors indicate $PV * 10^{10}$ and black contour lines are potential density (σ_θ) with contour intervals of 0.2 kg/m^3. White contours are $\sigma_\theta = 25.1$, 25.5, 26.4, and 26.8, outlining the four major regions mentioned in the text. Curvature adds a very small positive vorticity throughout most of the region due to the cyclonic curvature of the trough.

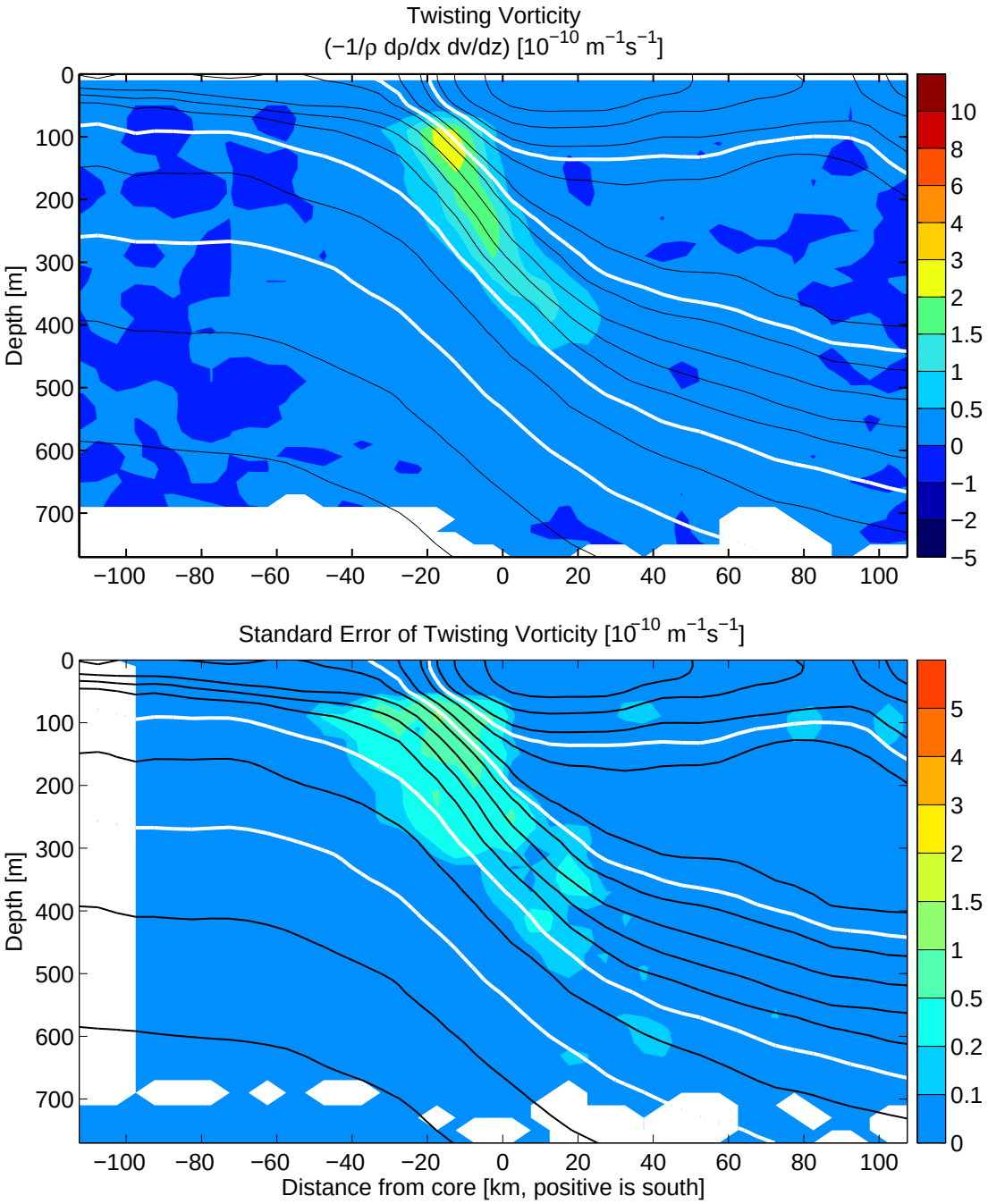

Figure 1.19: Mean twisting vorticity (top) and standard error (bottom) for feature survey Crossings 1-4. Colors indicate $PV * 10^{10}$ and black contour lines are potential density (σ_θ) with contour intervals of 0.2 kg/m^3. White contours are $\sigma_\theta = 25.1$, 25.5, 26.4, and 26.8, outlining the four major regions mentioned in the text. Twisting vorticity makes strong contributions at shallow depths north of the core, descending across the core with isopycnals.

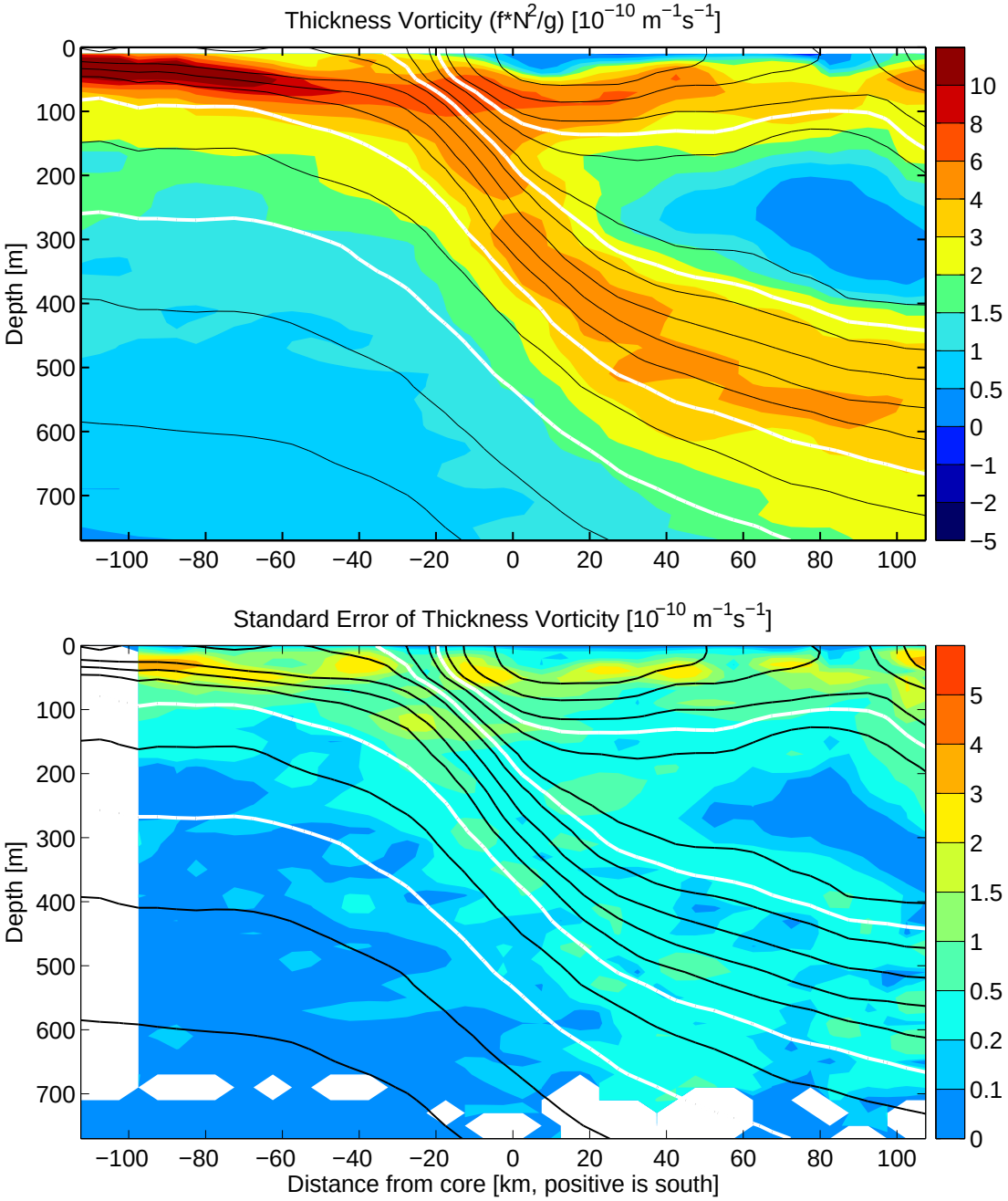

Figure 1.20: Mean thickness vorticity (top) and standard error (bottom) for feature survey Crossings 1-4. Colors indicate $PV * 10^{10}$ and black contour lines are potential density (σ_θ) with contour intervals of 0.2 kg/m^3. White contours are $\sigma_\theta = 25.1$, 25.5, 26.4, and 26.8, outlining the four major regions mentioned in the text. The thickness component defines the background structure of the total PV.

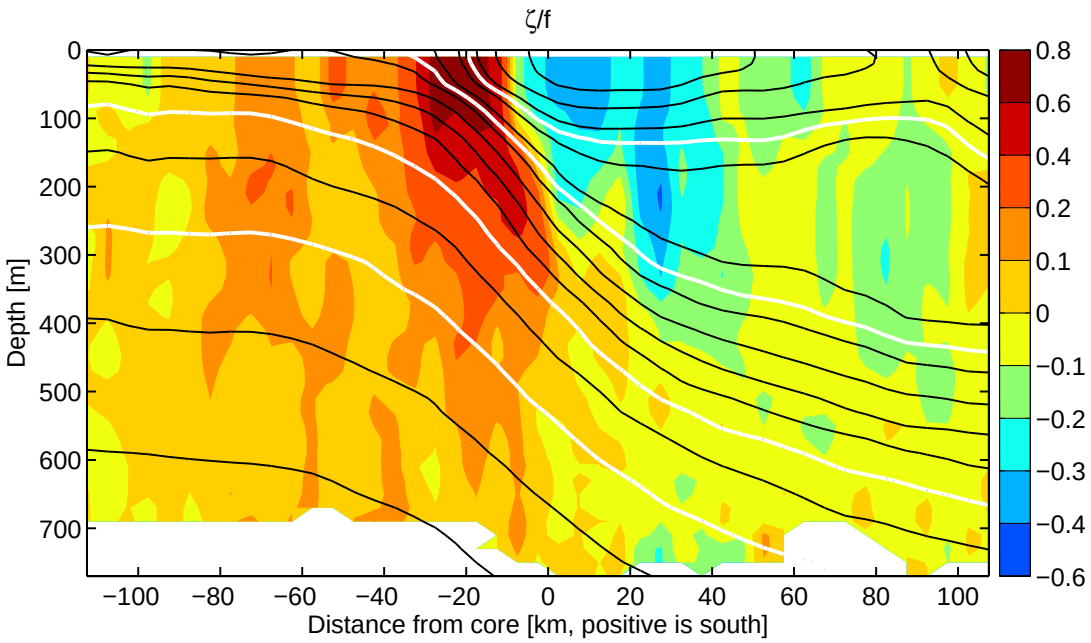

Figure 1.21: Mean Rossby number (ζ/f) for feature survey Crossings 1-4. Colors indicate Rossby number and black contour lines are potential density (σ_θ) with contour intervals of 0.2 kg/m^3. White contours are $\sigma_\theta = 25.1$, 25.5, 26.4, and 26.8, outlining the four major regions mentioned in the text. Rossby numbers reach $>$0.7 at shallow depths north of the core and about -0.4 south of the core.

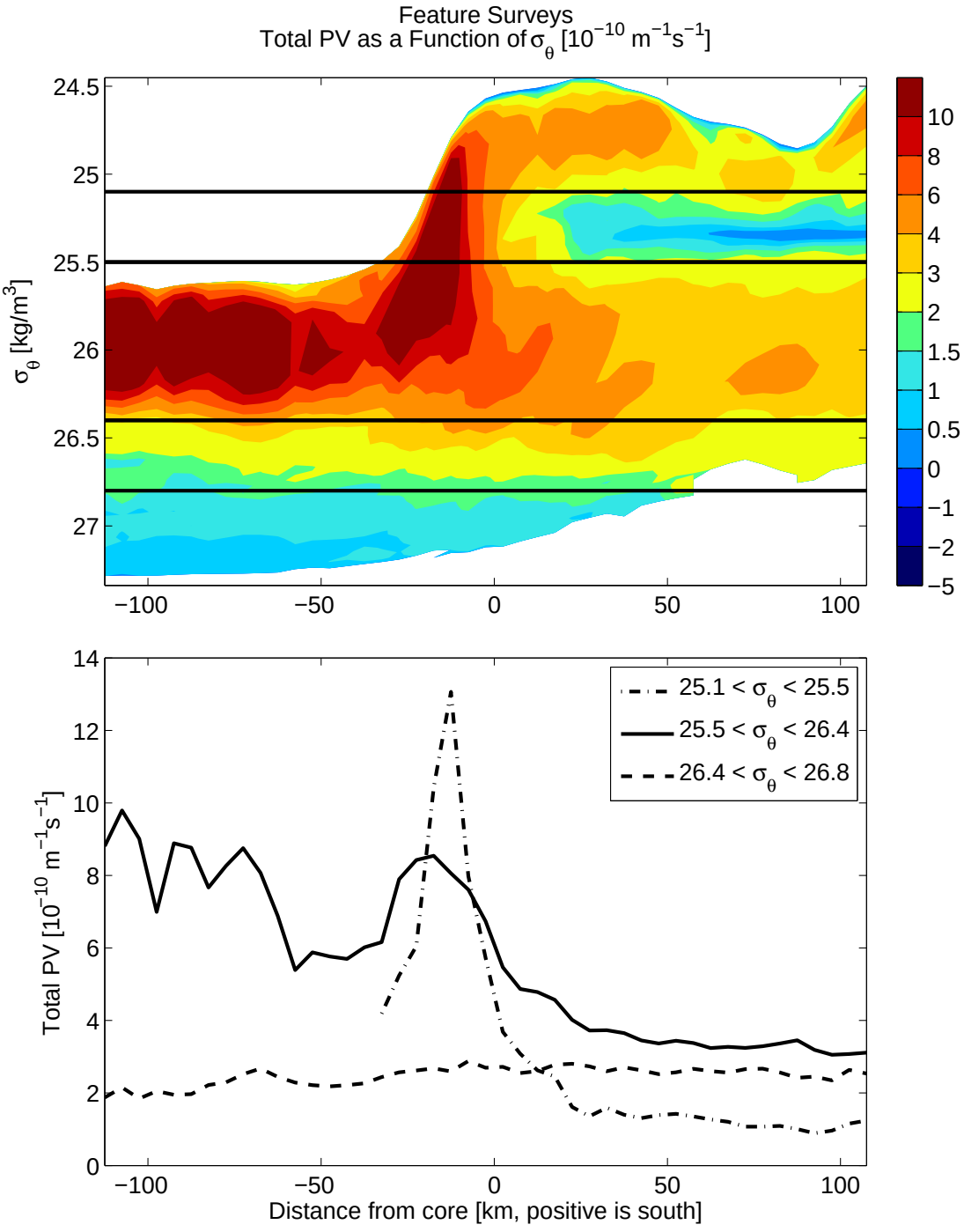

Figure 1.22: (top) Mean total PV as a function of σ_θ from feature survey Crossings 1-4. Black lines indicate σ_θ = 25.1, 25.5, 26.4, and 26.8, and delineate the mode water, mid-thermocline, lower-thermocline/NPIW, and deep PV gradient regimes mentioned in the text. (bottom) Total PV averaged over the first three layers identified in the top panel, as indicated by the key.

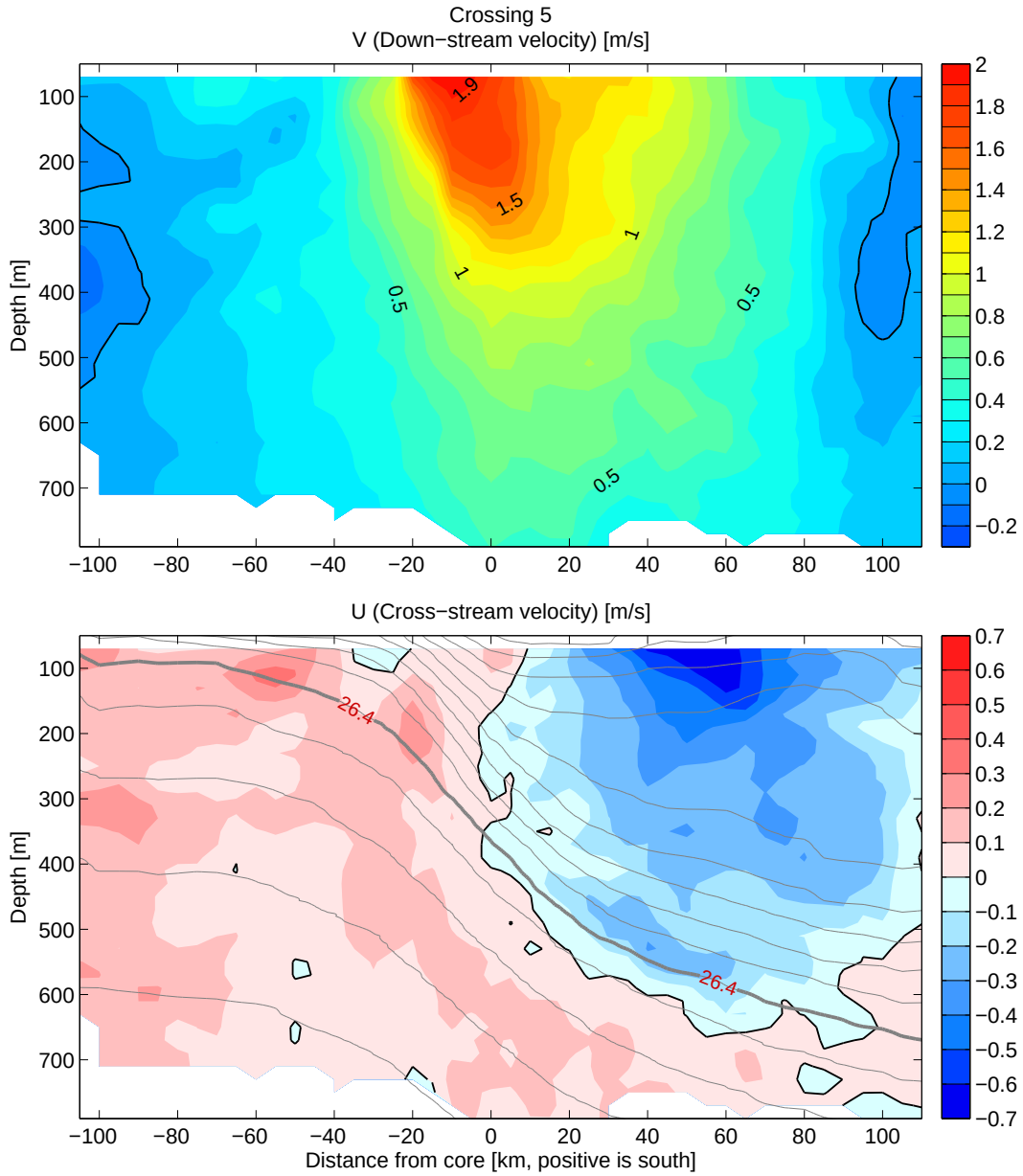

Figure 1.23: Down- (top) and cross-stream (bottom) velocities for feature survey Crossing 5. Black contours indicate zero velocity. Gray contours are mean potential density from Crossings 1-4, with the $\sigma_\theta = 26.4$ contour accentuated to show the depth extent of the strongest PV gradients. Southward flow crossing the core occurs only below this density level, and confluent flow around the core occurs only above it.

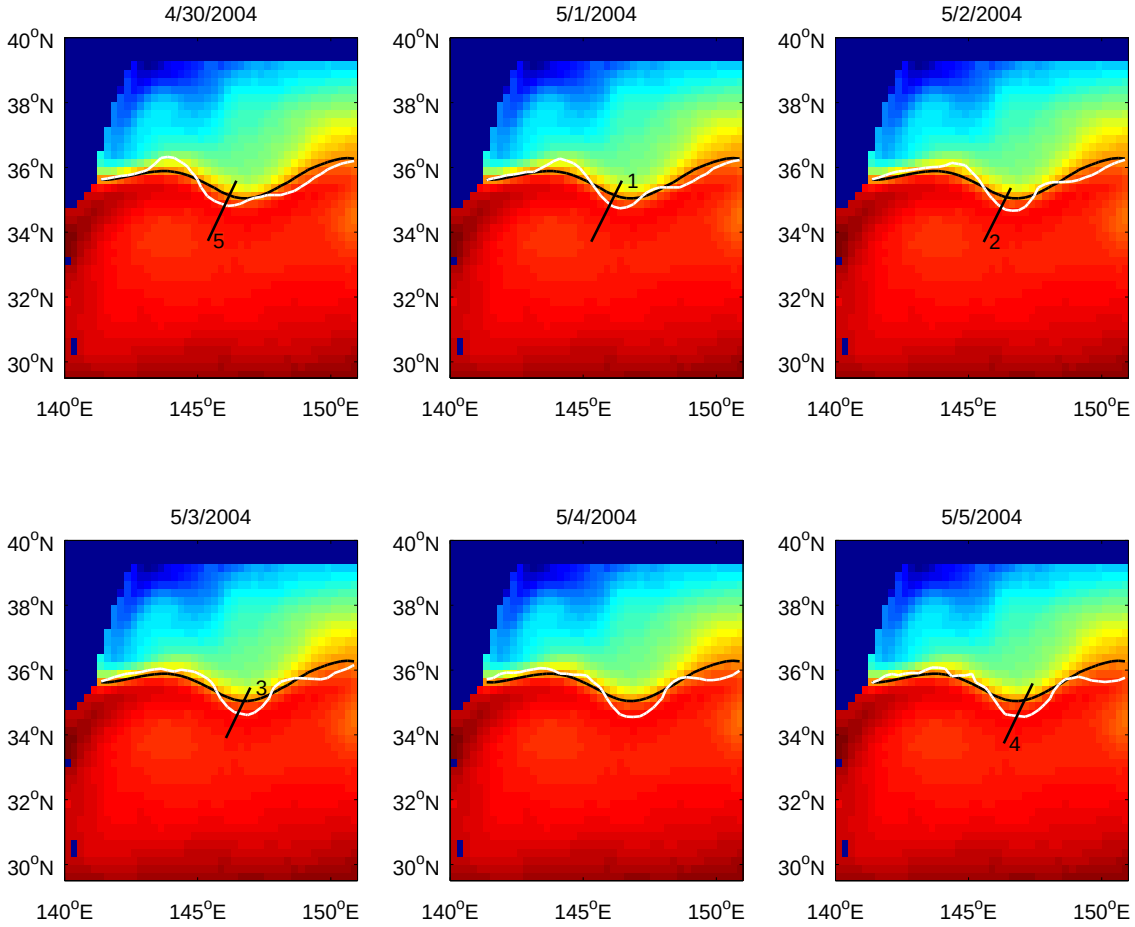

Figure 1.24: Frontal wave passage during feature surveys illustrated via TMI SST data. Background color is mean SST over a 6-month period, with the mean 17.8°C contour shown in black. White contour is the 17.8°C contour for the specified date, with the feature survey crossing plotted and numbered in black. The deviation of the daily 17.8°C contours from the mean suggests a steepening of the meander trough during this time which may represent a mechanism for cross-stream transport.

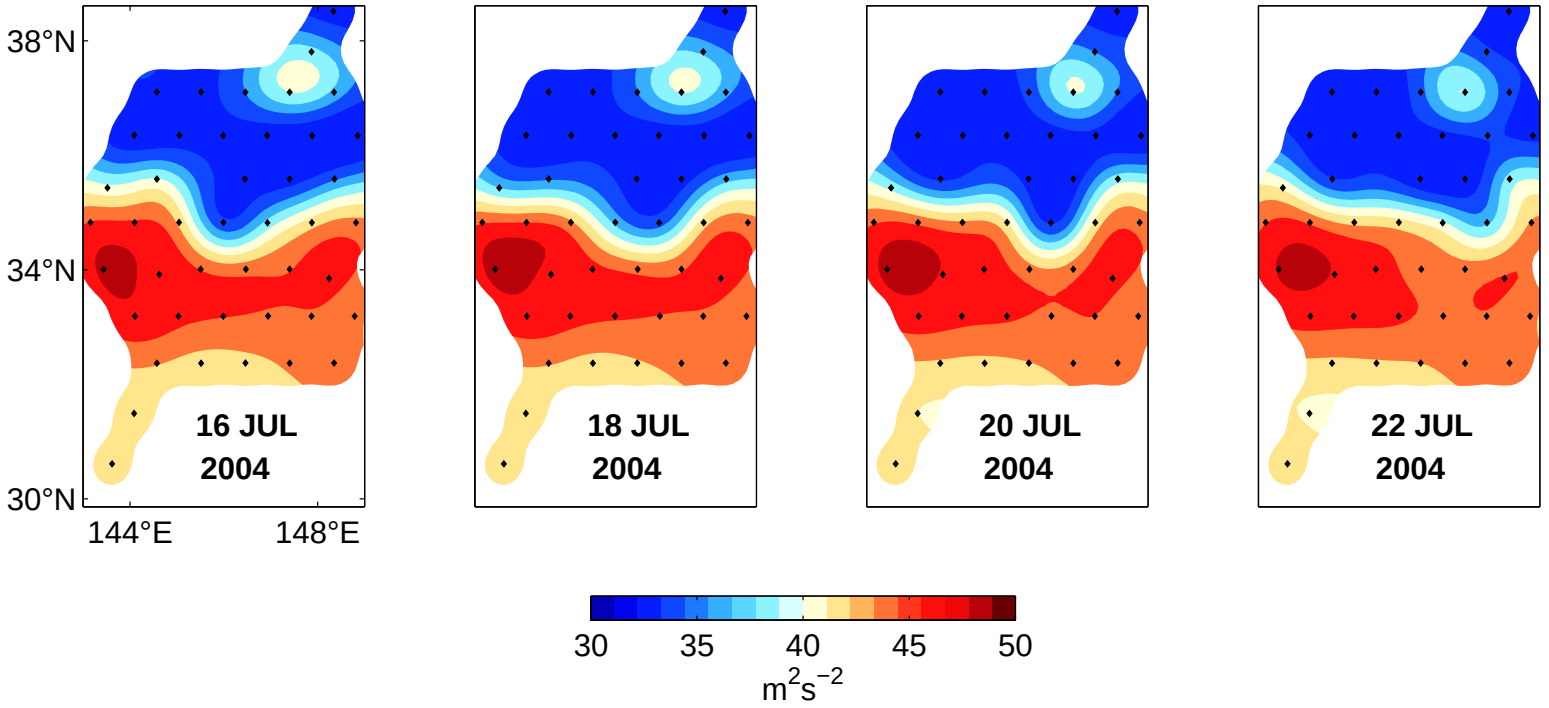

Figure 1.25: Maps of surface geopotential anomaly referenced to 0 at 5300 dbar from CPIES reveal considerable variability in the meander pattern even during the weakly meandering period. This series shows the passage of a frontal wave. Black dots indicate CPIES instrument locations.

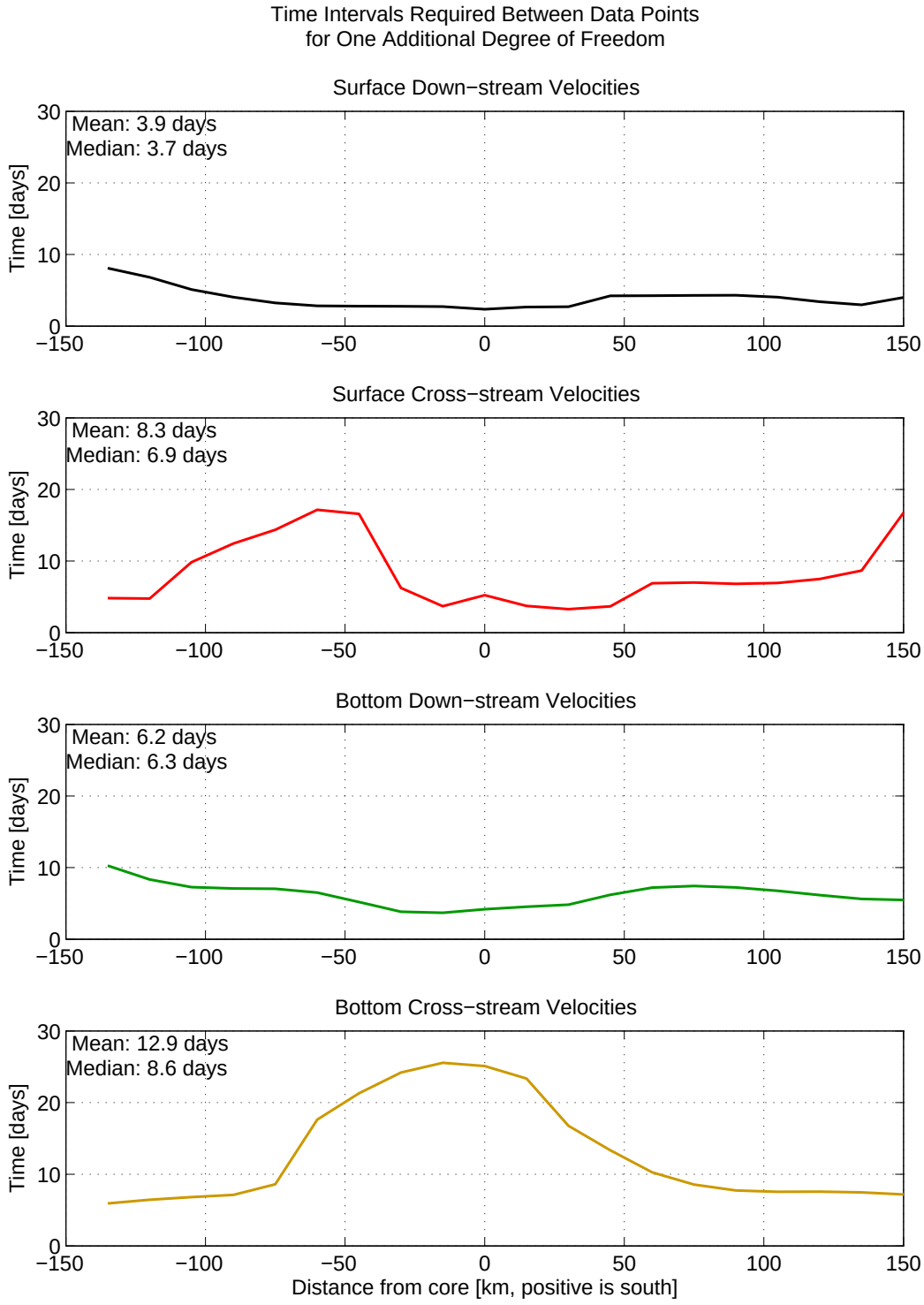

Figure 1.26: Time intervals required between mapped CPIES velocities to obtain one additional degree of freedom. Values shown here are calculated from the time series of the transect entering the meander trough. Although mean values are considerably lower, a conservative time interval of 19 days was chosen to ensure that the significance of bottom cross-stream velocities was not overestimated.

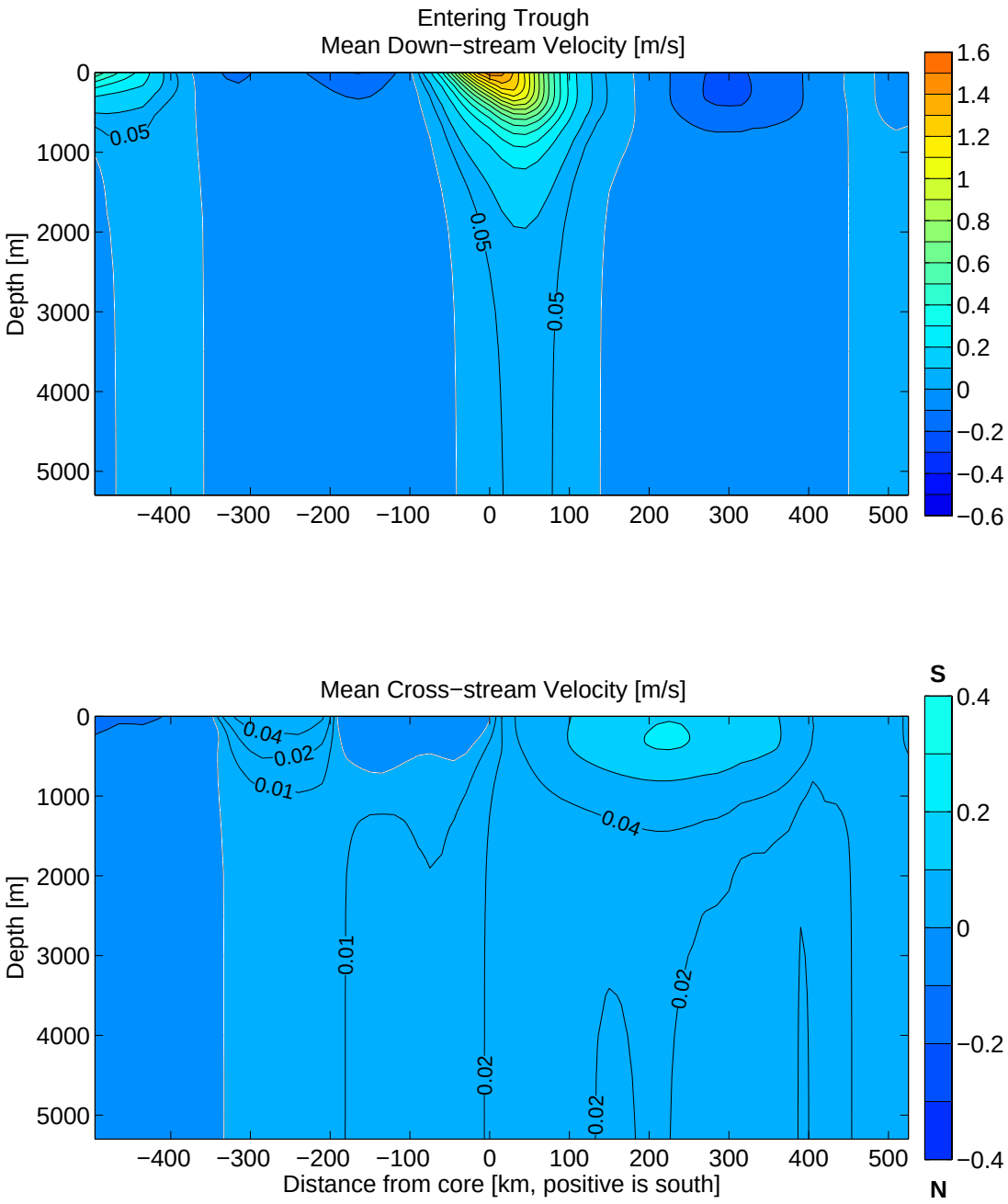

Figure 1.27: Mean down- and cross-stream velocity transects from mapped CPIES entering trough. See text for a comparison between these profiles and those observed in the feature surveys (Figure 1.7). Contour intervals are 0.1 m/s except as labeled. White contours indicate zero velocity.

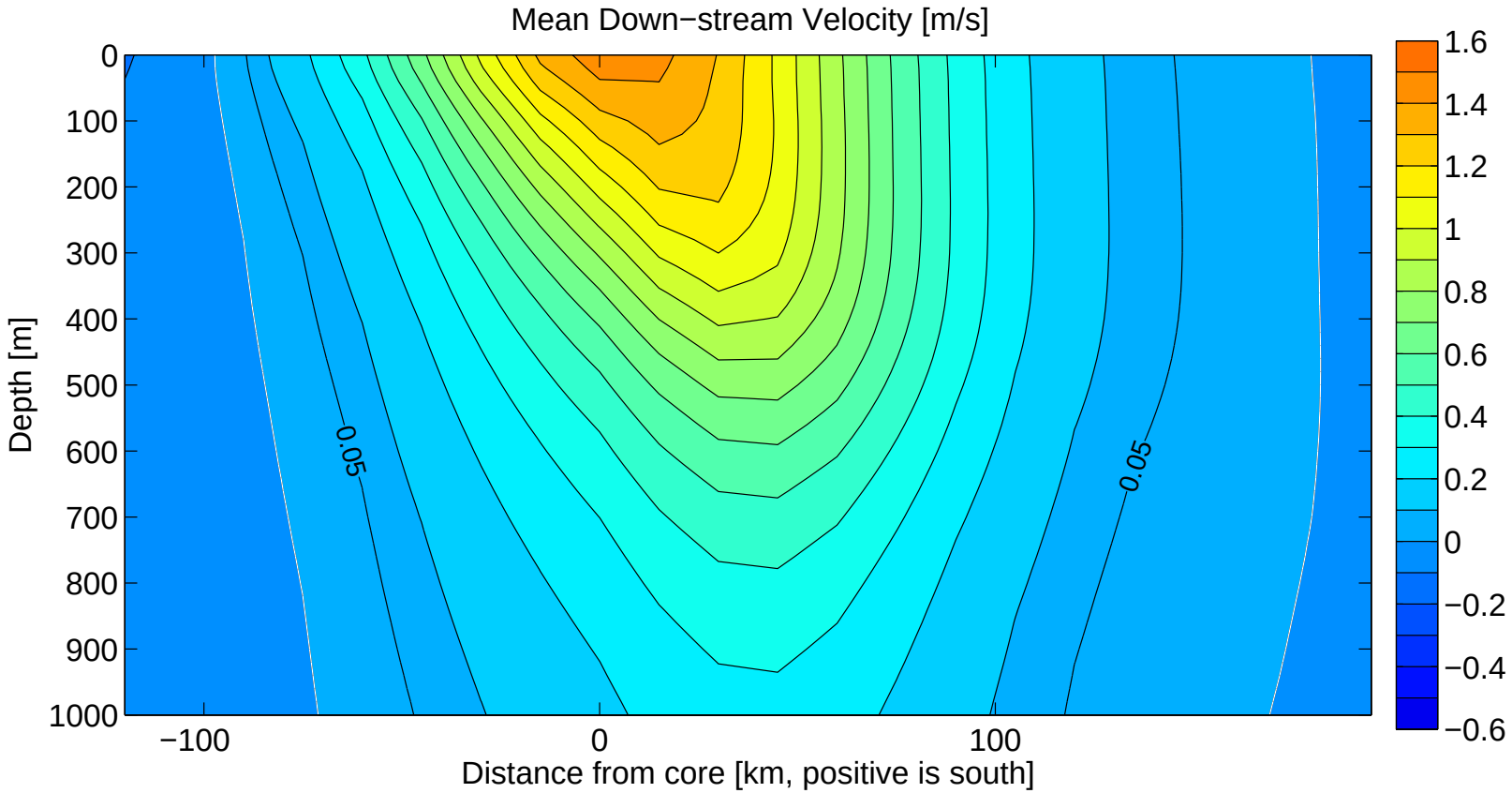

Figure 1.28: Close-up of near-surface core down-stream velocities from mapped CPIES entering trough. Contour intervals are 0.1 m/s except as labeled. White contours indicate zero velocity. Compare to velocities from ADCP transects in Figure 1.7. Both figures have the same aspect ratio.

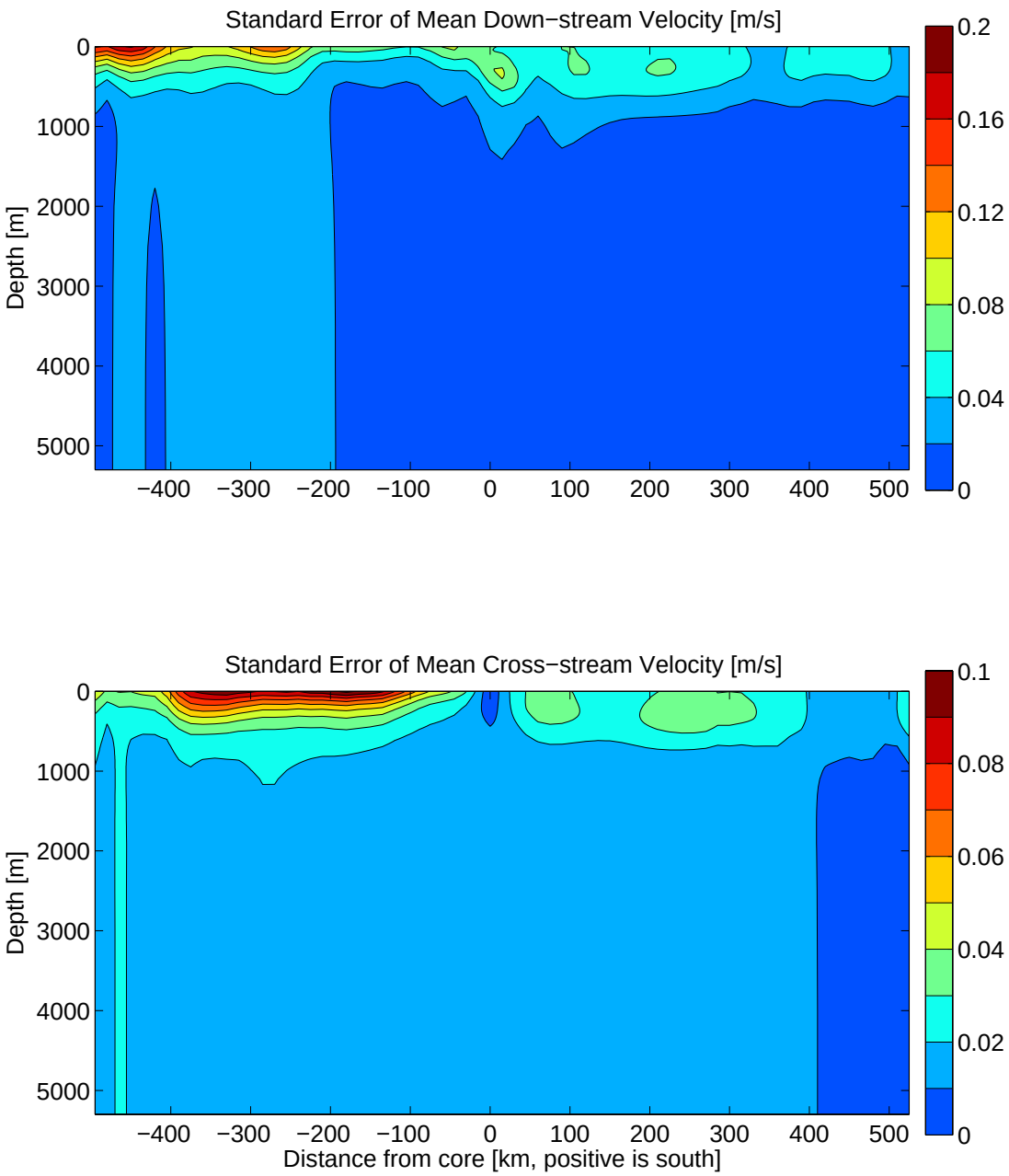

Figure 1.29: Standard error of mean down- and cross-stream velocity transects (Figure 1.27) from mapped CPIES entering trough.

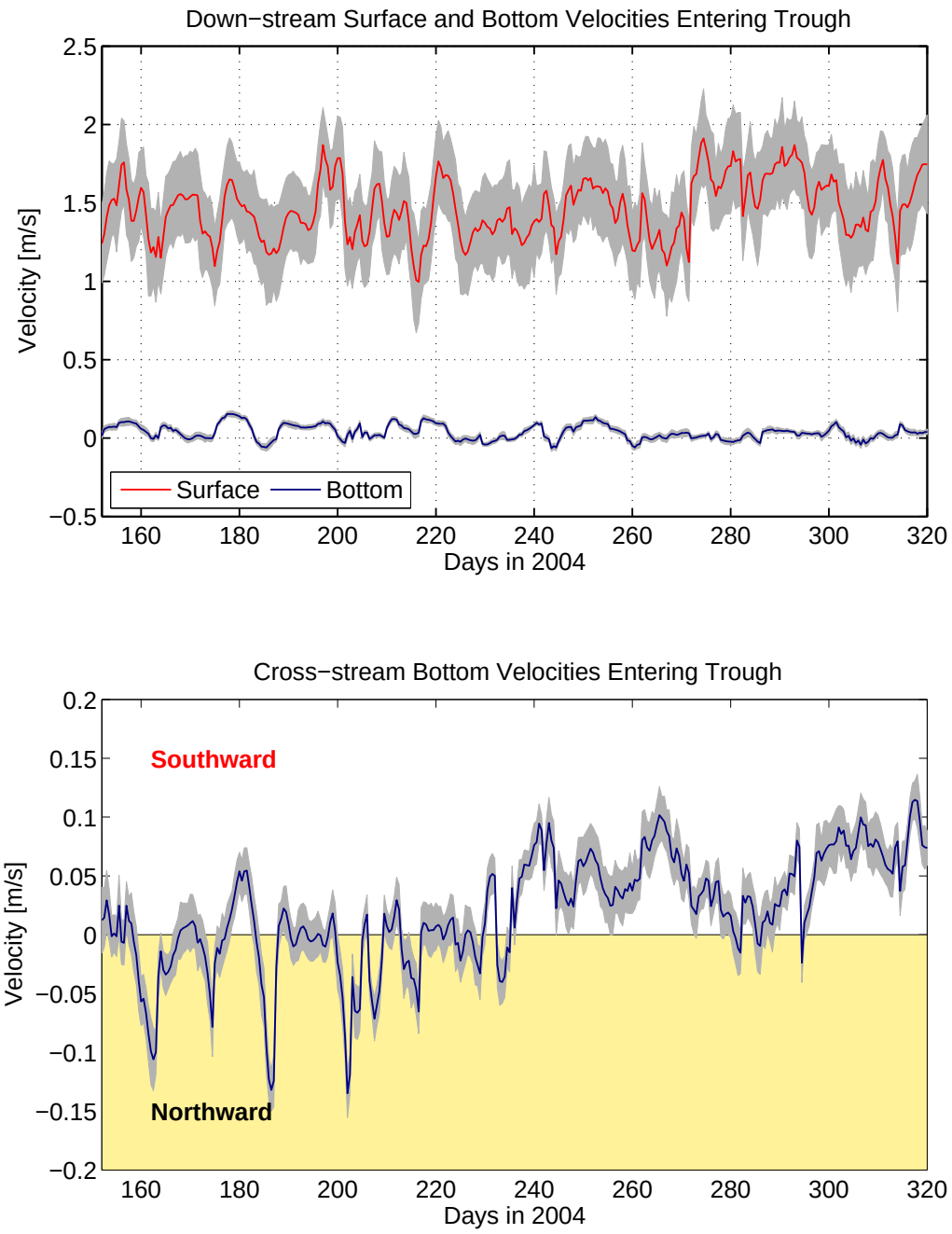

Figure 1.30: Down- and cross-stream surface and bottom velocity time series at core (x=0) from mapped CPIES entering trough. Red indicates surface and blue bottom velocities. Surface cross-stream core velocities are zero by definition and are therefore omitted. Gray shading indicates error in each measurement including errors in u, v values from the CPIES as well as the resultant potential down-stream direction error. Note apparent shift around Day 238 from northward-dominated to southward-dominated cross-stream flows.

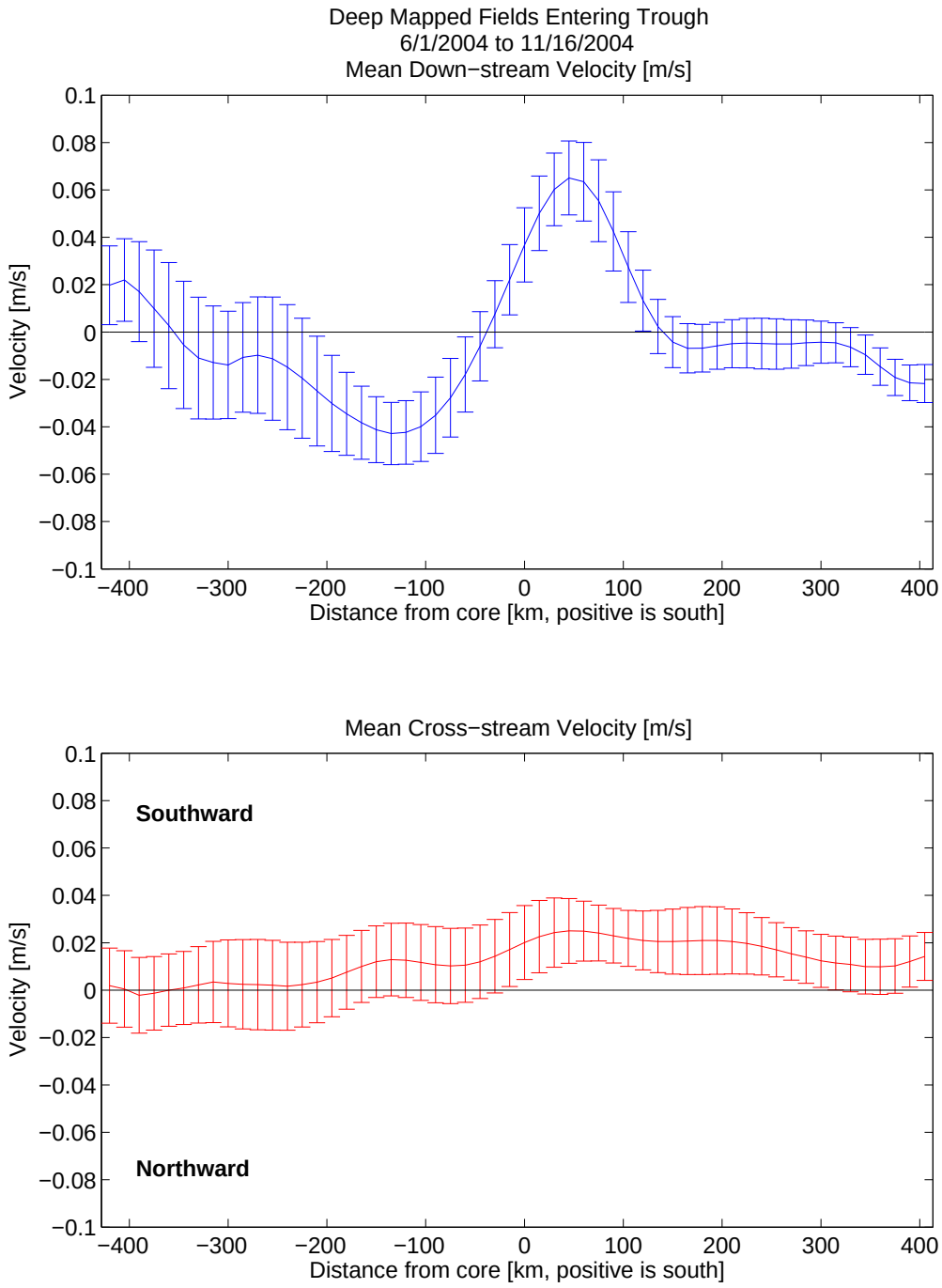

Figure 1.31: Mean down- (top) and cross-stream (bottom) bottom velocities from mapped deep currents entering trough. Errorbars indicate standard error of the mean calculated with the required time interval of 19 days for one additional degree of freedom. Time series with fewer than five degrees of freedom or more than 200 bad data points are not shown.

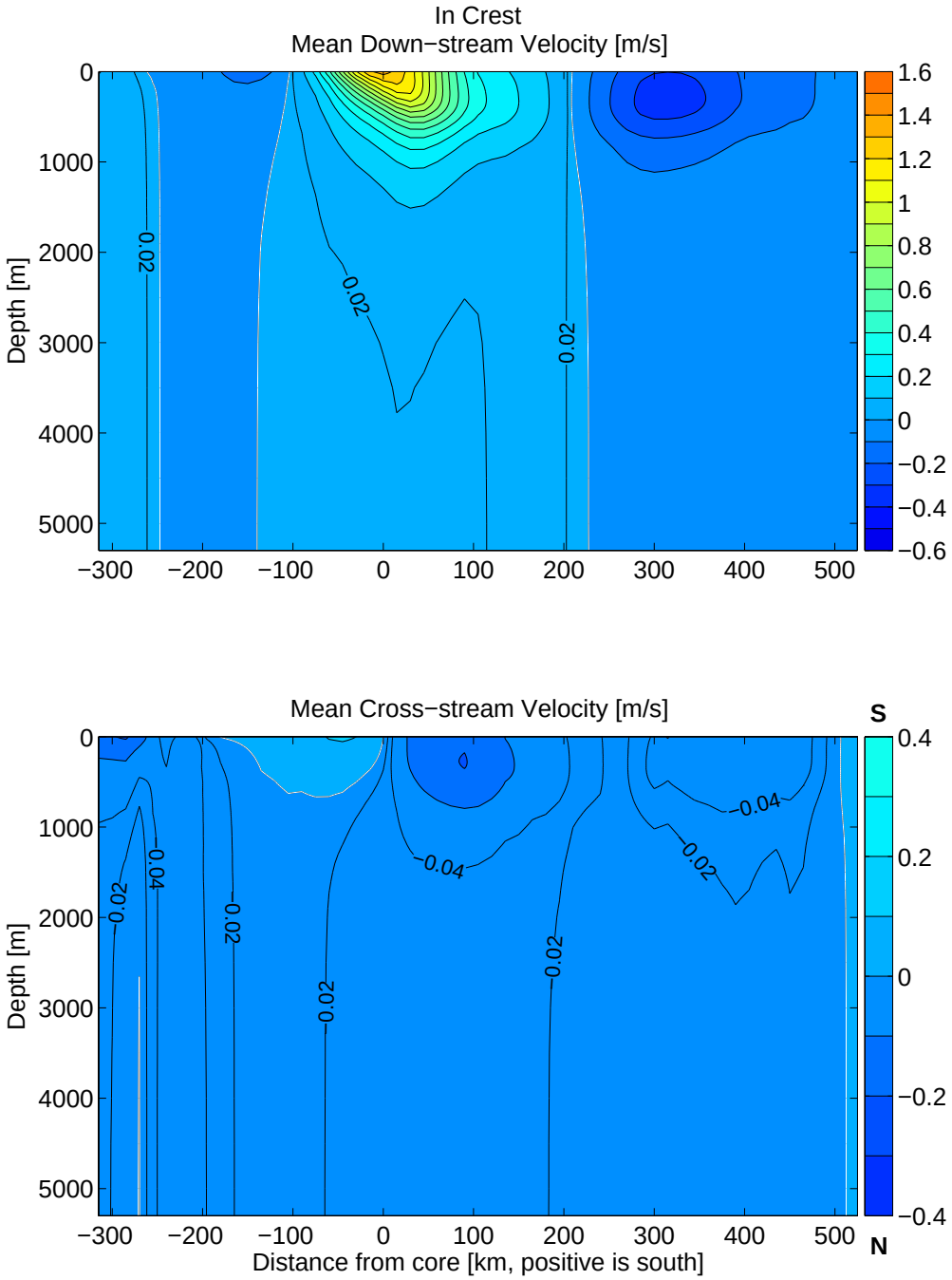

Figure 1.32: Mean down- (top) and cross-stream (bottom) velocity transects from mapped CPIES in crest (143.75°E). Contour intervals are 0.1 m/s except as labeled. White contours indicate zero velocity. See text for comparison of these transects with those observed entering the trough. Note that although axes differ between these plots and Figure 1.27, the aspect ratios are the same.

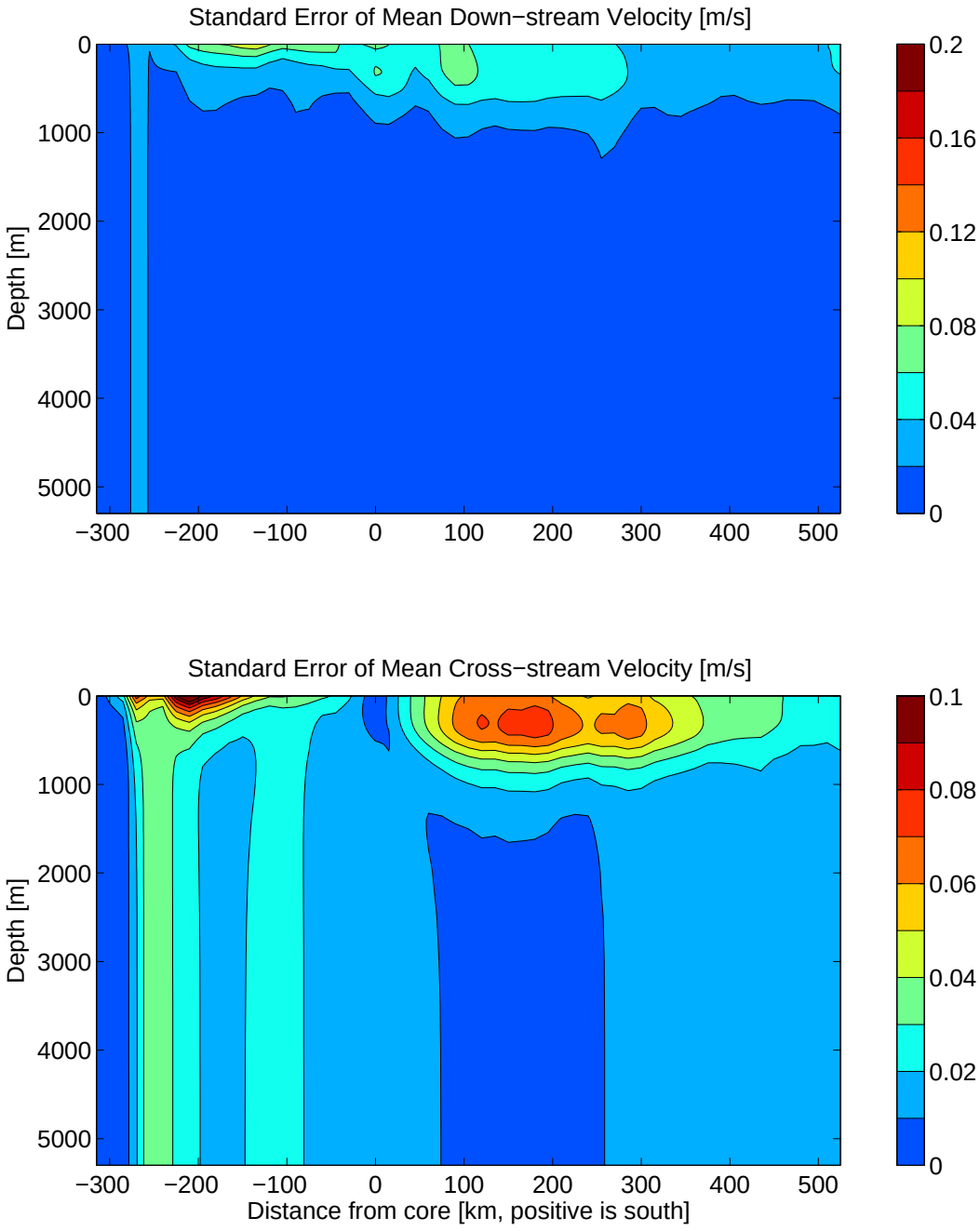

Figure 1.33: Standard error of mean down- (top) and cross-stream (bottom) velocity transects from mapped CPIES in crest (143.75°E).

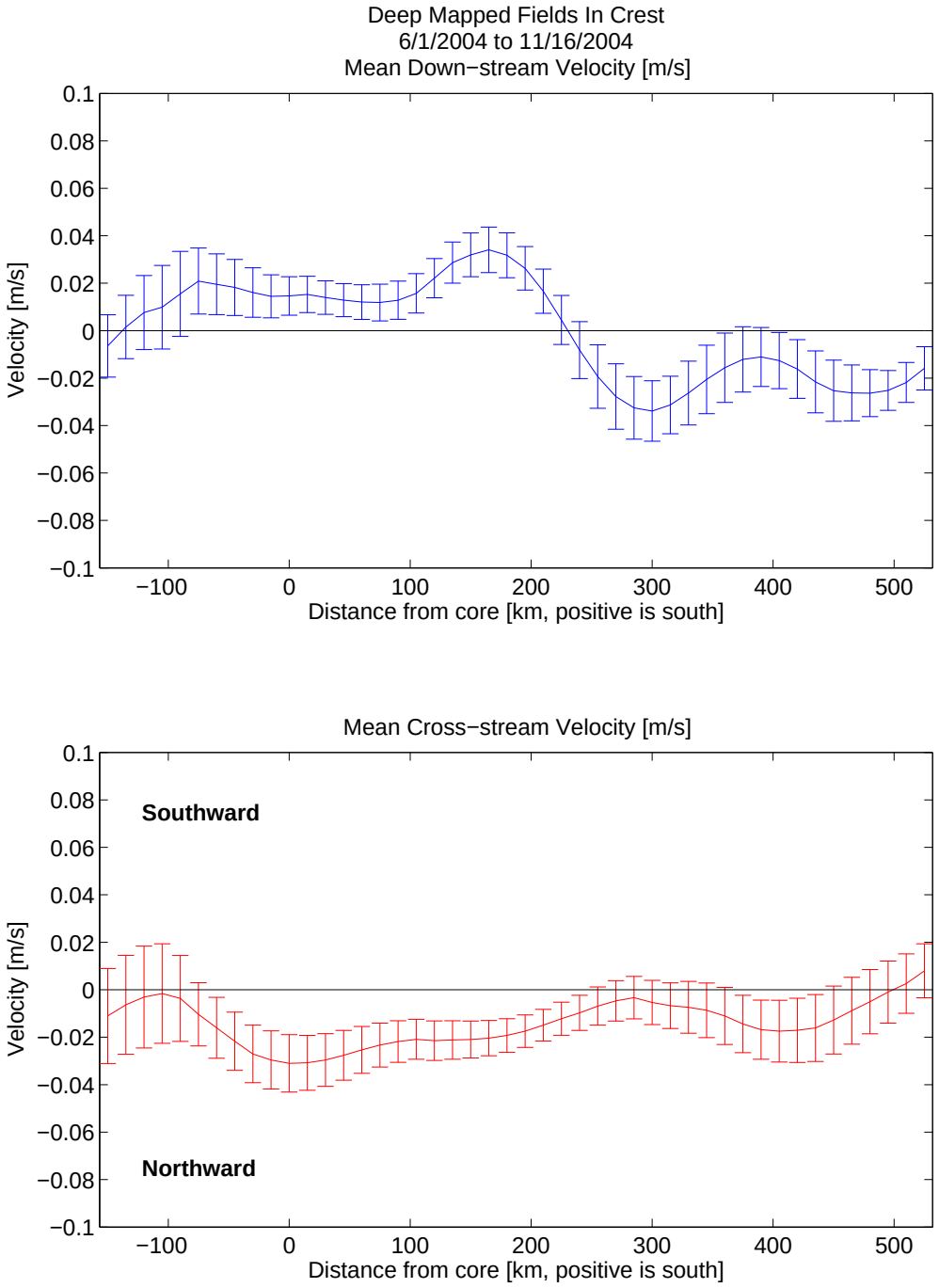

Figure 1.34: Mean down- (top) and cross-stream (bottom) bottom velocities from mapped deep currents in crest (143.75°E). Errorbars indicate standard error of the mean calculated with the required time interval of 19 days for one additional degree of freedom. Time series with fewer than five degrees of freedom or more than 200 bad data points are not shown.

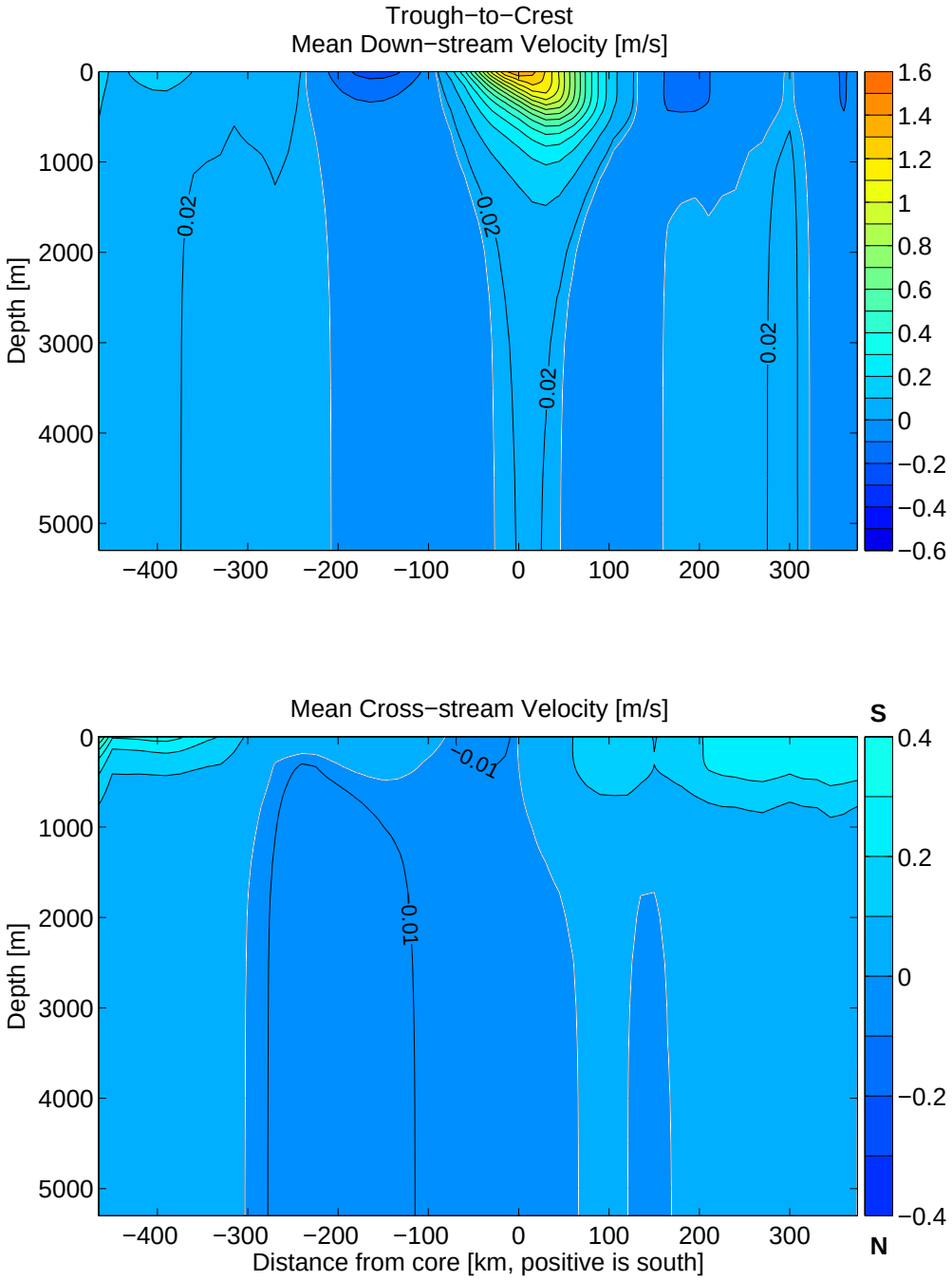

Figure 1.35: Mean down- (top) and cross-stream (bottom) velocity transects from mapped CPIES between trough and second crest (148.5°E). Contour intervals are 0.1 m/s except as labeled. White contours indicate zero velocity. See text for comparison of these transects with those observed entering the trough and in the crest at 143.75°E. Again, the aspect ratio here matches that of Figures 1.27 and 1.32.

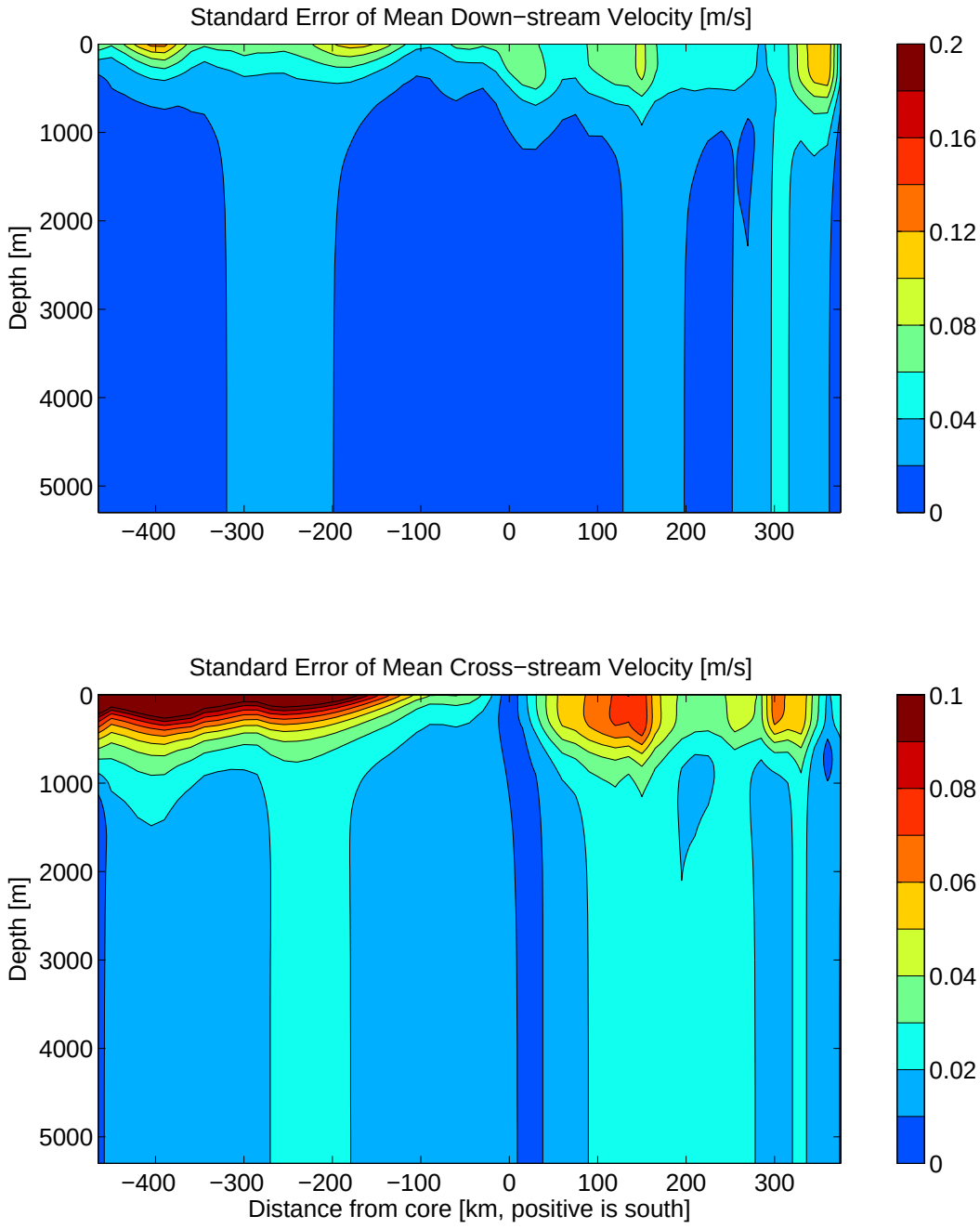

Figure 1.36: Standard error of mean down- and cross-stream velocity transects from mapped CPIES between trough and second crest (148.5°E).

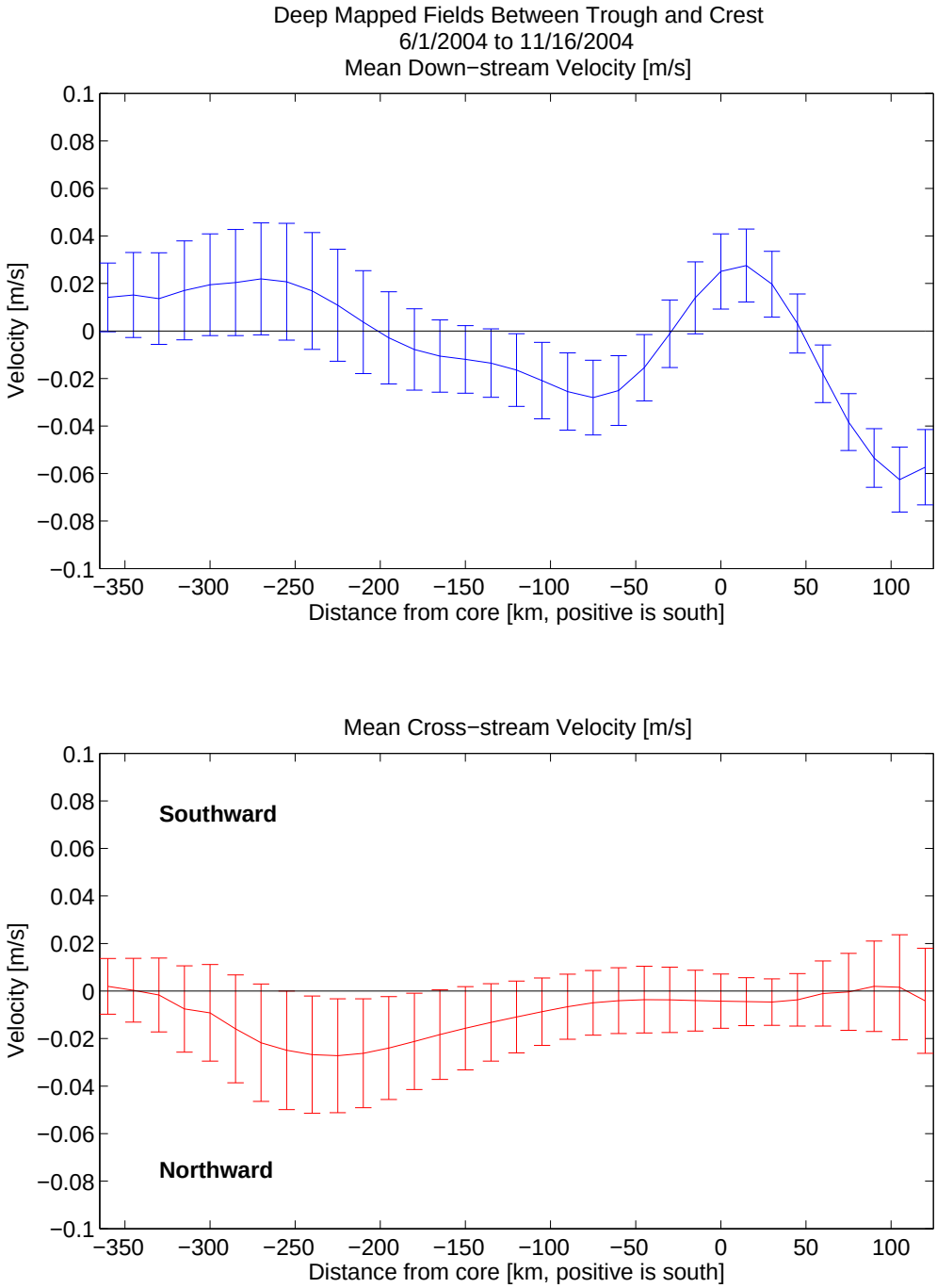

Figure 1.37: Mean down- (top) and cross-stream (bottom) bottom velocities from mapped deep currents between trough and second crest (148.5°E). Errorbars indicate standard error of the mean calculated with the required time interval of 19 days for one additional degree of freedom. Time series with fewer than five degrees of freedom or more than 200 bad data points are not shown. Cross-stream bottom velocities are statistically not different from zero at and surrounding the core.

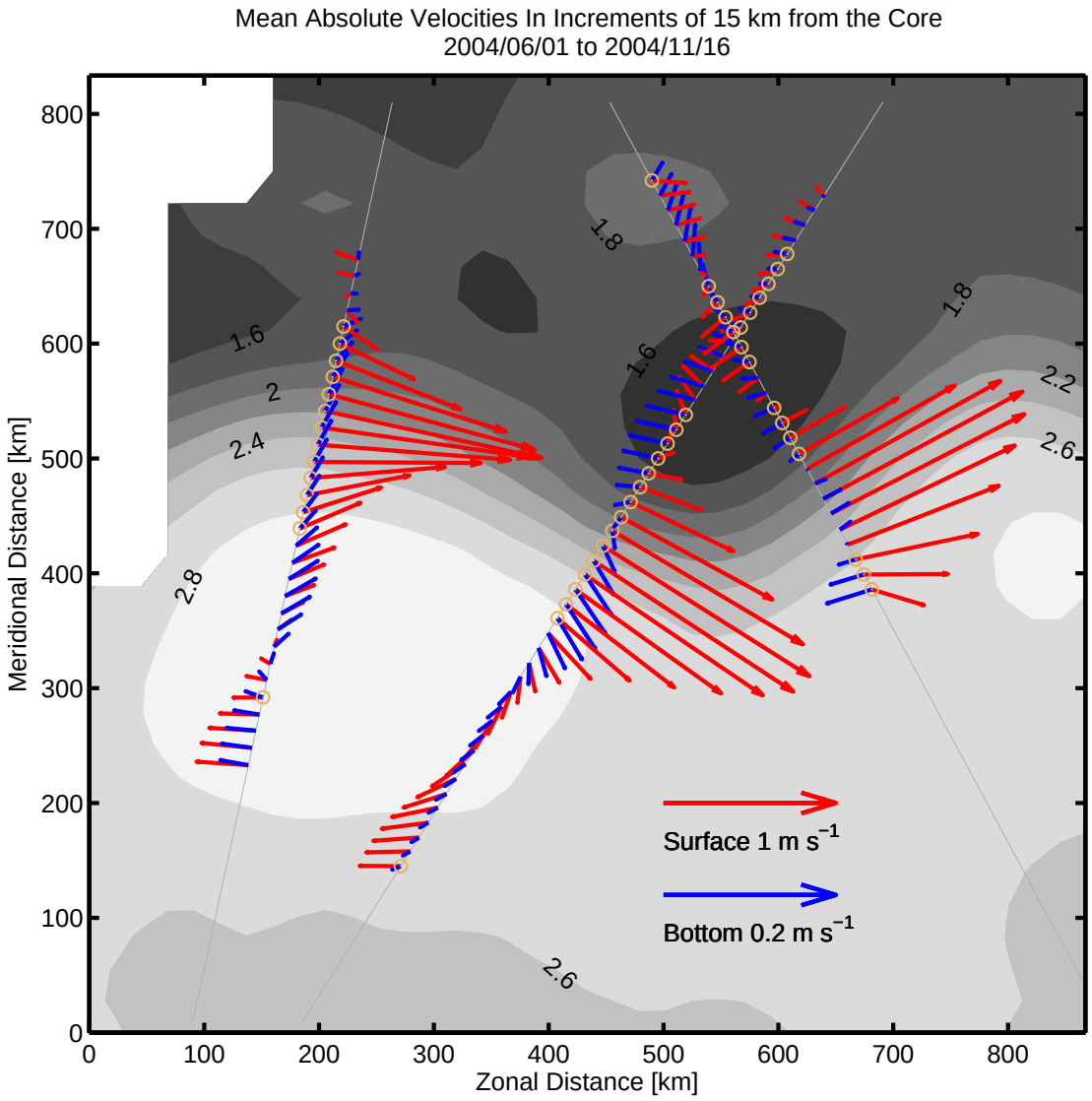

Figure 1.38: Plan view of surface and bottom velocities on three cross-stream transects in the first meander crest, trough, and between the first trough and second crest, over mean SSH contours from AVISO Rio05 for weakly meandering period. Cross-stream lines (thin gray) represent mean cross-stream direction calculated as the perpendicular to the direction of the mean velocity at the core. Orange circles indicate locations where the turning with depth is significant beyond the bounds of the maximum potential directional error in the measurements. Note counterclockwise rotation of bottom (blue) vectors from surface (red) at up-stream (crest) section, clockwise rotation at middle (trough) section, and near vertical alignment at easternmost section; also note evidence of southern and northern recirculation gyres. The longitudinal range of this plot is 141.5-151°E; latitudinal range is 31-38.5°N. SSH contours are in 0.2 m intervals.

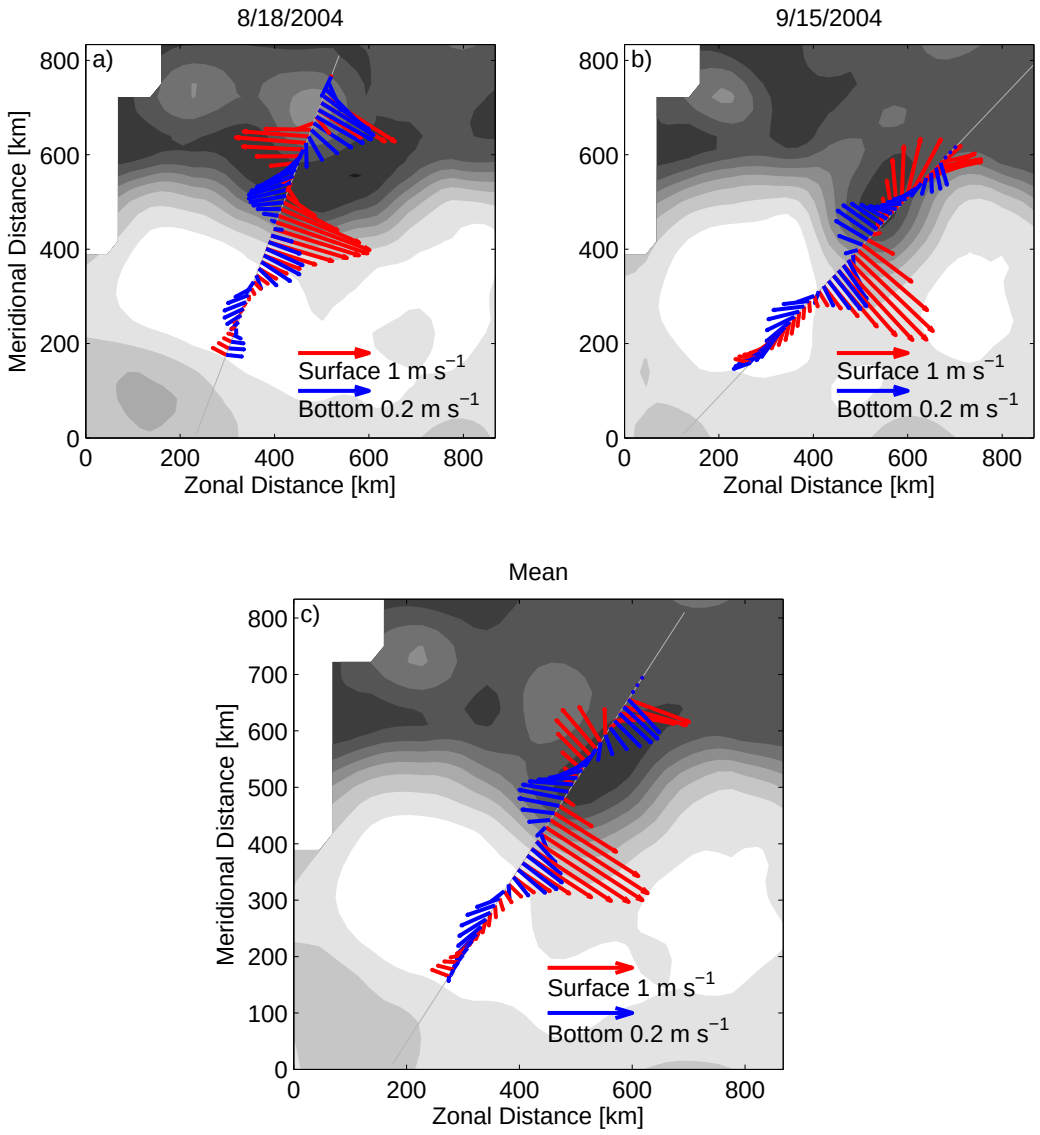

Figure 1.39: Demonstration of plan view schematic averaging procedure entering the trough. Panels *a* and *b* show cross-stream transects superimposed on SSH from two non-consecutive days (to illustrate time-variability). In each of these cases, the longitude of the up-stream edge of the trough has been determined via visual inspection. The location of the core has been determined by finding the maximum absolute surface velocity along this line of longitude. The cross-stream direction has been defined as perpendicular to the surface velocity at the core, and absolute surface (red) and bottom (blue) velocities have been interpolated from the mapped CPIES grid to the cross-stream line. Panel *c* shows the mean of the data shown in panels *a* and *b*. Absolute surface and bottom velocities from the two days are averaged as a function of cross-stream distance. The mean core location is defined as the mean of the lat/lon coordinates of the core on the two individual days, and the cross-stream direction is perpendicular to the mean surface velocity at the core. The average surface and bottom velocities are then plotted along this mean cross-stream line. This identical procedure is used in the crest and trough-to-crest sections, except that those transects use a fixed longitude (variable latitude) rather than tracking the location of the meander phase, since the longitudes of those features remain relatively fixed.

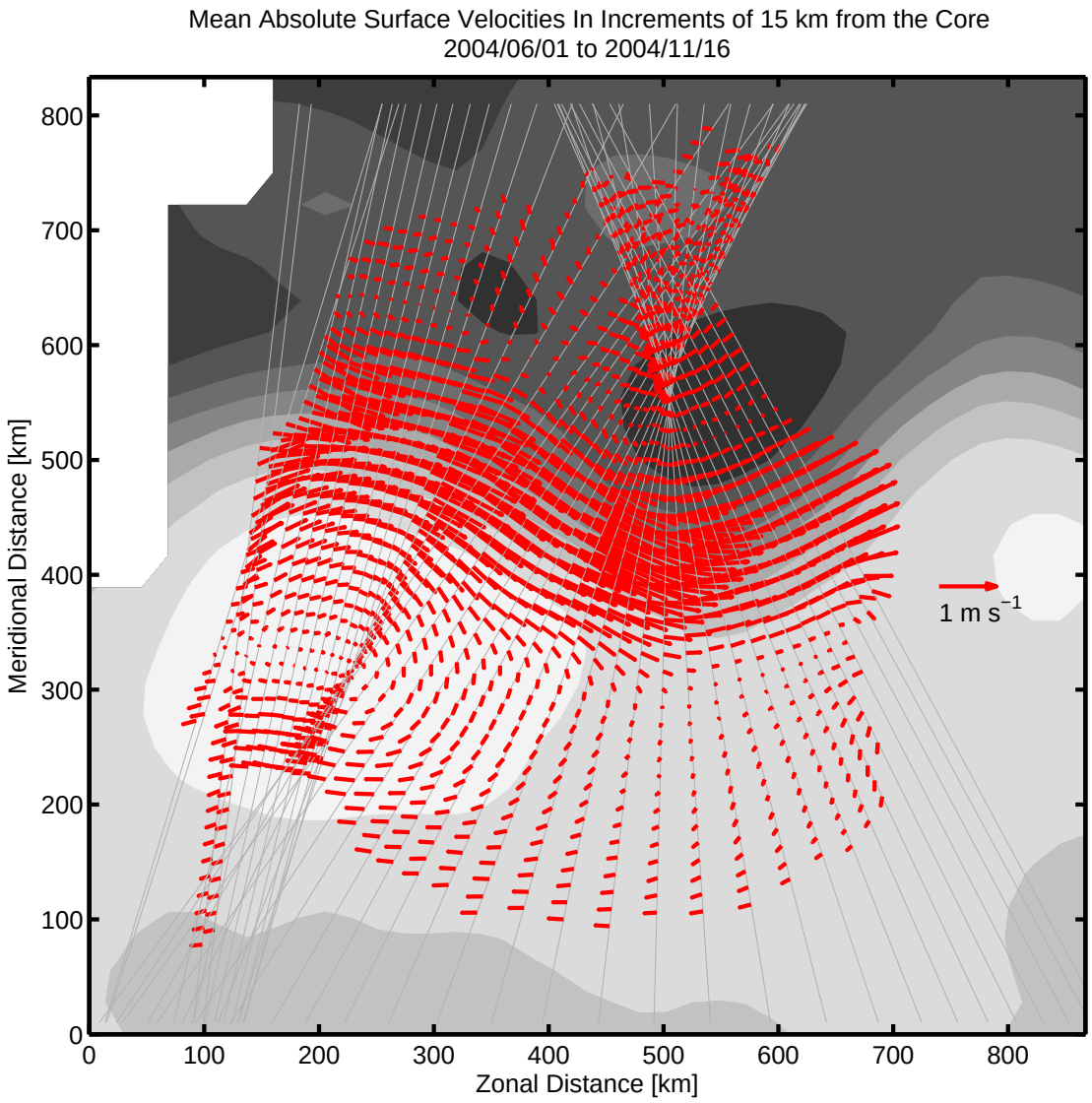

Figure 1.40: As in Figure 1.38 but for surface velocities only, at fixed $\frac{1}{8}^{th}$-degree longitudinal spacing. Note tendency of down-stream velocities to peel off into southern recirculation gyre south of first meander crest and trough.

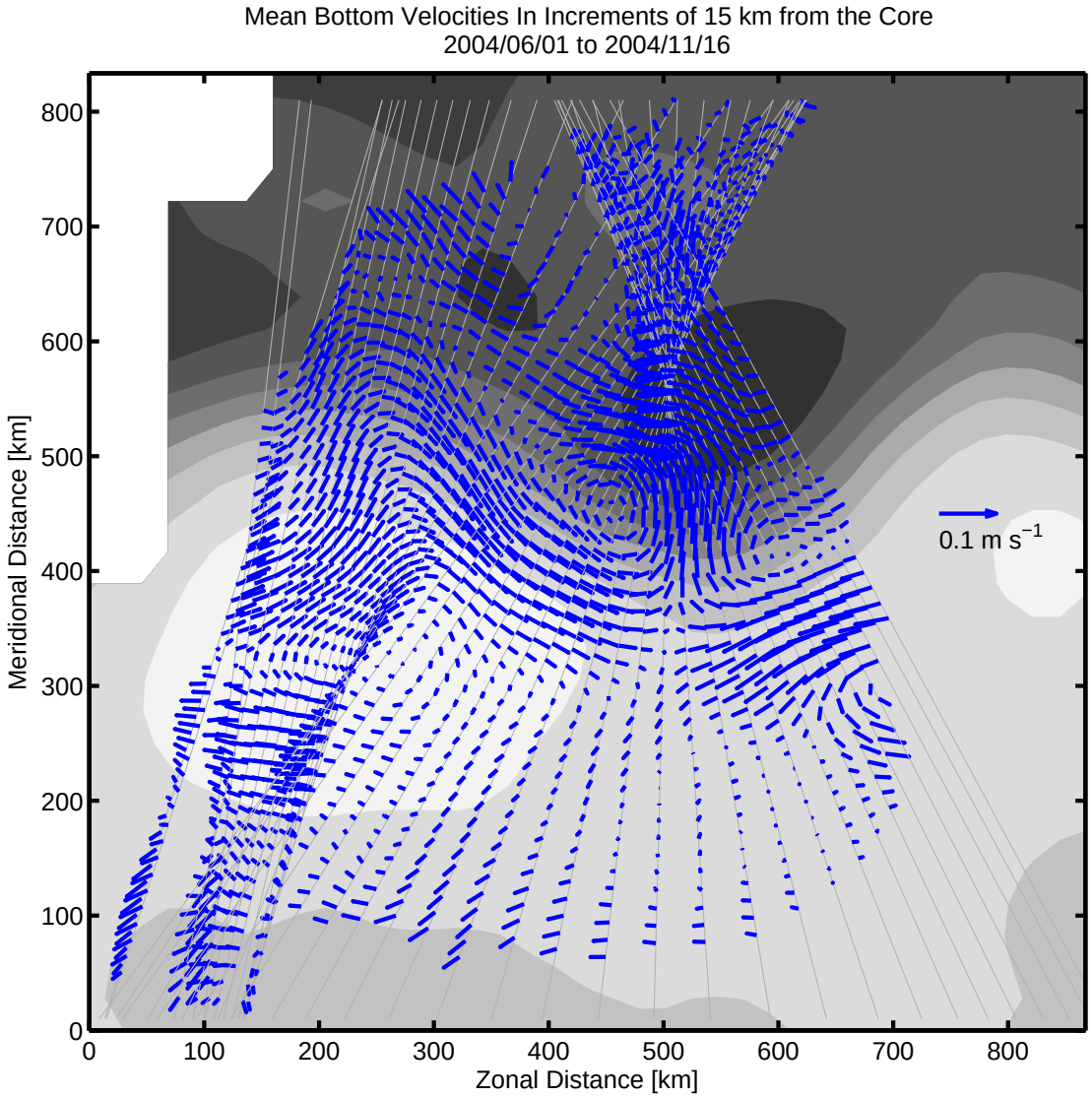

Figure 1.41: As in Figure 1.40 but for bottom velocities. Note cross-stream stretching of meander pattern at depth compared to the surface pattern between the first crest and trough. Also note mean presence of deep eddy on northern side of first meander trough.

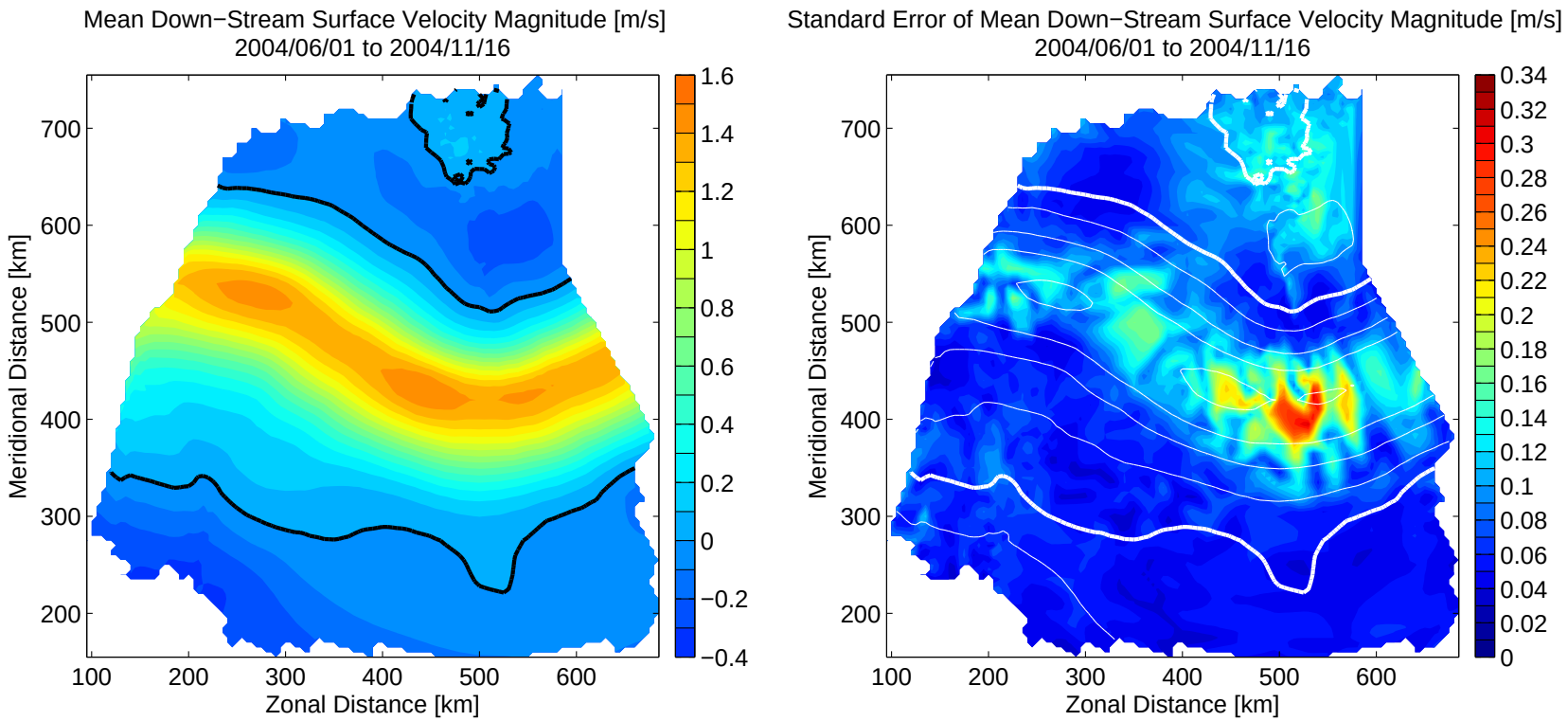

Figure 1.42: (left) Plan view of mean down-stream surface velocity magnitude contoured from $\frac{1}{8}^{th}$-degree longitudinal-spaced cross-stream transects. Heavy black contours indicate zero down-stream velocity magnitude. (right) Standard error of down-stream surface velocity magnitude. White contours indicate surface down-stream velocity magnitude, provided for context. Note the apparent existence of "jet streaks" in the surface down-stream velocity, as observed by *Howden and Watts* [1999] in the Gulf Stream.

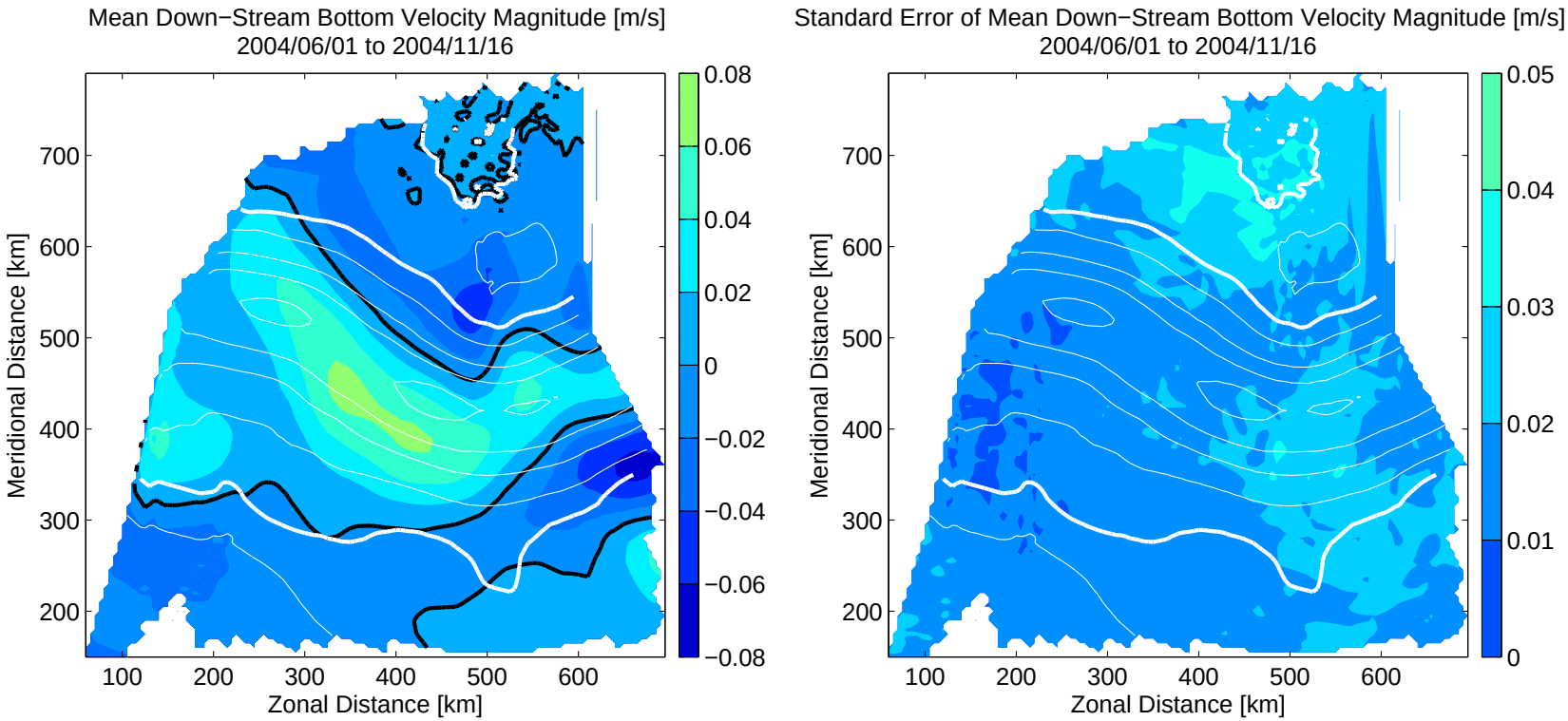

Figure 1.43: As in Figure 1.42 but colors indicate mean down-stream bottom velocity magnitude and associated standard error. Black contours indicate zero down-stream bottom velocity. White contours are surface down-stream velocity magnitude, provided for context.

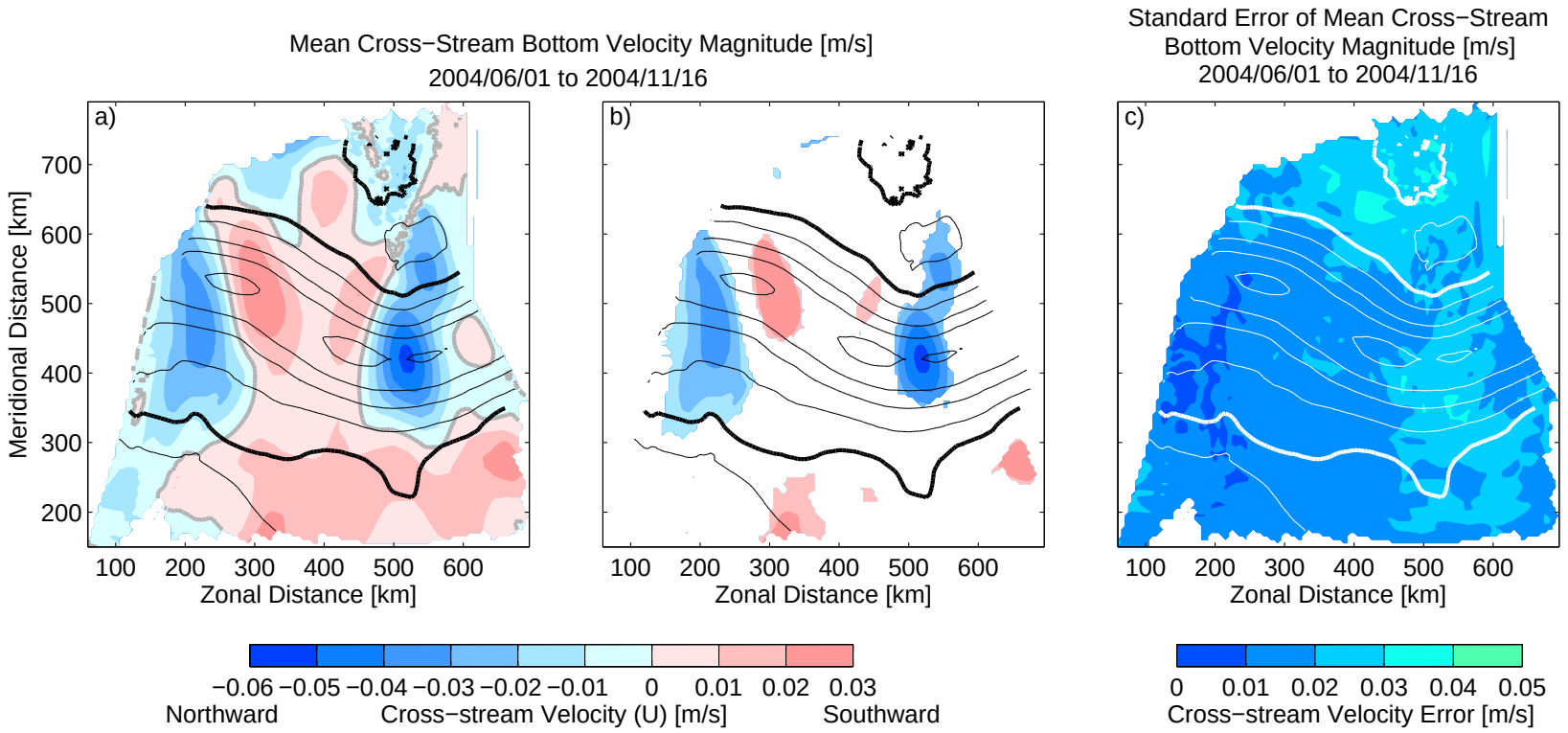

Figure 1.44: As in Figure 1.43 but colors indicate mean cross-stream bottom velocity magnitude and associated standard error. In panel *a* the full field is shown, as in Figure 1.43, with gray contours indicating zero cross-stream velocity magnitude. In panel *b*, velocities with magnitudes less than the value of the standard error (panel *c*) have been masked out. Surface down-stream contours are provided in all three for context, indicated in black in panels *a* and *b* and white in panel *c*. Note that positive (negative) velocities imply southward (northward) flow.

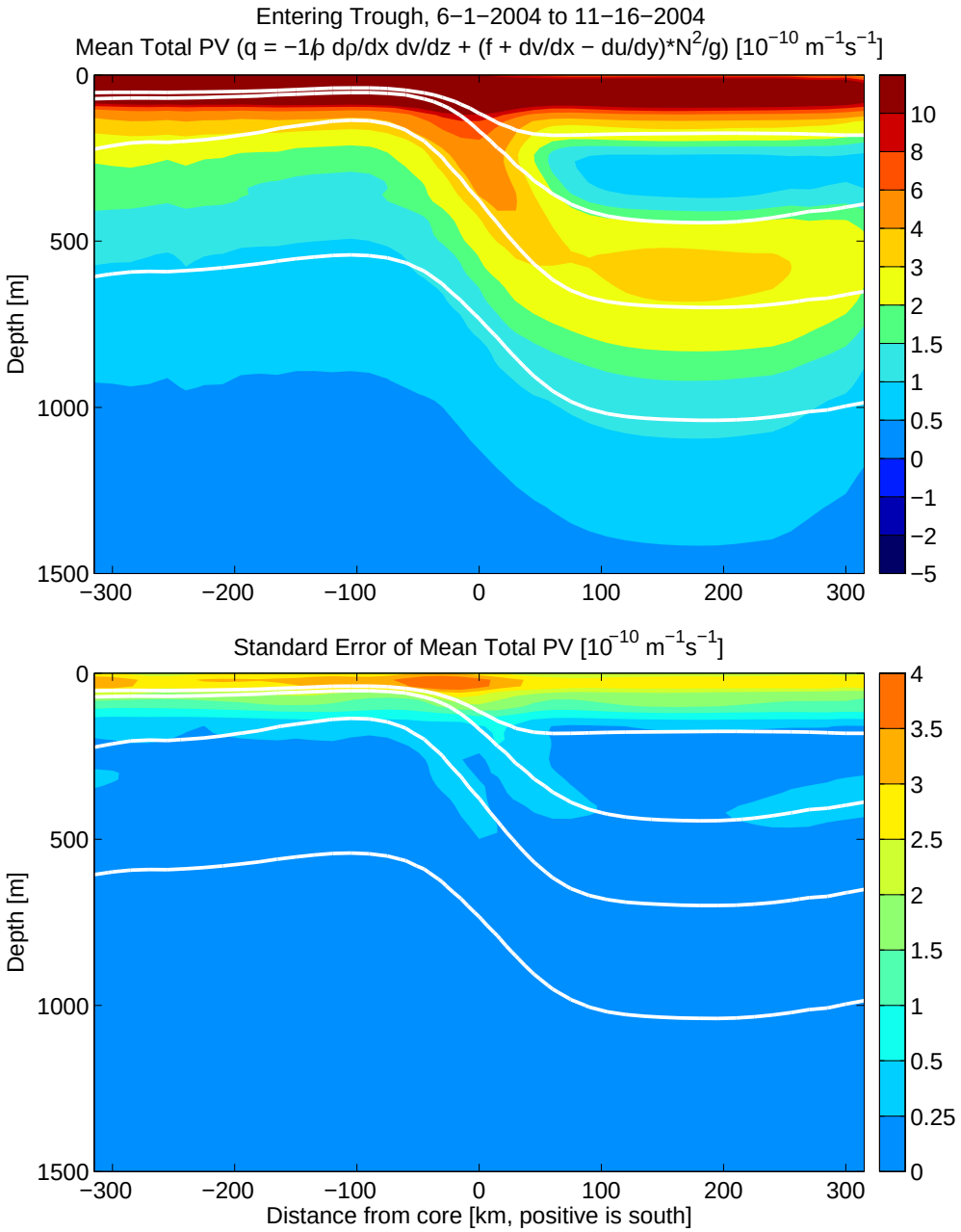

Figure 1.45: Mean total PV and error from mapped CPIES entering trough. Compare to basic structure from the survey mean in Figure 1.16. See text for discussion of similarities and differences between the two. White contours indicate σ_θ = 25.1, 25.5, 26.4, and 27.1.

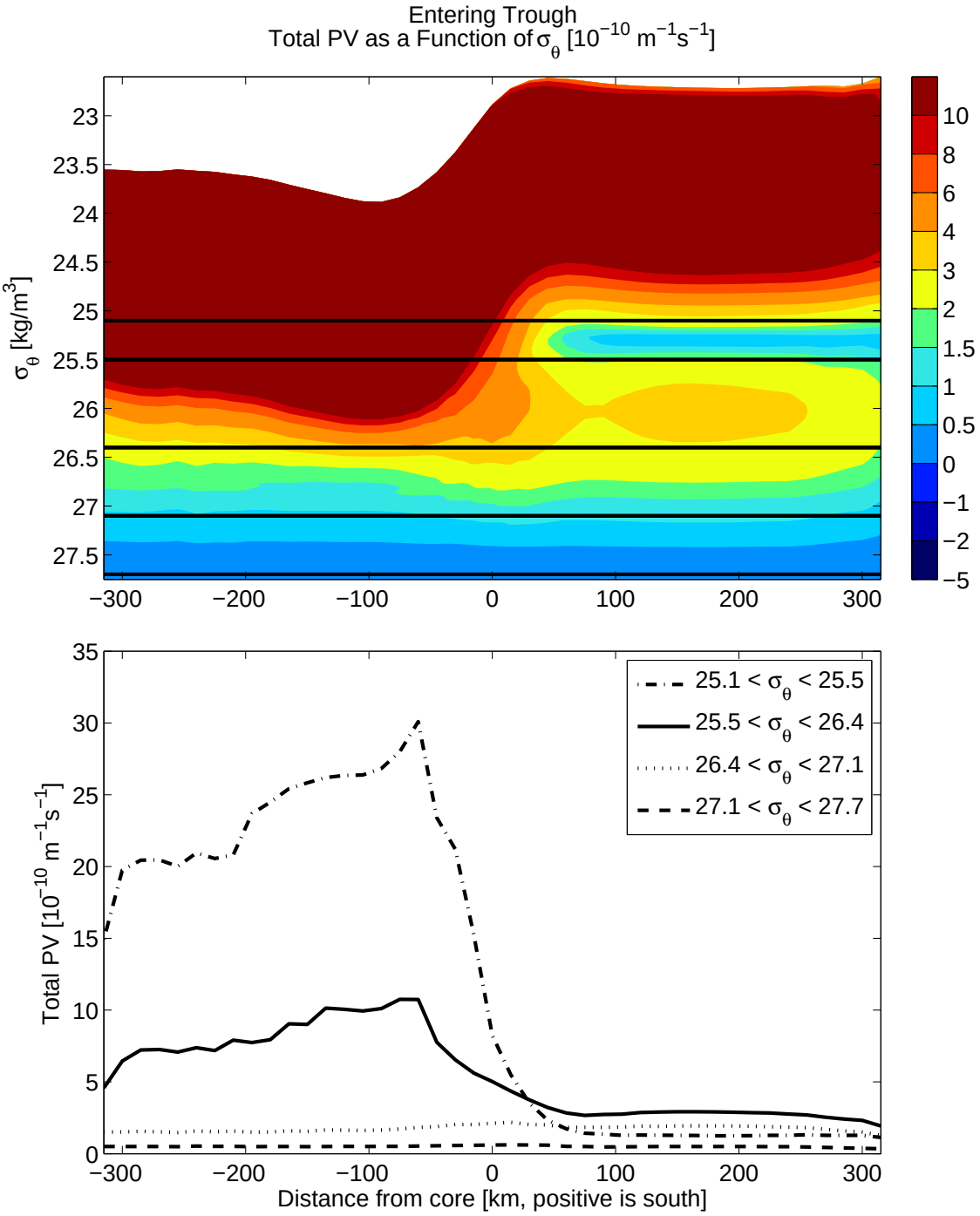

Figure 1.46: (top) Mean total PV as a function of σ_θ from mapped CPIES entering trough. Black lines indicate σ_θ = 25.1, 25.5, 26.4, 27.1, and 27.7. Compare to Figure 1.22 from surveys. The same mode water, mid-thermocline, lower-thermocline/NPIW, and deep PV-gradient regimes are evident. (bottom) Total PV averaged over the four layers identified in the top panel, as indicated by the key.

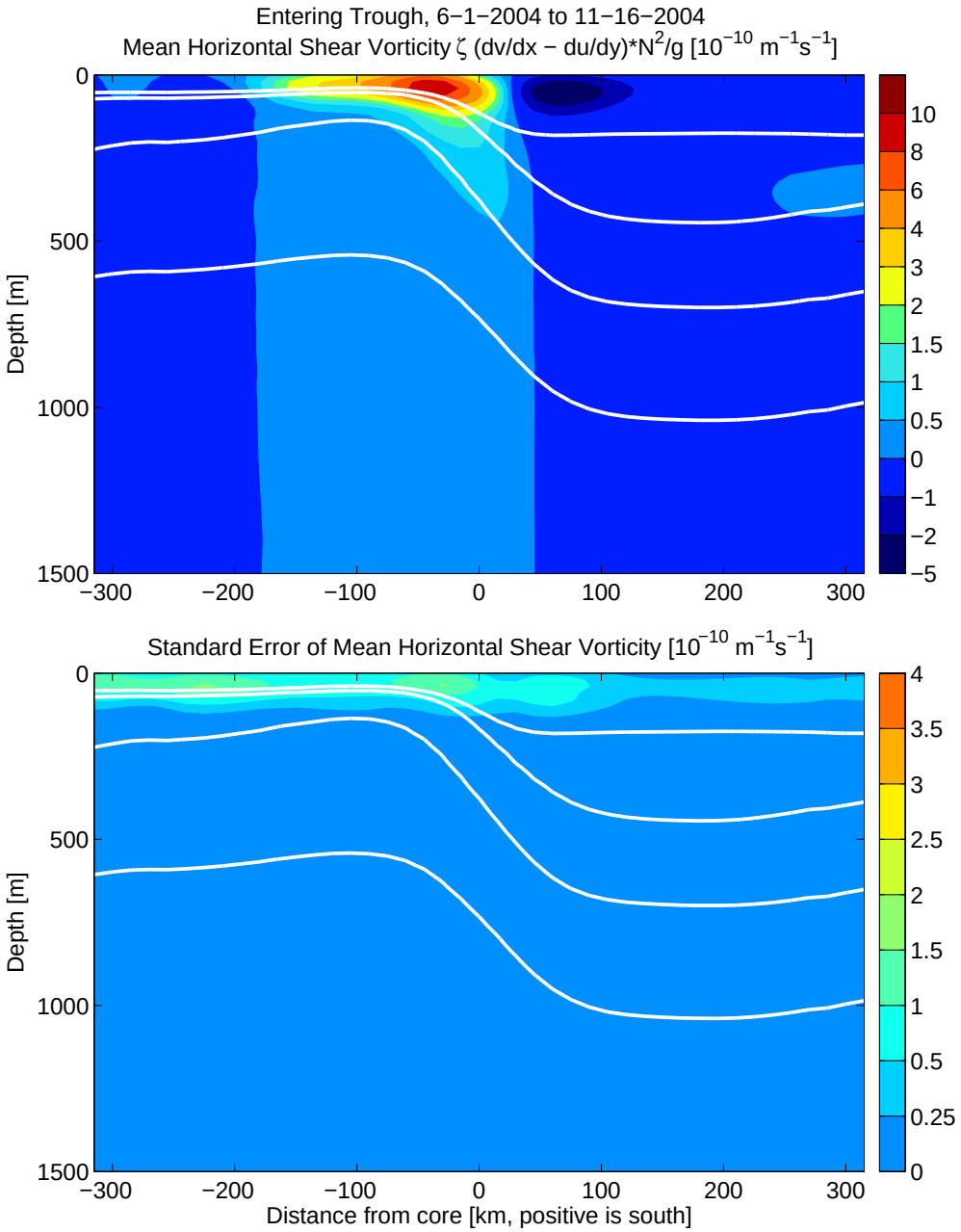

Figure 1.47: Mean horizontal shear vorticity and errors from mapped CPIES entering trough. Compare to shear vorticity from surveys in Figure 1.17. White contours indicate σ_θ = 25.1, 25.5, 26.4, and 27.1.

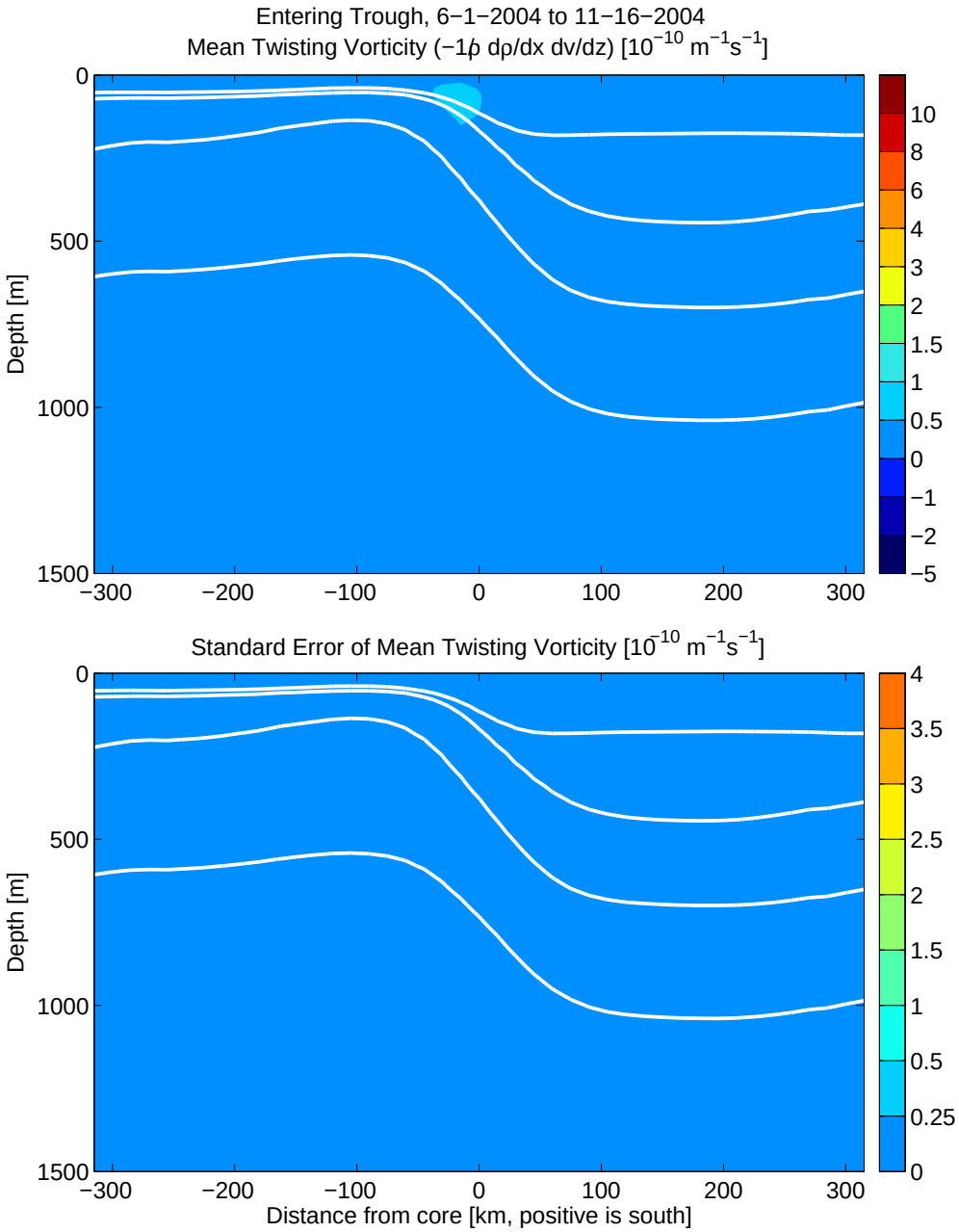

Figure 1.48: Mean twisting vorticity and errors from mapped CPIES entering trough. Compare to twisting vorticity from surveys in Figure 1.19. White contours indicate σ_θ = 25.1, 25.5, 26.4, and 27.1.

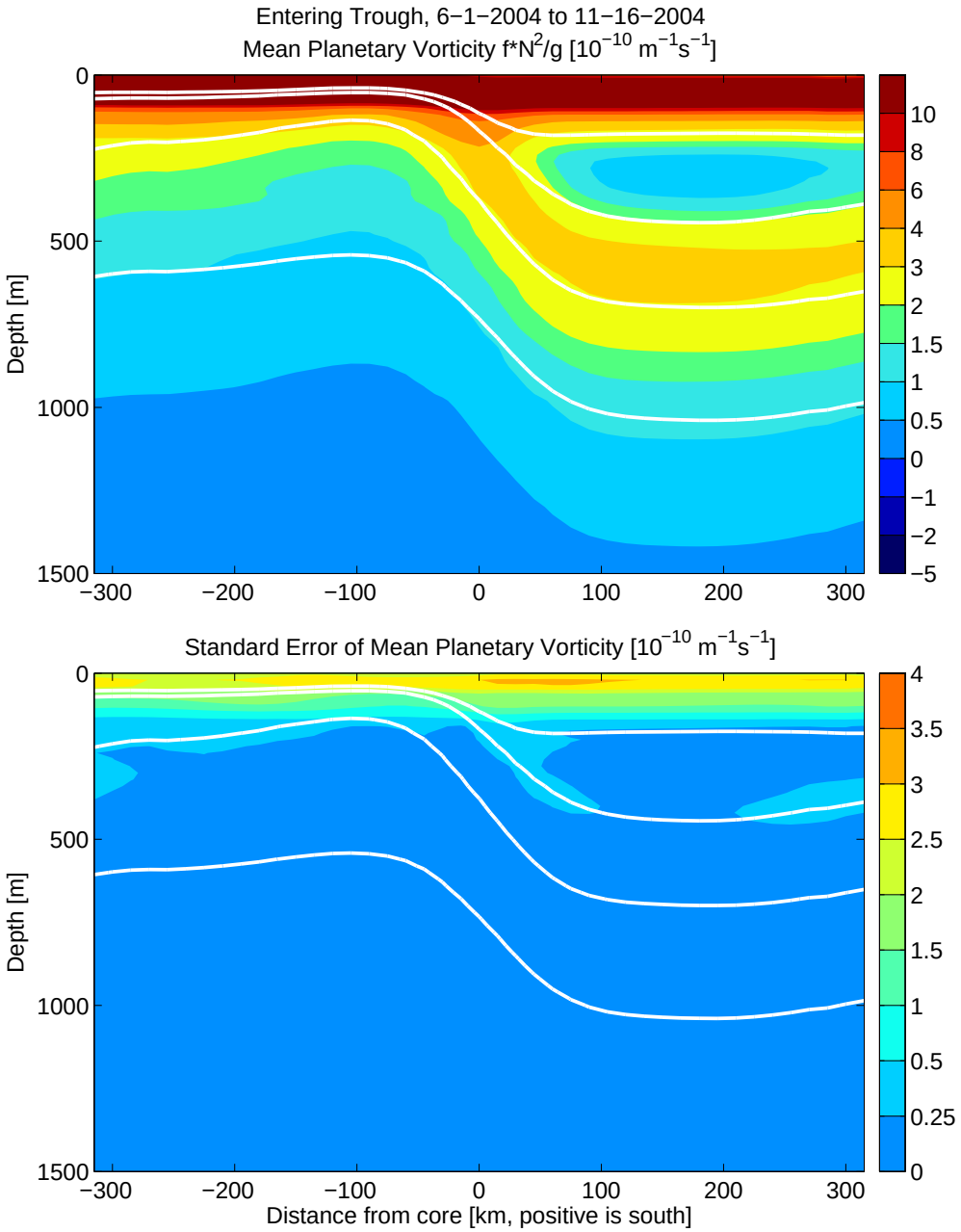

Figure 1.49: Mean planetary vorticity and errors from mapped CPIES entering trough. Compare to planetary vorticity from surveys in Figure 1.20. White contours indicate σ_θ = 25.1, 25.5, 26.4, and 27.1.

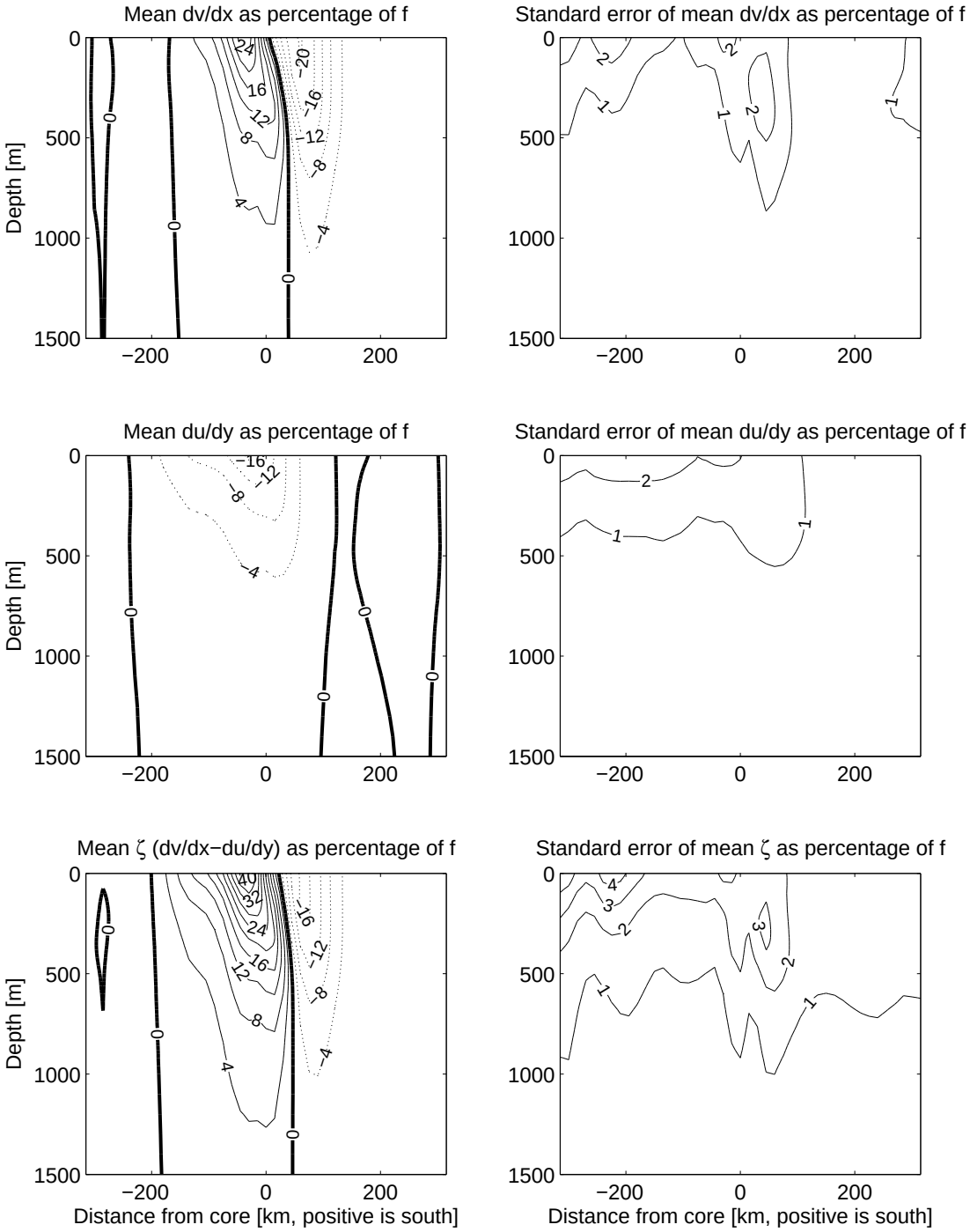

Figure 1.50: Mean $\frac{\partial v}{\partial x}$, $\frac{\partial u}{\partial y}$, and ζ as percentages of f and associated errors from mapped CPIES entering trough. Dotted contours indicate negative values. Bold contour is zero. Horizontal and vertical range have been reduced from the available data to highlight only the relevant jet region.

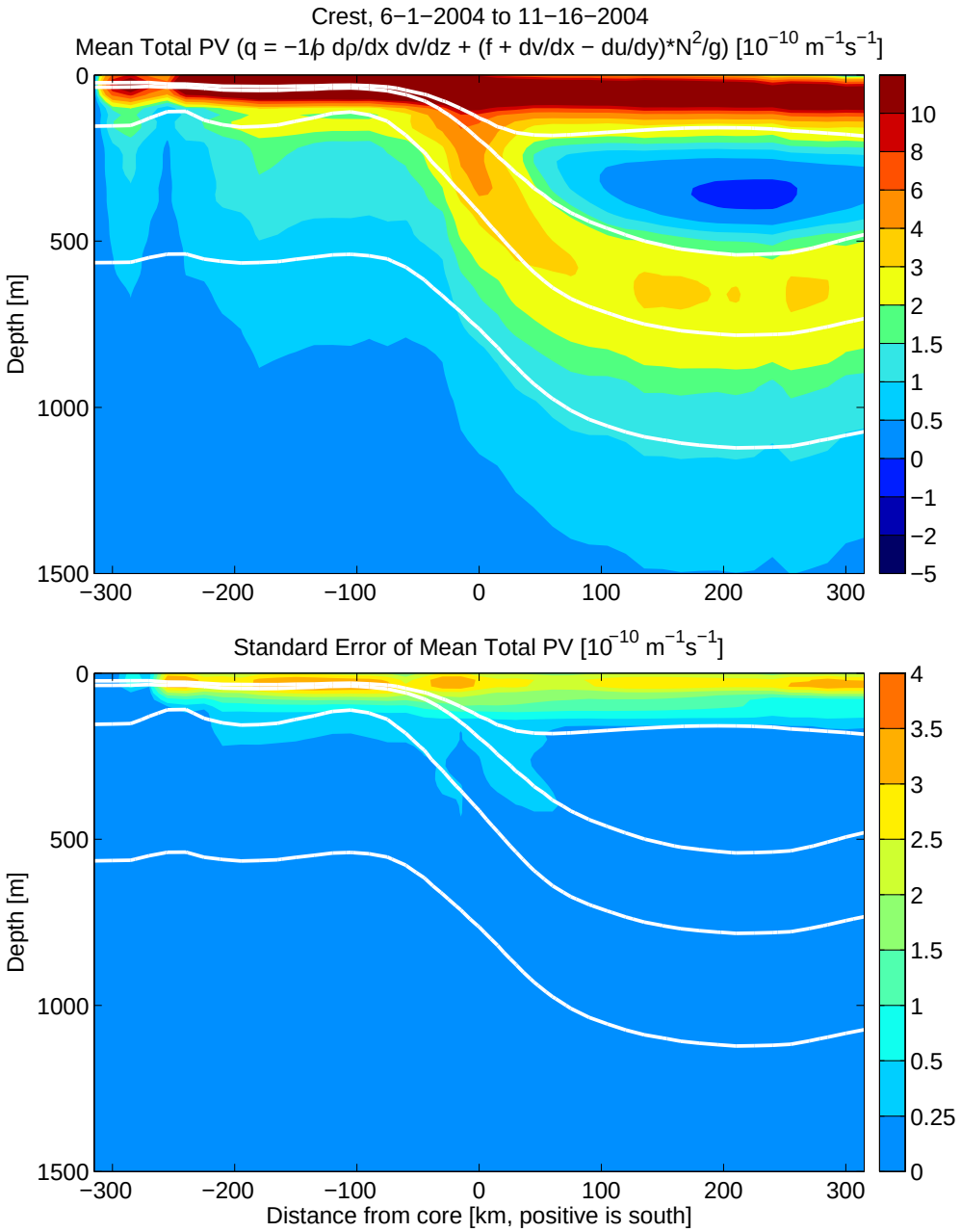

Figure 1.51: Mean total PV and errors from mapped CPIES in crest (143.75°E). See text for discussion of similarities and differences between crest and trough. White contours indicate σ_θ = 25.1, 25.5, 26.4, and 27.1.

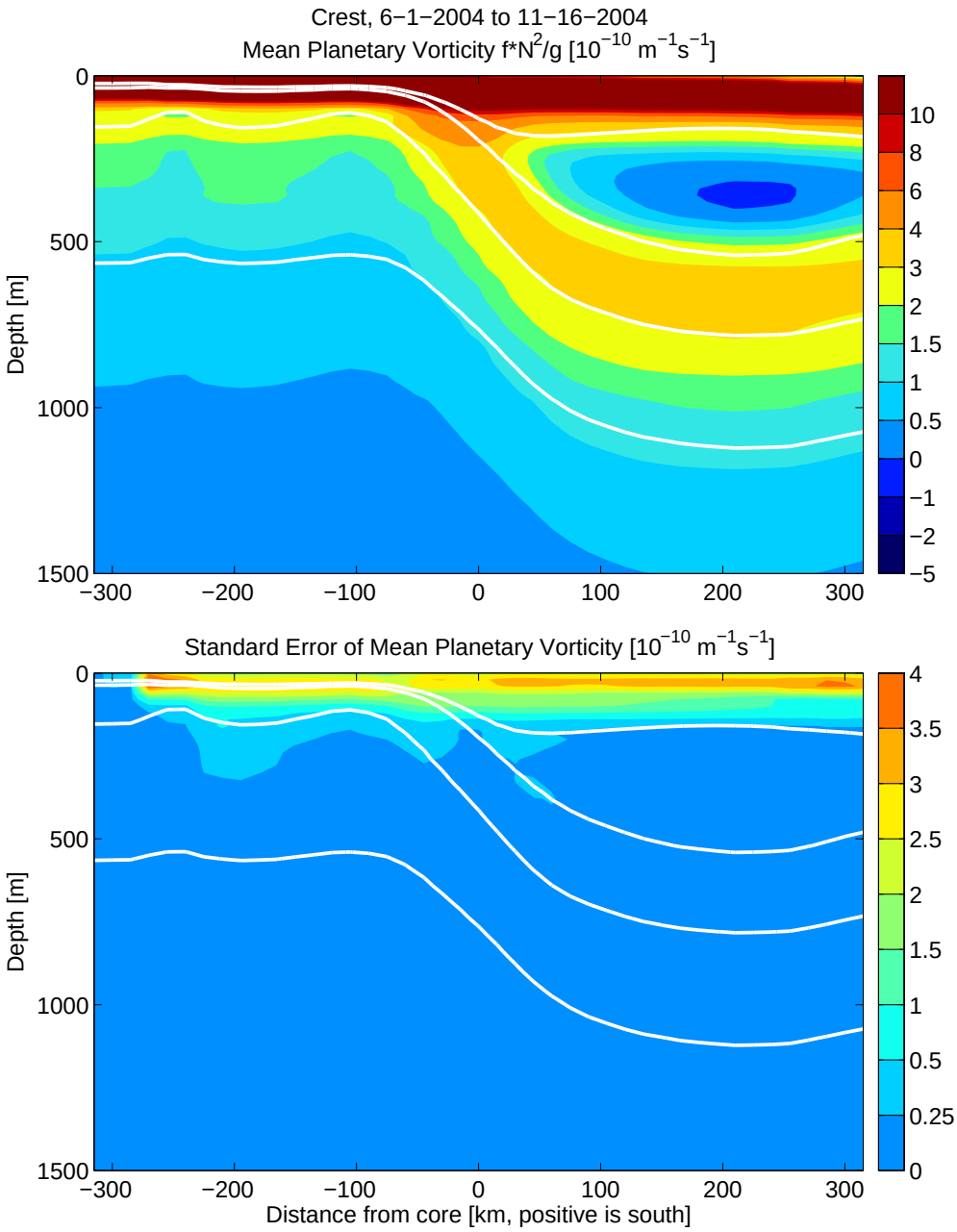

Figure 1.52: Mean thickness vorticity and errors from mapped CPIES in crest (143.75°E). See text for discussion. White contours indicate σ_θ = 25.1, 25.5, 26.4, and 27.1.

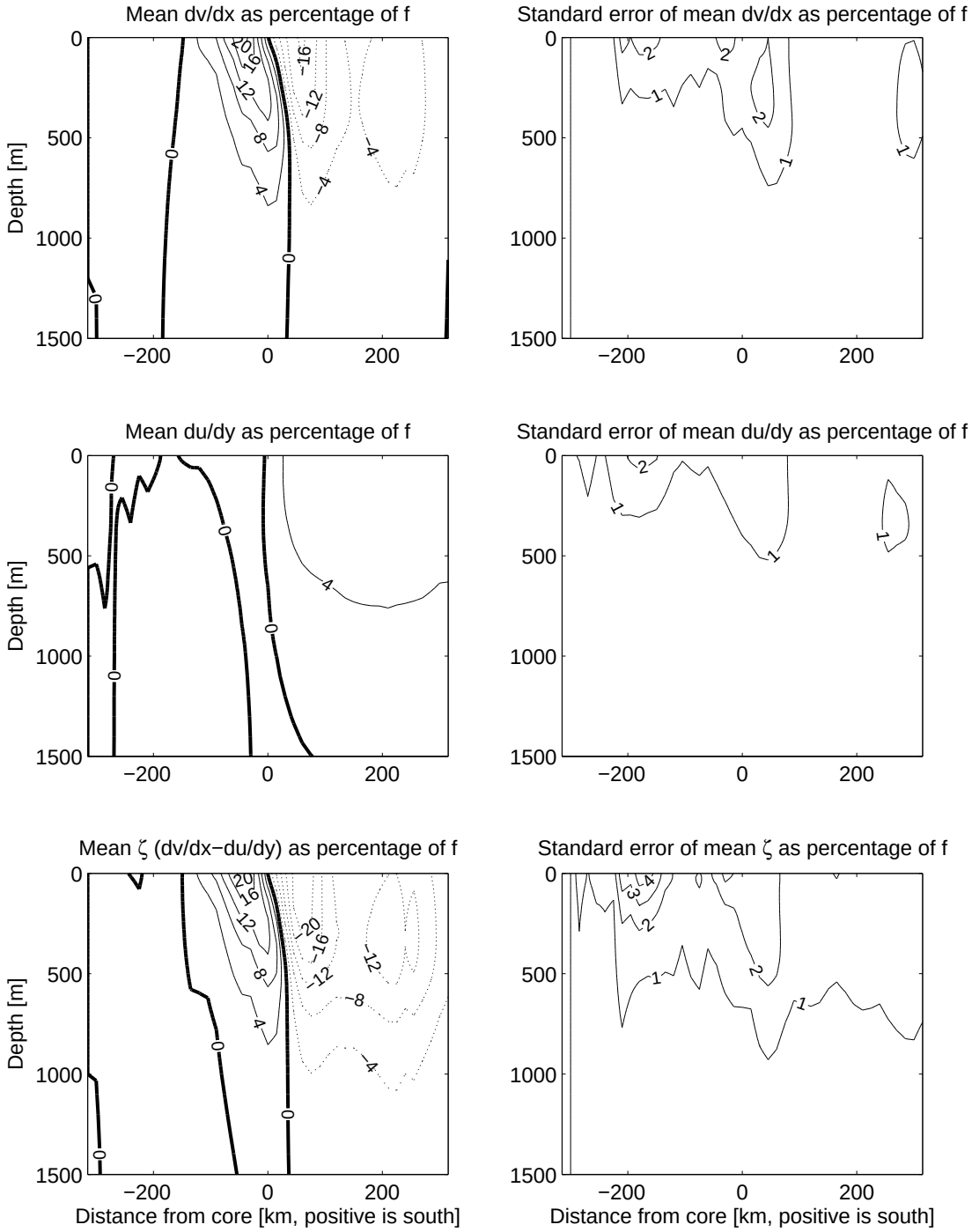

Figure 1.53: Mean $\frac{\partial v}{\partial x}$, $\frac{\partial u}{\partial y}$, and ζ as percentages of f and errors from mapped CPIES in crest (143.75°E). Dotted contours indicate negative values. Bold contour is zero. Horizontal and vertical range have been reduced from the available data to highlight only the relevant jet region.

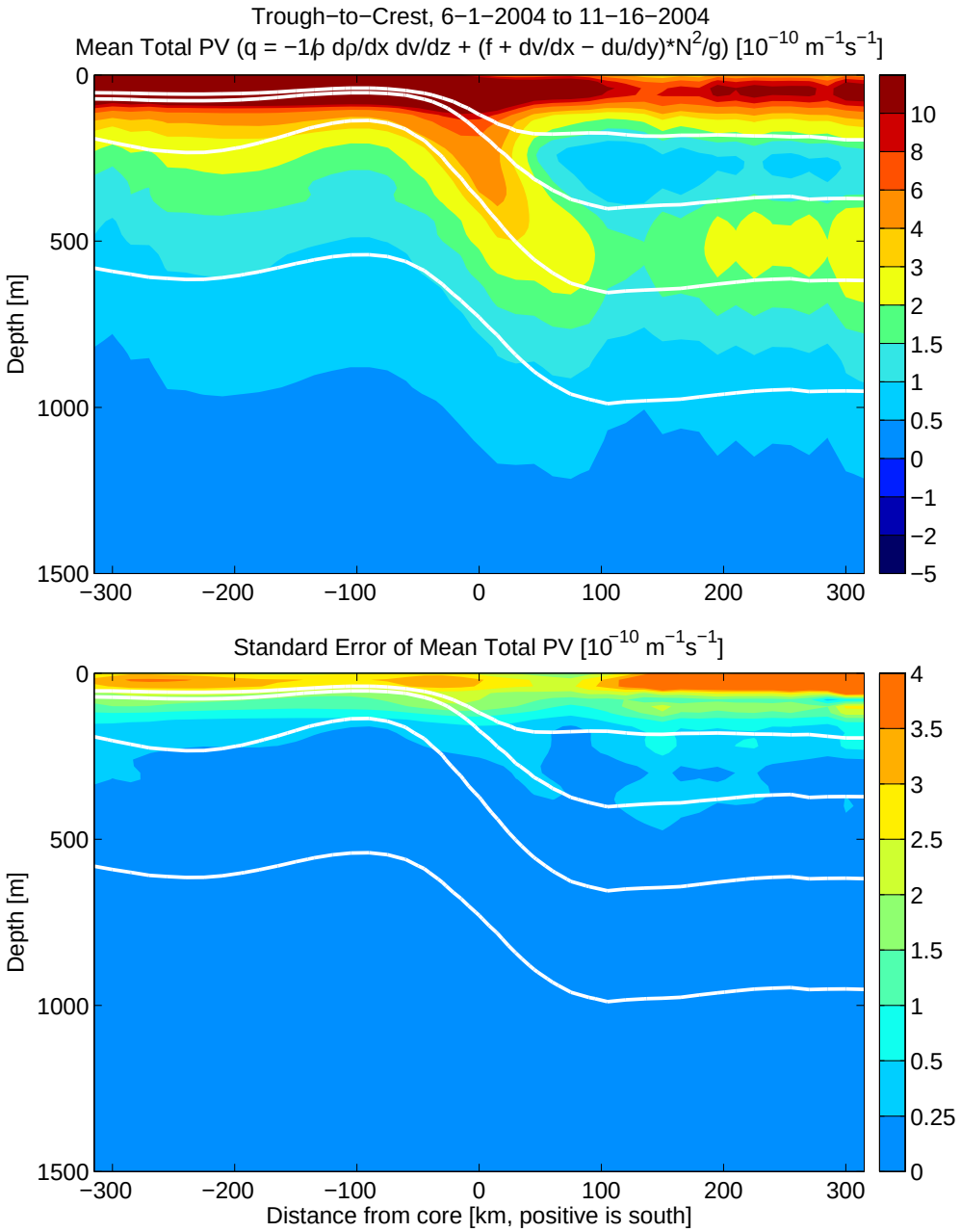

Figure 1.54: Mean total PV and errors from mapped CPIES between trough and second crest (148.5°E). See text for discussion of similarities and differences between this location and trough. White contours indicate σ_θ = 25.1, 25.5, 26.4, and 27.1.

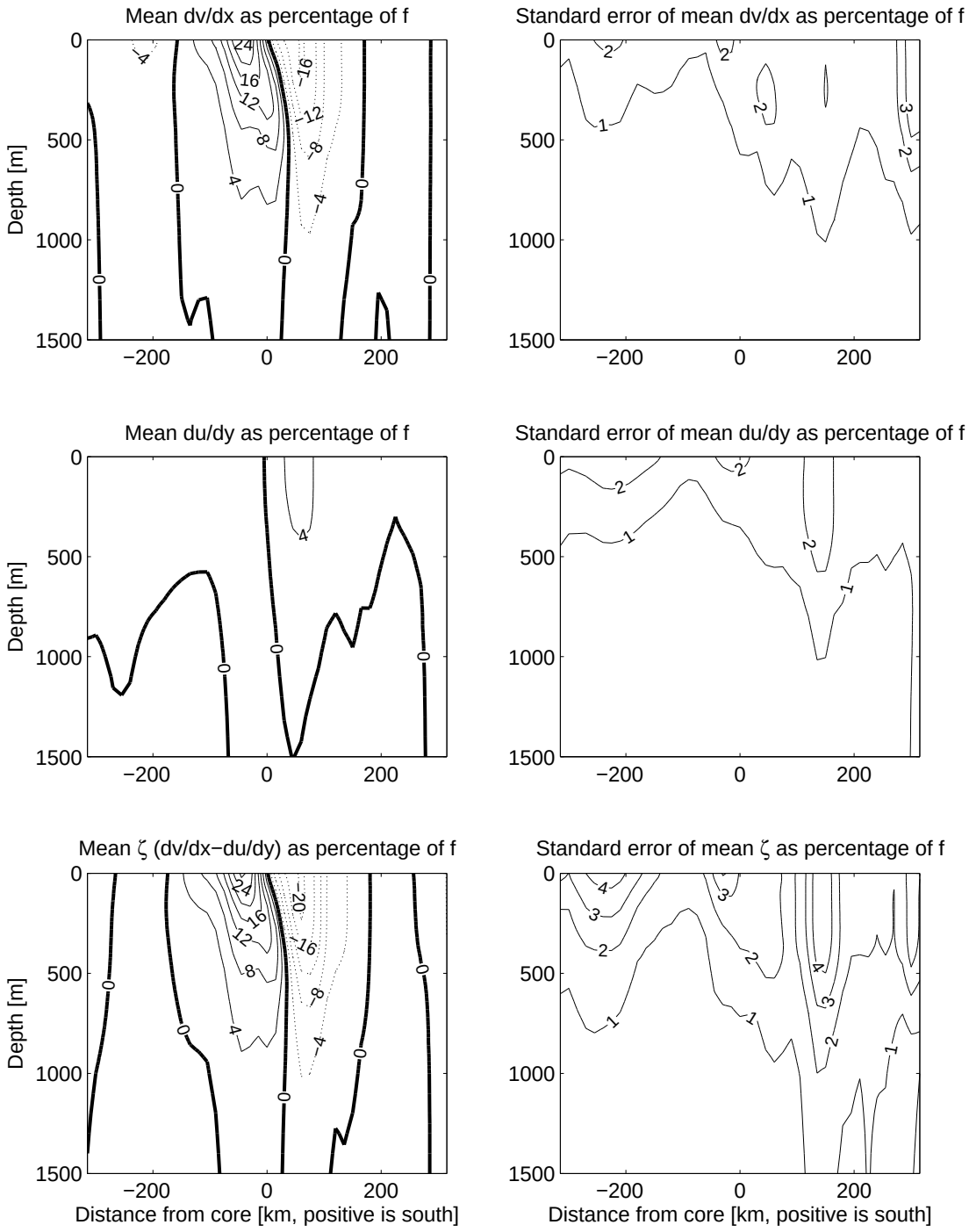

Figure 1.55: Mean $\frac{\partial v}{\partial x}$, $\frac{\partial u}{\partial y}$, and ζ as percentages of f and errors from mapped CPIES between trough and second crest (148.5°E). Dotted contours indicate negative values. Bold contour is zero. Horizontal and vertical range have been reduced from the available data to highlight only the relevant jet region.

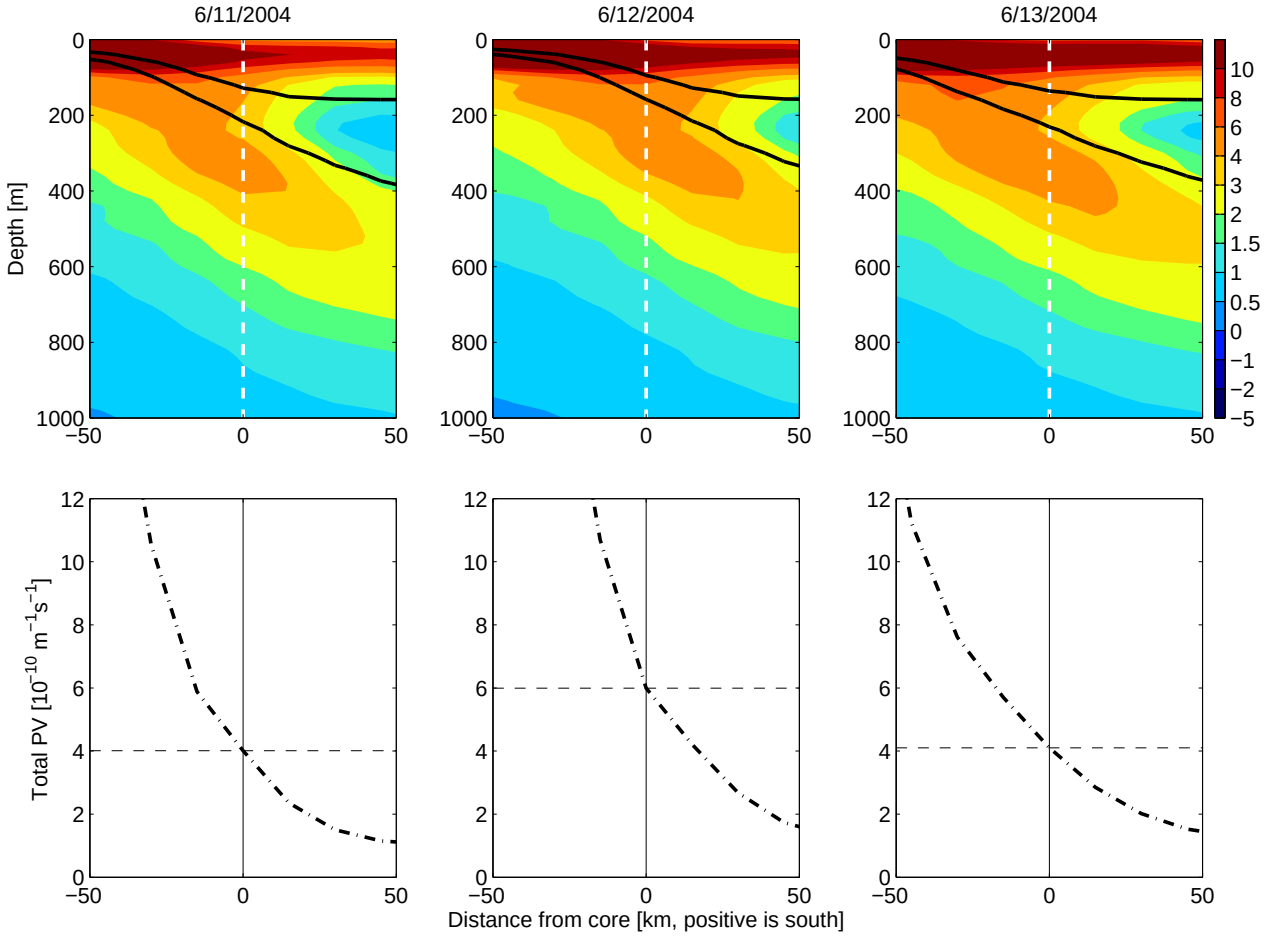

Figure 1.56: Total PV across the KE core at a fixed longitude on three consecutive days. Top panels show PV structure with depth, with dashed white lines indicating the location of the core and black contours indicating $\sigma_\theta = 25.1$ and 25.5. Bottom panels show total PV averaged over the $\sigma_\theta = 25.1$ to 25.5 layer, with solid black lines indicating the location of the core and dashed black line indicating the value of the total PV at the core. Note apparent lateral shifting of PV structure across the core.

List of References

Bendat, J. S., and A. G. Piersol (2000), *Random Data: Analysis and Measurement Procedures*, 3rd ed., Wiley, John and Sons, Incorporated, New York.

Bower, A. S. (1989), Potential Vorticity Balances and Horizontal Divergence along Particle Trajectories in Gulf Stream Meanders East of Cape Hatteras, *J. Phys. Oceanogr.*, *19*(11), 1669–1681.

Bower, A. S. (1991), A Simple Kinematic Mechanism for Mixing Fluid Parcels across a Meandering Jet, *J. Phys. Oceanogr.*, *21*(1), 173–180.

Bower, A. S., and T. Rossby (1989), Evidence of Cross-Frontal Exchange Processes in the Gulf Stream Based on Isopycnal RAFOS Float Data, *J. Phys. Oceanogr.*, *19*(9), 1177–1190.

Bower, A. S., H. T. Rossby, and J. L. Lillibridge (1985), The Gulf Stream - Barrier or Blender?, *J. Phys. Oceanogr.*, *15*(1), 24–32.

Donohue, K. A., D. R. Watts, K. L. Tracey, A. D. Greene, and M. Kennelly (2008), Mapping circulation in the Kuroshio Extension with an array of Current and Pressure recording Inverted Echo Sounders, in progress.

Halkin, D., and T. Rossby (1985), The Structure and Transport of the Gulf Stream at 73°W, *J. Phys. Oceanogr.*, *15*(11), 1439–1452.

Hall, M. M. (1989), Velocity and Transport Structure of the Kuroshio Extension at 35°N, 152°E, *J. Geophys. Res.*, *94*(10), 14,445–14,459.

Holton, J. R. (1992), *An Introduction to Dynamic Meteorology*, 3rd ed., Academic Press, San Diego.

Howden, S. D., and D. R. Watts (1999), Jet streaks in the Gulf Stream, *J. Phys. Oceanogr.*, *29*, 1910–1924.

Johns, W. E., T. J. Shay, J. M. Bane, and D. R. Watts (1995), Gulf Stream Structure, Transport, and Recirculation near 68°W, *J. Geophys. Res.*, *100*(C1), 817–838.

Joyce, T. M., I. Yasuda, Y. Hiroe, K. Komatsu, K. Kawasaki, and F. Bahr (2001), Mixing in the Meandering Kuroshio Extension and the Formation of North Pacific Intermediate Water, *J. Geophys. Res.*, *106*(C3), 4397–4404.

Kouketsu, S., I. Yasuda, and Y. Hiroe (2005), Observation of Frontal Waves and Associated Salinity Minimum Formation Along the Kuroshio Extension, *J. Geophys. Res.*, *110*, doi: 10.1029/2004JC002862.

Kouketsu, S., I. Yasuda, and Y. Hiroe (2007), Three-Dimensional Structure of Frontal Waves and Associated Salinity Minimum Formation Along the Kuroshio Extension, *J. Phys. Oceanogr.*, *37*, 644–656.

Liu, M., and T. Rossby (1993), Observations of Velocity and Vorticity Structure of Gulf Stream Meanders, *J. Phys. Oceanogr.*, *23*(2), 329–345.

Logoutov, O., G. Sutyrin, and D. R. Watts (2001), Potential Vorticity Structure Across the Gulf Stream: Observations and a PV-Gradient Model, *J. Phys. Oceanogr.*, *31*(2), 637–644.

Meinen, C. S., D. S. Luther, D. R. Watts, A. D. Chave, and K. L. Tracey (2003), Mean Stream Coordinate Structure of the Subantarctic Front: Temperature, Salinity, and Absolute Velocity, *J. Geophys. Res.*, *108*(C8), doi:10.1029/2002JC001545.

Meinen, C. S., D. S. Luther, and M. O. Baringer (2008), Structure, transport, and potential vorticity of the Gulf Stream at 68°W: Revisiting older data sets with new techniques, *Deep-Sea Res.*, to appear.

Mizuno, K., and W. B. White (1983), Annual and Interannual Variability in the Kuroshio Current System, *J. Phys. Oceanogr.*, *13*(10), 1847–1867.

Qiu, B., and S. Chen (2005), Variability of the Kuroshio Extension Jet, Recirculation Gyre, and Mesoscale Eddies on Decadal Time Scales, *J. Phys. Oceanogr.*, *35*(11), 2090–2103.

Qiu, B., S. Chen, P. Hacker, N. G. Hogg, S. R. Jayne, and H. Sasaki (2008), The Kuroshio Extension Northern Recirculation Gyre: Profiling Float Measurements and Forcing Mechanism, *J. Phys. Oceanogr.*, to appear.

Rajamony, J., D. Hebert, and T. Rossby (2001), The Cross-Stream Potential Vorticity Front and Its Role in Meander-Induced Exchange in the Gulf Stream, *J. Phys. Oceanogr.*, *31*(12), 3551–3568.

Rossby, T., and E. Gottlieb (1998), The *Oleander* Project: Monitoring the Variability of the Gulf Stream and Adjacent Waters between New Jersey and Bermuda, *Bull. Amer. Meteorol. Soc.*, *79*(1), 5–18.

Rossby, T., and H.-M. Zhang (2001), The Near-Surface Velocity and Potential Vorticity Structure of the Gulf Stream, *J. Mar. Res.*, *59*, 949–975.

Sun, C., and D. R. Watts (2001), A Circumpolar Gravest Empirical Mode for the Southern Ocean Hydrography, *J. Geophys. Res.*, *106*(C2), 2833–2855.

Taguchi, B., S.-P. Xie, H. Mitsudera, and A. Kubokawa (2005), Response of the Kuroshio Extension to Rossby Waves Associated with the 1970s Climate Regime Shift in a High-Resolution Ocean Model, *J. Climate*, *18*(15), 2979–2995.

Talley, L. D., and J.-Y. Yun (2000), The Role of Cabbeling and Double Diffusion in Setting the Density of the North Pacific Intermediate Water Salinity Minimum, *J. Phys. Oceanogr.*, *31*(6), 1538–1549.

Talley, L. D., Y. Nagata, M. Fujimara, T. Iwao, T. Kono, D. Inagake, M. Hirai, and K. Okuda (1995), North Pacific Intermediate Water in the Kuroshio/Oyashio Mixed Water Region, *J. Phys. Oceanogr.*, *25*(4), 475–501.

Teague, W. J., M. J. Carron, and P. J. Hogan (1990), A Comparison Between the Generalized Digital Environmental Model and Levitus Climatologies, *J. Geophys. Res.*, *95*(C5), 7167–7183.

Watts, D. R., K. L. Tracey, J. M. Bane, and T. J. Shay (1995), Gulf Stream path and thermocline structure near 74°W and 68°W, *J. Geophys. Res.*, *100*(C9), 18,291–18,312.

Yasuda, I., K. Okuda, and Y. Shimizu (1996), Distribution and Modification of North Pacific Intermediate Water in the Kuroshio-Oyashio Interfrontal Zone, *J. Phys. Oceanogr.*, *26*(4), 448–465.

APPENDIX A

ADCP Processing and Error Estimates

The Acoustic Doppler Current Profiler (ADCP) makes use of the Doppler effect to measure radial velocities parallel to the four acoustic beams of the ADCP transducer. Acoustic pulses from each transducer beam reflect off scatterers in the water column, such as plankton and other passive particles that do not self-propel and hence move at the same speed as the surrounding water. By measuring the Doppler shift of the echos of these transmitted pulses, the radial velocity of the scatterers relative to the ADCP is determined. Using three acoustic beams allows calculation of three orthogonal components of velocity, and adding a fourth beam produces a redundant estimate of vertical velocity, which can be compared to its counterpart to determine the amount of random error in the measurements. The value resulting from this comparison is referred to as the error velocity. Range-gating the reflected pulses allows calculation of a velocity profile, as reflections from greater distances take longer to return to the transducer. Regularly-spaced depth "bins" are specified prior to deployment of the instrument, and the resulting velocities reported by the ADCP represent center-weighted averages over the range of each depth bin. The angle of the transducer beams (typically 20-30° from vertical) combined with the range-gating process results in overlap between successive depth bins, which causes a correlation of about 15% between them. This value varies depending on the ratio of the size of the bins to the length of the transmitted sound pulse. Random error and noise are also reduced by the process of "ensemble averaging," in which single ping profiles are vector-averaged into groups before data transmission to the storage device occurs. Typical averaging periods are anywhere from 1 to 10 minutes. The data are then corrected for pitch, roll, and tilt angle of the transducer, and heading data from the ship's gyrocompass, ideally corrected with additional GPS navigation such as the Position and Orientation System for Marine Vessels (POS MV) or Ashtek, are used to rotate the velocities into earth coordinates. Finally, ship motion, equivalent to ADCP motion, is subtracted from the profiles to give absolute earth-referenced current velocities. These resultant profiles are

then processed and checked by the user for possible errors and interferences using standard post-processing software. For more details concerning the underlying principles of ADCP operation, see *RDI* [1996].

Although ADCP data has come to be regarded as a relatively reliable oceanographic data source, a considerable amount of post-processing is required to bring it to this point. The popularity of ADCPs in a wide range of oceanographic contexts prompted the development by scientists at the University of Hawai'i of a standardized software package to perform the necessary processing procedures. This package is referred to as the Common Ocean Data Access System (CODAS), and consists of a set of scripts that can be tailored by the user to the dataset in question to perform all steps from scanning the raw data files for completeness and readability to producing vector and contour plots of the resultant velocity profiles. A summary of CODAS processing will be provided here; an in-depth description is available from the creators themselves [*Firing et al.*, 1995].

Before loading the raw data files into the CODAS database, within which all processing procedures occur, a scanning process can be run to examine the raw data for readability and gaps or other acquisition problems. At this time, any necessary corrections can be made to the recorded profile times, which are most often inaccurate due to problems with the clock on the PC to which the data were transmitted. Once these corrections have been performed, the data are loaded into the CODAS database. Before examining individual profiles, the dataset as a whole can be evaluated by calculating and plotting some general statistics such as the signal strength, the percent good pings, the error velocity, the vertical velocity, and the vertical first difference of the horizontal velocity components. Comparing these variables in both on-station and underway periods can be helpful in determining the influence of the ship's motion on the dataset. Individual profiles are then evaluated via an automated system which flags values for each variable that do not lie within certain thresholds, which have default settings that can be user-modified if desired. The user is then presented with graphical representations of the profiles that contain the flagged

values and asked to determine by visual inspection and cross-examination with other details of the cruise environment whether to accept or reject the flagged values. This editing procedure is primarily intended to detect bottom interference or interference from fish or other scattering layers, physical intrusion of winch wires or other objects into the path of one or more of the beams, and random instrument or data acquisition system failures or inconsistencies in configuration. The next step corrects for possible misalignment of the ADCP transducer by calibrating with the gyrocompass, which is first corrected for bias and long-term Schüler oscillations by comparison with GPS heading data, if available. In relatively shallow water, the ADCP's bottom track mode can be used for this calibration, by comparing the ship's track as determined from the ADCP with that shown by the navigation records. Alternatively, in deep water as in the KESS region, a "water-track" assessment can be done to determine heading error by comparing on-station and underway readings. Finally, the absolute water velocities are determined by subtracting the ship's velocity from the relative velocity profiles, again using navigation data. If sound speed corrections at the transducer need to be made to alter the value from the nominal speed (1470 m/s) assumed by the RD Instruments ADCP, this is also done at this time. The data are now in an appropriate format for plotting and analysis.

The RD Instruments Ocean Surveyor 75 kHz model used during the deployment cruise of KESS penetrates to a nominal depth of 700 m [*RDI*, 1996]. Bin sizes were set to 16 m during the time of the feature surveys in order to reduce random error through vertical averaging, resulting in a total of 50 depth bins. The primary heading source was the ship's gyrocompass, with the POS MV providing satellite corrections to the gyro. Water-track assessment of heading accuracy during the KESS deployment cruise suggests an error of $<0.1^{\circ}$, which results in <1 cm/s error in the velocities when traveling at 10 knots. In addition, the water-track calibration determined a scale factor offset error of 1.0232, the cause of which is unknown. Ensemble averaging was performed over 5-minute intervals. The shallowest bin was contaminated by acoustic ringing, but performance was good throughout the rest of the depth range, with good data reaching consistently down to 650-750 m [*Greene et al.*, 2004].

List of References

Firing, E., J. Ranada, and P. Caldwell (1995), *Processing ADCP Data with the CO-DAS Software System Version 3.1*, Joint Institute for Marine and Atmospheric Research, University of Hawaii, and National Oceanography Data Center, Available at *http://currents.soest.hawaii.edu/docs/doc/index.html*, (accessed 28 May, 2008).

Greene, A., C. Ashmankas, K. Donohue, R. Watts, G. Chaplin, and K. Tracey (2004), KESS Deployment Cruise Report, unpublished.

RDI (1996), *Acoustic Doppler Current Profiler Principles of Operation: A Practical Primer*, RD Instruments, 9855 Businesspark Ave., San Diego, California 92131, 2 ed.

APPENDIX B

Stream Coordinates Definition Methods

As is discussed in the main text, various methods have been used in past studies to define stream-coordinate systems from which to perform structural analysis of baroclinic jets. Of course, the type of data available in any one study in large part determines the methods which may be employed for analysis. In general, three steps are required for all datasets; however, the order of the second and third steps changes depending on the type of data in use. The first step is always to define the origin of the coordinate system, which often corresponds to the high-velocity *core* of the current. If the dataset includes fine horizontal-scale cross-sectional measurements of velocity, as in KESS, the second step is to determine the down-stream direction, and the final step is to project the data points onto the normal line to determine cross-stream distance from the core. If, on the other hand, the velocity data come from a single mooring or are spread out on coarser horizontal scales in a 2-D mooring array, as in the SAFDE study by *Meinen and Luther* [2003] (hereinafter referred to as ML03), the SYNOP studies by *Johns et al.* [1995] and *Meinen et al.* [2008], and the KE study by *Hall* [1989], the distance of each measurement from the core may be determined before the down-stream direction is defined. In the following, some methods commonly employed for each of these steps are described and their application to the KESS dataset is discussed.

Core Location Identification ML03, in their comparison of stream-coordinate definition methods for the Subantarctic Front (SAF), suggest that the best methods are those that make the fewest a priori assumptions about the current structure. In particular, they refer to the "frozen field" method that has been used in studies involving data from very few moorings, in which a time-invariant cross-stream baroclinic structure is assumed. Under this assumption, the cross-stream pycnocline structure remains constant, so the origin of the stream-coordinate system need not be located at the center of the current. ML03 show, however, that the baroclinic structure of

the SAF, and presumably of other such jets, is in fact strongly time-*dependent*, and that a highly erroneous picture having qualitatively the wrong shape may be obtained under the frozen-field assumption. The preferred alternative is to determine a characteristic of the structure that is representative of the center of the jet and to use its location to define the location of the core as a function of time. In many studies in which fine horizontal-scale ADCP transects are not available, this is done by finding the location of a particular isotherm crossing some pressure surface or depth, or the midpoint between where an isotherm crosses two different pressure surfaces or depths [*Halkin and Rossby*, 1985]. As ML03 describe, the appropriate isotherm should be chosen by determining the most common temperature at the depth of the maximum vertical gradient of temperature in the thermocline, and the appropriate isobar (or depth) should lie at the central minimum of a bi-modal distribution of pressures (or depths) of the isotherm. Thermal wind and geostrophy suggest that in most cases this location is equivalent to the location of the maximum velocity, so our decision in the KESS study to define the core as the location of the maximum velocity averaged over 100-300 m depth in the surveys, and at the surface in the CPIES data, is consistent with these methods. To assure the reader that this is so, a comparison of resultant core locations using several different methods is presented with the KESS feature survey data.

The hydrographic core definition method tested here is the same as that used by *Mizuno and White* [1983]: the location at which the 12°C isotherm crosses 300 m. For each of the survey crossings, the CTD data are interpolated along the ship track and used to identify this location to define the core. This method is compared with several variations on the maximum velocity method, using the maximum current velocity at a single depth of 150 m and the maximum after averaging over the depth intervals 100-200 m, 100-300 m, and 100-400 m. Core locations are calculated with each of these methods both before and after gridding the ADCP and CTD data to an even 5-km horizontal grid. The method of defining the core has little effect on the resulting core location, particularly after gridding the data. For all cases in the gridded data, the maximum difference in core locations among the different methods is about 5 km, or one grid-spacing, which represents a difference of about 1.5 10-minute averaging intervals for the ADCP

data. Typically, averaging over 100-300 and 100-400 m produces the same core location coordinates. Using the shallower average of 100-200 m or the single 150 m maximum sometimes produces the same core location as the deeper averages and sometimes results in a core that is slightly further to the northeast. For Crossing 3, the shallower maximum speed methods produce a core further to the southwest than the deeper averages, but after gridding, all four ADCP methods produce the same core location. Using the hydrographic definition results in a core location that sometimes agrees with the shallower ADCP-defined cores and sometimes with the deeper ones. Table B.1 gives the core coordinates before and after gridding for each of the core location methods, and the results are displayed graphically in Figure B.1. The chosen method appears to produce the smoothest zonal variations in core positions.

Cross-stream Distance ML03 discuss the use of mooring arrays rather than fine horizontal-scale velocity transects for creating stream-coordinates sections and must therefore bin each individual velocity measurement at each mooring as a function of distance from the core to produce a mean cross-section. They determine cross-stream distance for each measurement by finding the perpendicular distance of each mooring on each day from the contour defining the core, and they show that this method produces a significantly more accurate result than the frozen field method, in which cross-stream location is determined simply by finding the depth of a certain isotherm at each mooring site on each day. Since near-synoptic ADCP transects are available from the KESS dataset, as well as a large CPIES array from which daily geostrophic velocity transects can be optimally interpolated, cross-stream distance is simply determined *after* defining the down-stream direction by projecting the data along the down-stream direction onto the cross-stream line, or by interpolating from the array to the cross-stream line in the case of the CPIES. See Figure 1.4 in the main text for an illustration of this procedure for the surveys.

Down-stream Direction Definition Again, because the datasets discussed by ML03 do not contain fine horizontal-scale synoptic transects, down-stream direction cannot be determined directly from the velocities at the core but must be estimated via a proxy. Two such proxy methods that are commonly used are to define down-stream as the tangent to the contour defining the cur-

rent core (where some isotherm crosses some isobar), or to define it as the direction of the local maximum of vertical shear of horizontal velocities. ML03 present various reasons for preferring the former. The KESS shipboard ADCP surveys and mapped CPIES datasets, however, include measurements of velocity at the core for all transects, so these can be used as a whole-transect representation of down-stream flow direction. Various vertical and horizontal averages of current vectors at and surrounding the core were investigated with the KESS data as possible methods for determining down-stream direction and were evaluated according to the amount of rotation required to rotate the original line between the first and last CTD casts of the crossing onto the X-axis of the new coordinate system (the cross-stream axis) and the amount of directional variation of the velocity vectors with depth from the down-stream direction. Methods examined included using only the vectors at the core averaged over various depth ranges, as well as taking the horizontal average of three and five central vectors, also averaged over various depth ranges. Differences in rotation angles for the CTD line and in the rotation of currents with depth from the defined down-stream direction were minimal among the definition methods, with a maximum difference between methods of about 2.4° in CTD line rotation for any one crossing (see Table B.2). However, the first method, which performs no vertical averaging, produces results for Crossings 2-4 that are inconsistent with the results of the other four methods. As described in the main text, the remaining four methods have maximum differences in down-stream direction of about 1.25°, which would result in maximum errors of $\sim$4.5 cm/s in the cross-stream velocities at times when absolute velocities reach 2 m/s. Given the similarity among these remaining methods, the ultimate choice of method represents the desire to perform some averaging in order to reduce the possibility of biasing the down-stream direction with an anomalous current vector, without averaging so much that the down- and cross-stream flow structure is significantly smoothed.

Table B.1

Latitude/Longitude Coordinates of Core from Various Core Location Methods Before (top) and After (bottom) Gridding to 5 km Horizontal Grid

Method	Crossing 1	Crossing 2	Crossing 3	Crossing 4
12°C Isotherm	34.71,145.94	34.65,146.16	34.57,146.46	34.63,146.85
ADCP 150m	34.71,145.93	34.69,146.19	34.61,146.52	34.63,146.84
ADCP 100-200m	34.73,145.95	34.67,146.18	34.61,146.52	34.60,146.83
ADCP 100-300m	34.69,145.91	34.64,146.17	34.66,146.54	34.60,146.84
ADCP 100-400m	34.69,145.92	34.64,146.17	34.66,146.54	34.60,146.84

Method	Crossing 1	Crossing 2	Crossing 3	Crossing 4
12°C Isotherm	34.71,145.90	34.65,146.14	34.57,146.45	34.62,146.83
ADCP 150m	34.75,145.93	34.69,146.16	34.61,146.47	34.62,146.83
ADCP 100-200m	34.75,145.93	34.69,146.16	34.61,146.47	34.62,146.83
ADCP 100-300m**	34.71,145.90	34.65,146.14	34.61,146.47	34.62,146.83
ADCP 100-400m	34.71,145.90	34.65,146.14	34.61,146.47	34.58,146.81

Note. Method names indicate the hydrographic method or one of the four ADCP methods, which used a current velocity maximum at a single depth of 150 m or the maximum velocity averaged over one of several depth ranges, as indicated by the specified depth values.
**Indicates the final choice of method.

Table B.2

Down-stream Angle (top) and Rotation Angles of CTD Line (bottom) for Each Crossing from Various Down-stream Direction Definition Methods

Method	Crossing 1	Crossing 2	Crossing 3	Crossing 4
150m 5 pt. Avg.	-46.63	-42.80	-38.72	-30.42
100-300m Single	-48.02	-41.63	-39.92	-29.46
100-300m 3 pt. Avg.**	-47.07	-40.42	-40.14	-29.67
100-300m 5 pt. Avg.	-46.76	-40.53	-40.19	-29.65
100-400m 5 pt. Avg.	-46.90	-40.46	-40.66	-29.48

Method	Crossing 1	Crossing 2	Crossing 3	Crossing 4
150m 5 pt. Avg.	-19.66	-15.84	-12.77	-4.49
100-300m Single	-21.05	-14.67	-13.97	-3.53
100-300m 3 pt. Avg.**	-20.10	-13.46	-14.19	-3.74
100-300m 5 pt. Avg.	-19.79	-13.57	-14.24	-3.72
100-400m 5 pt. Avg.	-19.93	-13.50	-14.71	-3.55

Note. Angles are in degrees, with negative values signifying clockwise rotation from 0 pointing due east. Method names indicate depths over which ADCP data are averaged and number of points included in horizontal average. “3 pt. Avg.” implies an average of the vector at the core with the vectors one grid-space to the north and south of the core, hence a 10 km lateral average. Similarly, “5 pt. Avg.” implies a 20 km lateral average.
**Indicates final choice of method.

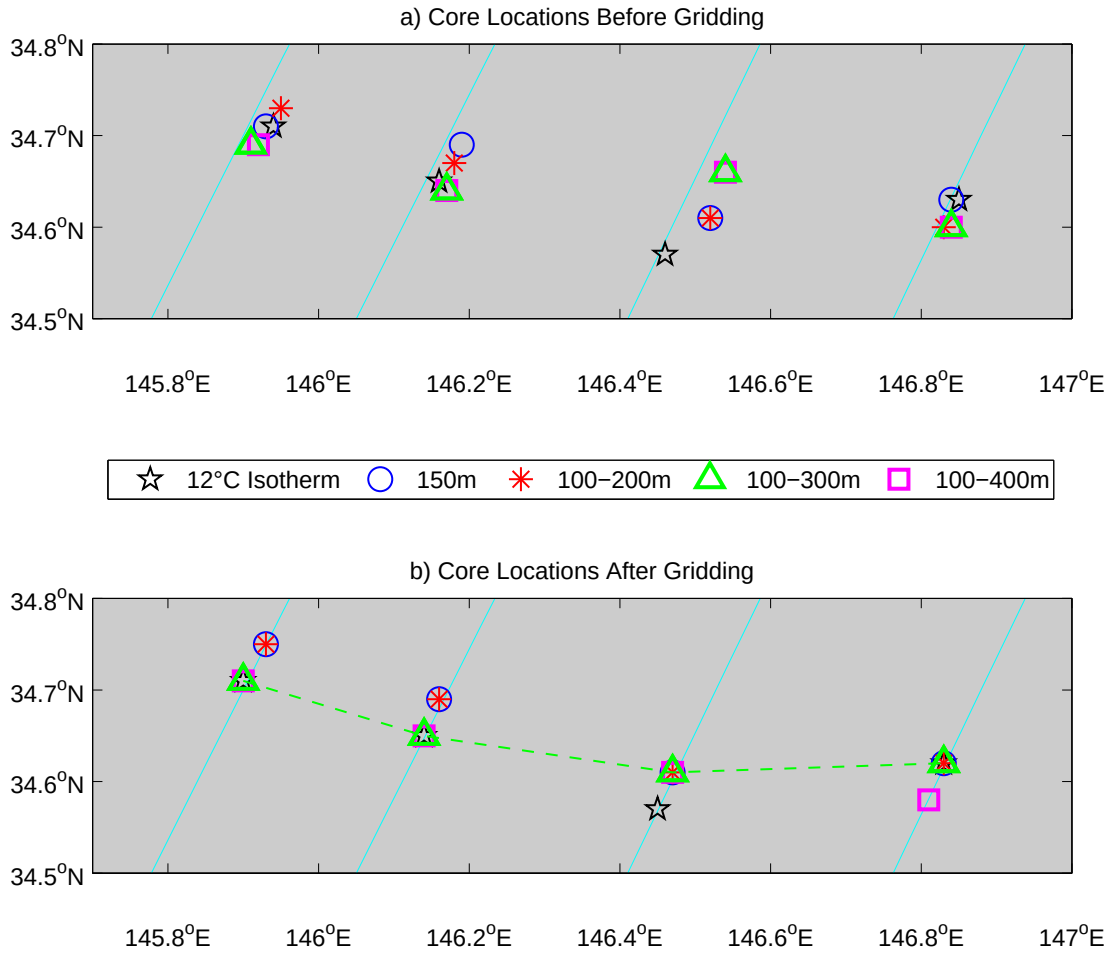

Figure B.1: Map of core locations identified using the five core location methods described in the text and listed in Table 1 both a) before, and b) after gridding the data to the 5 km grid. Light blue lines represent the four successive fine-scale survey crossings, Crossing 1 being the furthest west. Each symbol represents the location of the core as defined by the corresponding method given in the legend. Green triangles represent the final choice of method, the location of the maximum velocity after averaging the velocities over 100-300 m depth. Dashed green lines connect the cores as located with the chosen method, showing smooth geographical variation with longitude following the meander shape.

List of References

Halkin, D., and T. Rossby (1985), The Structure and Transport of the Gulf Stream at 73°W, *J. Phys. Oceanogr.*, *15*(11), 1439–1452.

Hall, M. M. (1989), Velocity and Transport Structure of the Kuroshio Extension at 35°N, 152°E, *J. Geophys. Res.*, *94*(10), 14,445–14,459.

Johns, W. E., T. J. Shay, J. M. Bane, and D. R. Watts (1995), Gulf Stream Structure, Transport, and Recirculation near 68°W, *J. Geophys. Res.*, *100*(C1), 817–838.

Meinen, C. S., and D. S. Luther (2003), Comparison of methods of estimating mean synoptic current structure in ”stream coordinates” reference frames with an example from the Antarctic Circumpolar Current, *Deep-Sea Res.*, *50*, 201–220.

Meinen, C. S., D. S. Luther, and M. O. Baringer (2008), Structure, transport, and potential vorticity of the Gulf Stream at 68°W: Revisiting older data sets with new techniques, *Deep-Sea Res.*, to appear.

Mizuno, K., and W. B. White (1983), Annual and Interannual Variability in the Kuroshio Current System, *J. Phys. Oceanogr.*, *13*(10), 1847–1867.

APPENDIX C

CPIES Processing and Error Estimates

The KESS CPIES instruments consisted of bottom-moored inverted echo sounders measuring round-trip acoustic travel time between the sea floor and surface as well as Paroscientific Digiquartz sensors measuring near-bottom pressure and temperature (for calibration purposes) and Aanderaa acoustic Doppler current meters measuring current speed and direction, tilt, and temperature 50 m above the moored instrument [*URI*, 2006]. This combination of instruments and sensors produced a set of three types of measurements which were processed according to standard CPIES post-processing procedures for use as one combined dataset. The basic processing steps and associated errors are outlined here. For further details, see *Donohue et al.* [2008], *URI* [2006], *Kennelly et al.* [2007], and *Kennelly et al.* [2008].

The CPIES emitted twenty-four 12-kHz acoustic pings per hour, which were scheduled to occur in 4-ping bursts every 10 minutes after the hour. A modified quartile method [*Kennelly et al.*, 2007] was performed on this raw time series in order to extract the hourly signal from the τ estimates, which are scattered due to sea surface roughness. This method produced hourly travel time estimates which were then 72-hour low-pass filtered with a 4th-order Butterworth filter and subsampled at half-day intervals.

The measured τ values resulting from the initial post-processing procedures (τ_m) are not yet in a form appropriate for use in the GEM. In order to convert them to this form, referred to as τ_{index}, mass-loading contributions to variation in τ must first be removed, as the hydrographic measurements used to create the GEM represent only steric SSH changes. Next, a so-called "dynamic τ" is calculated, which removes the effects of the latitudinal dependence of g. The dynamic τ records are then de-seasoned over the upper 250 dbar. The subscript *index* refers to the fact that the measured τ values come from instruments deployed at a variety of depths, so they

must therefore be indexed to some specified depth via a τ_m-τ_{index} relationship. To accomplish this, all τ time series are calibrated with CTD casts to 4000 dbar, and these are then converted to $\tau_{0-1400} = \tau_{index}$, via a fitted polynomial relationship between τ_{0-4000} and τ_{0-1400}. These τ_{index} values are finally ready for use in the GEM lookup table. Combining all contributing sources of error related to the τ data produces an estimate of standard deviation in τ_{index} of 1.02 ms. For more processing details see *Kennelly et al.* [2008].

Bottom pressure measurements were also recorded every 10 minutes and were averaged to create hourly estimates. These hourly values were detided using tidal response analysis [*Munk and Cartwright*, 1966]. Although preconditioning of the pressure sensors at 3000 dbar for 1-2 months prior to deployment was performed to considerably reduce the amount of drift occurring during the mission, pressure records still required de-drifting, which was performed visually as a first approximation. The records were then detided a second time to refine the estimate. In order to remove any remaining drift from the records, a new technique was used in which mismatch is minimized between 31-day low-pass filtered streamfunctions derived from the pressure records and the bottom current meters. Real ocean signals of long period can thereby be distinguished from instrument drift, and pressure drift is removed with great accuracy; this process also results in leveling of the dedrifted pressures. A final detiding was then performed, and the resulting pressure time series were de-meaned and subjected to the same 72-hour low-pass 4th-order Butterworth filter as the τ measurements and subsampled at half-day intervals. The overall error associated with the bottom pressure measurements at the CPIES sites is estimated to have standard deviation 0.74 cm.

The bottom current meters recorded zonal and meridional velocities every 20 minutes. After converting these measurements to speed and direction, three corrections were performed. The first was to adjust for local magnetic declination at each site. Second was a speed of sound correction, applied for each instrument according to its depth, which was required as the near-bottom speed of sound in the KESS region varies by about 40-65 m/s from the 1500 m/s nominal

speed of sound used by the current meters. Finally, the speeds were multiplied by a factor of 1.1, in accordance with a study by *Hogg and Frye* [2007] which showed that RCM-11 current meter speeds are biased low. Once these corrections had been made, the measurements were converted back to zonal and meridional components and averaged hourly. The time series were 72-hour low-pass 4th-order Butterworth filtered and subsampled at half-day intervals. The overall estimated standard deviation error associated with the bottom current meter measurements at the CPIES sites is 1.6 cm/s.

The method described in Section 1.2.2 for determining absolute velocities from CPIES measurements (summing baroclinic shears derived from geopotential height difference and deep barotropic velocities from the combined pressure and current meter mapped velocities) incorporates error from various sources including scatter in the GEM field and error in the deep current measurements, as well as that due to assumption of geostrophic flow. Propagating these individually estimated errors through to produce a single error estimate for the CPIES-derived velocity profiles produces a result in good agreement with that obtained via a simple comparison between the direct velocity measurements made by the moored profilers and the co-located CPIES measurements (locations shown in Figure 1.6). The maximum RMS differences from this profiler-CPIES comparison were found to range between 12 and 26 cm/s, some of which is due to the fact that the profilers provide actual point measurements while the CPIES velocities represent a geostrophic average over 80-90 km between instruments.

The OI mapping also mentioned in Section 1.2.2 has its own associated errors [*Donohue et al.*, 2008], which increase the farther one moves from actual CPIES measurement locations. During the first year of the KESS CPIES mission, that is, during the whole of the weakly meandering period which is under scrutiny in this study, the CPIES at site D3 failed to record any data, leaving a hole in the array which was partially compensated by OI mapping. Figure C.1 provides maps of sample surface and bottom velocity errors from the mapped CPIES τ and pressure measurements and bottom current meters. The mapped bottom velocity errors are of the order 2 cm/s

over most of the array and remain about the same magnitude throughout the weakly meandering period. Mapped surface velocity errors reach close to 30 cm/s in the high-velocity jet region and vary only slightly over the time series.

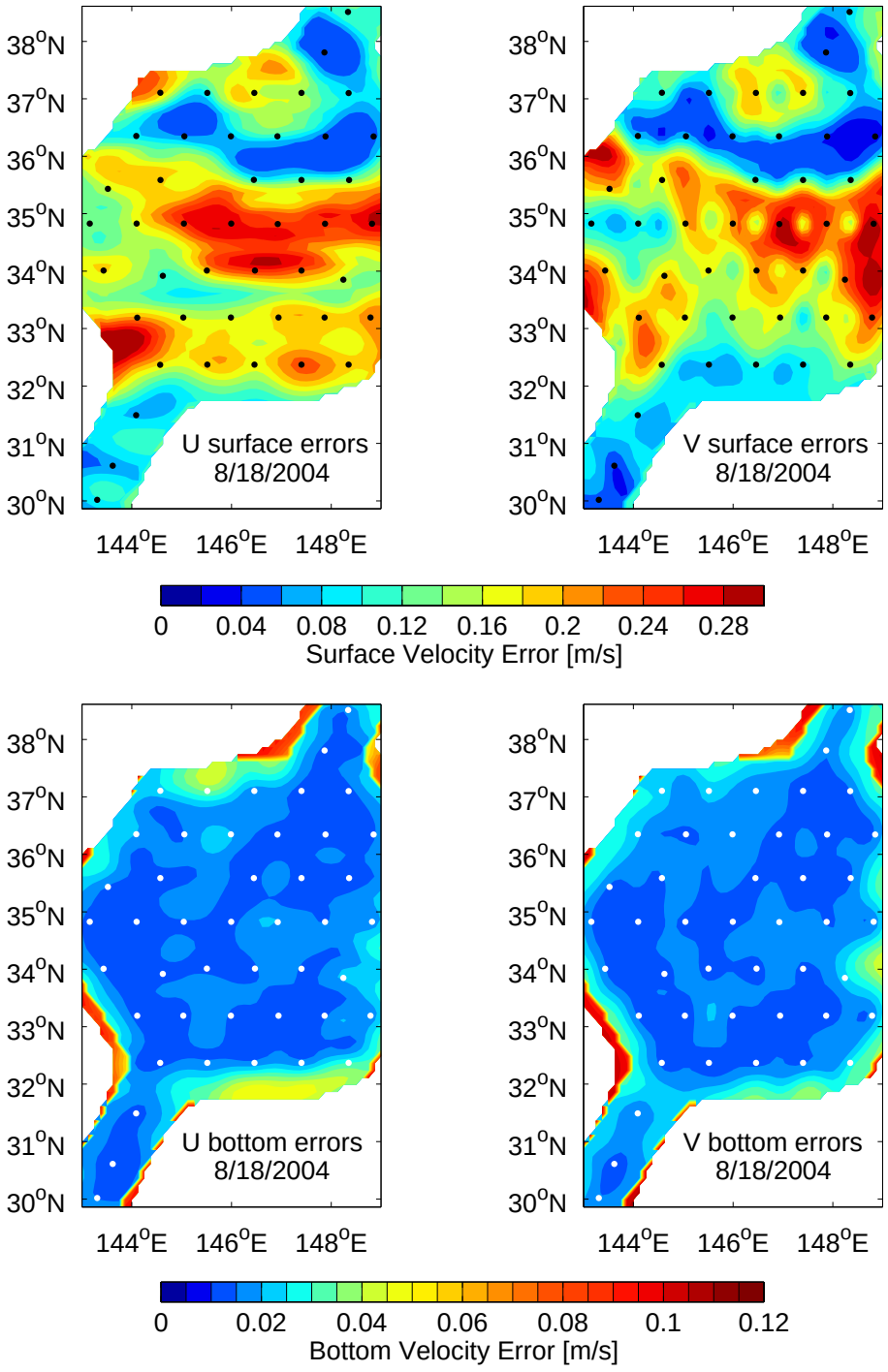

Figure C.1: Error maps for U and V components of surface and bottom velocities from CPIES τ measurements and bottom current meters. Black and white dots indicate location of CPIES instruments. Note gap in array where instrument 'D3' failed. Maps shown here are from 18 August, 2004, in the middle of the weakly meandering period. Bottom errors remain about the same magnitude throughout the weakly meandering period, and surface errors vary only slightly, maintaining a fairly constant geographical distribution.

List of References

Donohue, K. A., D. R. Watts, K. L. Tracey, A. D. Greene, and M. Kennelly (2008), Mapping circulation in the Kuroshio Extension with an array of Current and Pressure recording Inverted Echo Sounders, in progress.

Hogg, N. G., and D. E. Frye (2007), Performance of a New Generation of Acoustic Current Meters, *J. Phys. Oceanogr.*, *37*(2), 148–161.

Kennelly, M., K. Tracey, and D. R. Watts (2007), Inverted Echo Sounder Data Processing Manual, *Tech. Rep. 2007-02*, Graduate School of Oceanography, University of Rhode Island, Narragansett, Rhode Island.

Kennelly, M., K. Donohue, A. Greene, K. L. Tracey, and D. R. Watts (2008), Inverted Echo Sounder Data Report, *Tech. Rep. 2008-XX*, Graduate School of Oceanography, University of Rhode Island, Narragansett, Rhode Island.

Munk, W. H., and D. E. Cartwright (1966), Tidal Spectroscopy and Prediction, *Philos. Trans. Roy. Soc. London*, *259*(1105), 533–581.

URI (2006), *Inverted Echo Sounder User's Manual IES Model 6.2*, Graduate School of Oceanography, University of Rhode Island, Narragansett, Rhode Island.

BIBLIOGRAPHY

Bendat, J. S., and A. G. Piersol (2000), *Random Data: Analysis and Measurement Procedures*, 3rd ed., Wiley, John and Sons, Incorporated, New York.

Book, J. (1998), Kuroshio variations off southwest Japan, Master's thesis, Graduate School of Oceanography, University of Rhode Island, Narragansett, Rhode Island, 92pp.

Bower, A. S. (1989), Potential Vorticity Balances and Horizontal Divergence along Particle Trajectories in Gulf Stream Meanders East of Cape Hatteras, *Journal of Physical Oceanography*, *19*(11), 1669–1681.

Bower, A. S. (1991), A Simple Kinematic Mechanism for Mixing Fluid Parcels across a Meandering Jet, *Journal of Physical Oceanography*, *21*(1), 173–180.

Bower, A. S., and T. Rossby (1989), Evidence of Cross-Frontal Exchange Processes in the Gulf Stream Based on Isopycnal RAFOS Float Data, *Journal of Physical Oceanography*, *19*(9), 1177–1190.

Bower, A. S., H. T. Rossby, and J. L. Lillibridge (1985), The Gulf Stream - Barrier or Blender?, *Journal of Physical Oceanography*, *15*(1), 24–32.

Cushman-Roisin, B. (1994), *Introduction to Geophysical Fluid Dynamics*, Prentice Hall, Upper Saddle River, New Jersey 07458.

Dewar, W. K., and J. M. Bane, Jr. (1985), Subsurface Energetics of the Gulf Stream Near the Charleston Bump, *Journal of Physical Oceanography*, *15*(12), 1771–1789.

Donohue, K. A., D. R. Watts, K. L. Tracey, A. D. Greene, and M. Kennelly (2008), Mapping circulation in the Kuroshio Extension with an array of Current and Pressure recording Inverted Echo Sounders, in progress.

Firing, E., J. Ranada, and P. Caldwell (1995), *Processing ADCP Data with the CO-DAS Software System Version 3.1*, Joint Institute for Marine and Atmospheric Research, University of Hawaii, and National Oceanography Data Center, Available at *http://currents.soest.hawaii.edu/docs/doc/index.html*, (accessed 28 May, 2008).

Greene, A., C. Ashmankas, K. Donohue, R. Watts, G. Chaplin, and K. Tracey (2004), KESS Deployment Cruise Report, unpublished.

Halkin, D., and T. Rossby (1985), The Structure and Transport of the Gulf Stream at 73°W, *Journal of Physical Oceanography*, *15*(11), 1439–1452.

Hall, M. M. (1989), Velocity and Transport Structure of the Kuroshio Extension at 35°N, 152°E, *Journal of Geophysical Research, 94*(10), 14,445–14,459.

Hogg, N. G., and D. E. Frye (2007), Performance of a New Generation of Acoustic Current Meters, *Journal of Physical Oceanography*, *37*(2), 148–161.

Holton, J. R. (1992), *An Introduction to Dynamic Meteorology*, 3rd ed., Academic Press, San Diego.

Howden, S. D., and D. R. Watts (1999), Jet streaks in the Gulf Stream, *Journal of Physical Oceanography*, *29*, 1910–1924.

Johns, W. E., T. J. Shay, J. M. Bane, and D. R. Watts (1995), Gulf Stream Structure, Transport, and Recirculation near 68°W, *Journal of Geophysical Research*, *100*(C1), 817–838.

Joyce, T. M., I. Yasuda, Y. Hiroe, K. Komatsu, K. Kawasaki, and F. Bahr (2001), Mixing in the Meandering Kuroshio Extension and the Formation of North Pacific Intermediate Water, *Journal of Geophysical Research*, *106*(C3), 4397–4404.

Kennelly, M., K. Tracey, and D. R. Watts (2007), Inverted Echo Sounder Data Processing Manual, *Tech. Rep. 2007-02*, Graduate School of Oceanography, University of Rhode Island, Narragansett, Rhode Island.

Kennelly, M., K. Donohue, A. Greene, K. L. Tracey, and D. R. Watts (2008), Inverted Echo Sounder Data Report, *Tech. Rep. 2008-XX*, Graduate School of Oceanography, University of Rhode Island, Narragansett, Rhode Island.

Kouketsu, S., I. Yasuda, and Y. Hiroe (2005), Observation of Frontal Waves and Associated Salinity Minimum Formation Along the Kuroshio Extension, *Journal of Geophysical Research, 110*, doi:10.1029/2004JC002862.

Kouketsu, S., I. Yasuda, and Y. Hiroe (2007), Three-Dimensional Structure of Frontal Waves and Associated Salinity Minimum Formation Along the Kuroshio Extension, *Journal of Physical Oceanography*, *37*, 644–656.

Liu, M. (1991), The upper ocean velocity structure of Gulf Stream meanders - An application of the ADCP, Master's thesis, Graduate School of Oceanography, University of Rhode Island, Narragansett, Rhode Island, 101 pp.

Liu, M., and T. Rossby (1993), Observations of Velocity and Vorticity Structure of Gulf Stream Meanders, *Journal of Physical Oceanography*, *23*(2), 329–345.

Logoutov, O., G. Sutyrin, and D. R. Watts (2001), Potential Vorticity Structure Across the Gulf Stream: Observations and a PV-Gradient Model, *Journal of Physical Oceanography*, *31*(2), 637–644.

Meinen, C. S., and D. S. Luther (2003), Comparison of methods of estimating mean synoptic current structure in "stream coordinates" reference frames with an example from the Antarctic Circumpolar Current, *Deep-Sea Research*, *50*, 201–220.

Meinen, C. S., D. S. Luther, D. R. Watts, A. D. Chave, and K. L. Tracey (2003), Mean Stream Coordinate Structure of the Subantarctic Front: Temperature, Salinity, and Absolute Velocity, *Journal of Geophysical Research*, *108*(C8), doi:10.1029/2002JC001545.

Meinen, C. S., D. S. Luther, and M. O. Baringer (2008), Structure, transport, and potential vorticity of the Gulf Stream at 68°W: Revisiting older data sets with new techniques, *Deep-Sea Research*, to appear.

Mizuno, K., and W. B. White (1983), Annual and Interannual Variability in the Kuroshio Current System, *Journal of Physical Oceanography*, *13*(10), 1847–1867.

Mueller, P. (1995), Ertel's Potential Vorticity Theorem in Physical Oceanography, *Rev. Geophys.*, *33*(1), 67–97.

Munk, W. H., and D. E. Cartwright (1966), Tidal Spectroscopy and Prediction, *Philos. Trans. Roy. Soc. London*, *259*(1105), 533–581.

Qiu, B., and S. Chen (2005), Variability of the Kuroshio Extension Jet, Recirculation Gyre, and Mesoscale Eddies on Decadal Time Scales, *Journal of Physical Oceanography*, *35*(11), 2090–2103.

Qiu, B., P. Hacker, S. Chen, K. A. Donohue, D. R. Watts, H. Mitsudera, N. G. Hogg, and S. R. Jayne (2006), Observations of Subtropical Mode Water Evolution from the Kuroshio Extension System Study, *Journal of Physical Oceanography*, *36*.

Qiu, B., S. Chen, P. Hacker, N. G. Hogg, S. R. Jayne, and H. Sasaki (2008), The Kuroshio Extension Northern Recirculation Gyre: Profiling Float Measurements and Forcing Mechanism, *Journal of Physical Oceanography*, to appear.

Rajamony, J., D. Hebert, and T. Rossby (2001), The Cross-Stream Potential Vorticity Front and Its Role in Meander-Induced Exchange in the Gulf Stream, *Journal of Physical Oceanography*, *31*(12), 3551–3568.

RDI (1996), *Acoustic Doppler Current Profiler Principles of Operation: A Practical Primer*, RD Instruments, 9855 Businesspark Ave., San Diego, California 92131, 2 ed.

Rossby, T., and E. Gottlieb (1998), The *Oleander* Project: Monitoring the Variability of the Gulf Stream and Adjacent Waters between New Jersey and Bermuda, *Bull. Amer. Meteorol. Soc.*, *79*(1), 5–18.

Rossby, T., and H.-M. Zhang (2001), The Near-Surface Velocity and Potential Vorticity Structure of the Gulf Stream, *Journal of Marine Research*, *59*, 949–975.

Savidge, D. K., and J. M. Bane, Jr. (1999), Cyclogenesis in the deep ocean beneath the Gulf Stream: 1. Description, *Journal of Geophysical Research*, *104*(C8), 18,111 – 18,126.

Sun, C., and D. R. Watts (2001), A Circumpolar Gravest Empirical Mode for the Southern Ocean Hydrography, *Journal of Geophysical Research*, *106*(C2), 2833–2855.

Taguchi, B., S.-P. Xie, H. Mitsudera, and A. Kubokawa (2005), Response of the Kuroshio Extension to Rossby Waves Associated with the 1970s Climate Regime Shift in a High-Resolution Ocean Model, *Journal of Climate*, *18*(15), 2979–2995.

Talley, L. D., and J.-Y. Yun (2000), The Role of Cabbeling and Double Diffusion in Setting the Density of the North Pacific Intermediate Water Salinity Minimum, *Journal of Physical Oceanography*, *31*(6), 1538–1549.

Talley, L. D., Y. Nagata, M. Fujimara, T. Iwao, T. Kono, D. Inagake, M. Hirai, and K. Okuda (1995), North Pacific Intermediate Water in the Kuroshio/Oyashio Mixed Water Region, *Journal of Physical Oceanography*, *25*(4), 475–501.

Teague, W. J., M. J. Carron, and P. J. Hogan (1990), A Comparison Between the Generalized Digital Environmental Model and Levitus Climatologies, *Journal of Geophysical Research*, *95*(C5), 7167–7183.

URI (2006), *Inverted Echo Sounder User's Manual IES Model 6.2*, Graduate School of Oceanography, University of Rhode Island, Narragansett, Rhode Island.

Watts, D. R., K. L. Tracey, J. M. Bane, and T. J. Shay (1995), Gulf Stream path and thermocline structure near 74°W and 68°W, *Journal of Geophysical Research*, *100*(C9), 18,291–18,312.

Watts, D. R., C. Sun, and S. Rintoul (2001), A Two-Dimensional Gravest Empirical Mode Determined from Hydrographic Observations in the Subantarctic Front, *Journal of Physical Oceanography*, *31*(8), 2186–2209.

Yasuda, I., K. Okuda, and Y. Shimizu (1996), Distribution and Modification of North Pacific

Intermediate Water in the Kuroshio-Oyashio Interfrontal Zone, *Journal of Physical Oceanography*, *26*(4), 448–465.